Copyright Warning & Restrictions

The copyright law of the United States (Title 17, United States Code) governs the making of photocopies or other reproductions of copyrighted material.

Under certain conditions specified in the law, libraries and archives are authorized to furnish a photocopy or other reproduction. One of these specified conditions is that the photocopy or reproduction is not to be "used for any purpose other than private study, scholarship, or research." If a, user makes a request for, or later uses, a photocopy or reproduction for purposes in excess of "fair use" that user may be liable for copyright infringement,

This institution reserves the right to refuse to accept a copying order if, in its judgment, fulfillment of the order would involve violation of copyright law.

Please Note: The author retains the copyright while the New Jersey Institute of Technology reserves the right to distribute this thesis or dissertation

Printing note: If you do not wish to print this page, then select "Pages from: first page # to: last page #" on the print dialog screen

ABSTRACT

THE CONSTANT FRACTURE ANGLE MODEL FOR CEMENTITIOUS MATERIALS

by
Suk Ki Kim

Fracture mechanics of concrete has been investigated for the past two decades using linear elastic and nonlinear fracture mechanics concepts. The models proposed so far remain questionable largely due to specimen dependency of the proposed fracture parameters.

In this study, a new approach for modeling the fracture characteristics of concrete and fiber reinforced concrete is proposed. The model depends on the load-*CMOD* relationship rather than the traditional load-deflection principle. Although energy consumed during fracture is definitely a direct function of the load-displacement response, it was observed that traditional displacement measurement included an extraneous and erratic portion due to test setup and support crushing. The magnitude of this erroneous deformation was found to be of the same order as the actual displacement, leading to inaccurate determinations of fracture parameters. To overcome this problem, the load-*CMOD* relationship is a more reliable parameter for determining the fracture characteristics because it is unaffected by the specimen setup and any support crushing.

An important step towards the use of load-*CMOD* concept as a key fracture parameter depends on relating the *CMOD* to the traditional load-line deflection. This investigation found that there is a unique linear relationship between the *CMOD* and the load-line deflection, provided that deflection is measured accurately. The exact numeric value of relationship between the CMOD and the deflection, that is, the slope of the line, is discovered to be a material property. This linear relationship between the deflection

and *CMOD* can be understood physically as a constant fracture angle of the material. The proposed concept is therefore named the Constant Fracture Angle Model.

The model was evaluated for size dependency using several sizes of notched beams with different notch lengths. Different types of cementitious materials were also investigated to confirm the validity of the proposed model. The proposed model finds a problem with the existing RILEM recommendations for measuring the fracture toughness of concrete. A proposal to correct the problem is made.

This theoretical model can easily relate the fracture energy to the observed load-*CMOD* response. The model shows that fracture energy is a constant fracture parameter and independent of specimen and notch size. The model also provides a constant linear relationship of the deflection and *CMOD*, works with a range of specimen sizes to produce consistent fracture parameters, and the size of an equivalent micro cracked zone. In addition, it also generates a new concept for measuring the toughness index of fiber reinforced composites. Different types of fiber reinforced materials were studied and the same unique relationships were observed.

Finally, a new standard testing setup for measuring the fracture parameters of concrete is proposed if the traditional load-line deflection method is to be used. However, the present study strongly suggests that the *CMOD* response should be used as the new standard for any future fracture toughness testing and evaluation.

THE CONSTANT FRACTURE ANGLE MODEL FOR CEMENTITIOUS MATERIALS

by
Suk Ki Kim

A Dissertation
Submitted to the Faculty of
New Jersey Institute of Technology
in Partial Fulfillment of the Requirements for the Degree of
Doctor of Philosophy

Department of Civil and Environmental Engineering

May 1996

APPROVAL PAGE

THE CONSTANT FRACTURE ANGLE MODEL FOR CEMENTITIOUS MATERIALS

Suk Ki Kim

Dr. Methi Wecharatana, Dissertation Adviser — Date
Professor of Civil and Environmental Engineering, NJIT

Dr. Farhad Ansari, Committee Member — Date
Professor of Civil and Environmental Engineering, NJIT

Dr. Dorairaja Raghu, Committee Member — Date
Professor of Civil and Environmental Engineering, NJIT

Dr. Namunu Meegoda, Committee Member — Date
Associate Professor of Civil and Environmental Engineering, NJIT

Dr. Kenneth Sohn, Committee Member — Date
Professor of Electrical and Computer Engineering, NJIT

BIOGRAPHICAL SKETCH

Author: Suk Ki Kim

Degree: Doctor of Philosophy in Civil Engineering

Date: May 1996

Undergraduate and Graduate Education:

- Doctor of Philosophy in Civil and Environmental Engineering,
  New Jersey Institute of Technology, Newark, NJ, 1996
- Master of Science in Civil Engineering,
  Yonsei University, Seoul, Korea, 1974
- Bachelor of Engineering in Civil Engineering,
  Yonsei University, Seoul, Korea, 1972

Major: Civil Engineering

Publication:

Suk Ki Kim "A Generalized Formulation of Optimum Design of Steel Framed Structures using Elastic Theory," M. S. Thesis, Yonsei University, 1974

ACKNOWLEDGMENT

The author would like to express his sincere gratitude to his advisor, Professor Methi Wecharatana, for his invaluable guidance, suggestions, encouragement and patience during the development of this study. Appreciation is also extended to Professors Farhad Ansari, Dorairaja Raghu, Namunu Meegoda and Kenneth Sohn for serving as thesis committee members.

Appreciation also goes to Dr. Lin Showmay Hsu and Mr. Allyn Luke who provided advice and help in my dissertation.

Finally, the author wishes to thank his entire family for their patience, encouragement and support. The author would also like to thank Dankook University for providing the opportunity to study at NJIT.

TABLE OF CONTENTS

TABLE OF CONTENTS
(Continued)

LIST OF TABLES

LIST OF FIGURES

LIST OF FIGURES
(Continued)

LIST OF FIGURES
(Continued)

LIST OF FIGURES
(Continued)

LIST OF FIGURES
(Continued)

LIST OF FIGURES
(Continued)

LIST OF FIGURES
(Continued)

LIST OF FIGURES
(Continued)

Figure **Page**

CHAPTER 1

INTRODUCTION

Fracture mechanics is devoted to the analysis of cracked bodies based on Griffith's [1920; 1924] pioneering work that determined the fracture strength of brittle solids. The scope and complexity of problems treated with fracture mechanics theory has been increasing ever since. Finding the load required to cause a critical stress singularity ahead of a crack tip, described by a stress intensity factor, and the accompanying crack extension leading to failure are the kind of problems commonly solved using fracture mechanics.

Due to concrete's low tension resistance, most of the failures observed in concrete structures are initiated by local tensile failure in an area of high stress concentrations or within a zone of pre-existing flaws. Recently, it has been realized that in order to improve the serviceability and safety of concrete structures, the tensile fracture resistance of concrete has to be incorporated into the analysis procedures [Hawkins 1984; Tassios 1984; Elfgren 1988; Darwin et al. 1994].

More than thirty years after Kaplan's [1961] first attempts to apply fracture mechanics to concrete, it is still not clear whether or not the cracking of concrete can be predicted with linear elastic fracture mechanics (LEFM). Many inconsistent results determining the fracture parameters, fracture toughness (K_{IC}) or critical strain energy release rate (G_{IC}), and highly contradictory conclusions have been reported by the many researchers [Naus 1969; Brown 1983; Francois 1984]. One of the primary reasons for the discrepancies and increased complexity of the problem is a lack of knowledge about the exact nature of the process zone. The experimental studies of the process zone in concrete materials are hindered by the difficulties in estimating both the traction-free crack and the process zone size.

Another important fracture parameter is the fracture energy (G_F), which has a physical meaning similar to the critical strain energy release rate, and is determined from the work needed to completely separate a specimen into two halves. The real value of G_F is obtained from a direct tensile test. Because of the difficulties involved in performing the direct uniaxial tensile test, three-point bend tests on notched beams was suggested from the International Union of Testing and Research Laboratories for Materials and Structures (RILEM) for determining the fracture energy [RILEM 1985]. The energy consumed during fracture is a direct function of the load-displacement response. The traditional displacement measurement includes extraneous deformation due to test setup and supports crushing. Unfortunately, the magnitude of this erroneous deformation was found to be of the same order as the actual displacement, leading to inaccurate fracture parameters [Hillerborg 1985; Gopalaratnam, et al. 1991]. To overcome this problem, the load-crack mouth opening displacement (load-*CMOD*) relationship is a more reliable parameter unaffected by the specimen setup and any support crushing.

Until the current study the *CMOD* has primarily been used in closed-loop testing as the control parameter to ensure a stable failure of specimen so that the fracturing activities around peak the load and through the post-peak regions can be clearly observed. However, since the *CMOD* is unaffected by support settlement it is thought that it might be a more reliable fracture parameter.

This investigation found that there is a unique linear relationship between the *CMOD* and the load-line deflection, provided that deflection is measured accurately. The numeric value of the relationship between CMOD and the load-line deflection ,that is, the slope of the line, is shown to be a material property. Such a linear relationship between the deflection and *CMOD* can be understood physically as the constant fracture angle of the material. The proposed concept is then named the Constant Fracture Angle Model (CFAM). The model was evaluated for size dependency using several sizes of notched beams and with different notch lengths. With the proposed model, existing

RILEM recommendations for measuring the fracture toughness of concrete will have to be modified. This theoretical model can easily relate the fracture energy to the observed load-*CMOD* response.

An experimental program is undertaken to examine the relationship between the *CMOD* and load-line deflection. Three different specimen sizes and four different notch depths for each size are evaluated in the three-point bend notched beam test using normal and fiber reinforced concretes. The load, *CMOD*, load-line deflection measured with reference to the neutral axis of the beam, and load-line deflection with reference off the beam (traditional displacement measurement) are monitored to check and investigate the fracture parameters.

Chapter 2 will briefly review the fracture parameters of concrete. The stress intensity factor and energy release rate are described. Experimental methods for determining the fracture parameters are introduced. Several fracture mechanics models are investigated in Chapter 3. The fictitious crack model, the crack band model and the two-parameter fracture model are discussed. At the end of this chapter a new model, relying on the load-*CMOD* relationship, the Constant Fracture Angle Model, is proposed along with an in-depth analysis. Chapter 4 details the specimen preparation, concrete mix and the experimental program and setup. An improved method for measuring beam load-line deflections is introduced. Chapter 5 details the research findings and argues for the adoption of the CFAM. RILEM testing recommendations are criticized. Finally, a summary of the study's conclusions are given in chapter 6.

CHAPTER 2

FRACTURE CRITERIA

2.1 Stress Intensity Factor

A crack in a solid can be divided into three basic types, each associated with a local mode of deformation. Mode I, or the opening mode, is associated with local displacements in which the crack surfaces move directly apart. The sliding mode, or Mode II, is characterized by displacements in which the crack surfaces slide over one another normal to the crack front. Mode III, or the tearing mode, finds the crack surfaces sliding with respect to one another parallel to the crack front. Particularly, if we assume Cartesian coordinates as shown in Figure 2.1, then on the plane $y = 0$

For Mode I

$$\sigma_x \neq 0, \quad \sigma_y \neq 0, \quad \sigma_z \neq 0, \quad \text{and} \quad \tau_{xy} = 0$$

For Mode II

$$\tau_{xy} \neq 0 \quad \text{and} \quad \sigma_y = 0 \tag{2.1}$$

For Mode III

$$\tau_{yz} \neq 0, \quad \sigma_y = 0, \quad \text{and} \quad \tau_{xy} = 0$$

ASTM E616-82 [1982] gives additional details.

The stress field at the crack tip can be treated as one or a combination of these three basic types of stress fields. However, the field of fracture mechanics emphasizes Mode I because usually Mode II and Mode III have been relatively unimportant in fracture testing and application except for testing of adhesive joints. Hence, this investigation is also limited to Mode I. The stresses for the plane strain condition are given by Westergaard [1939] and Irwin [1957].

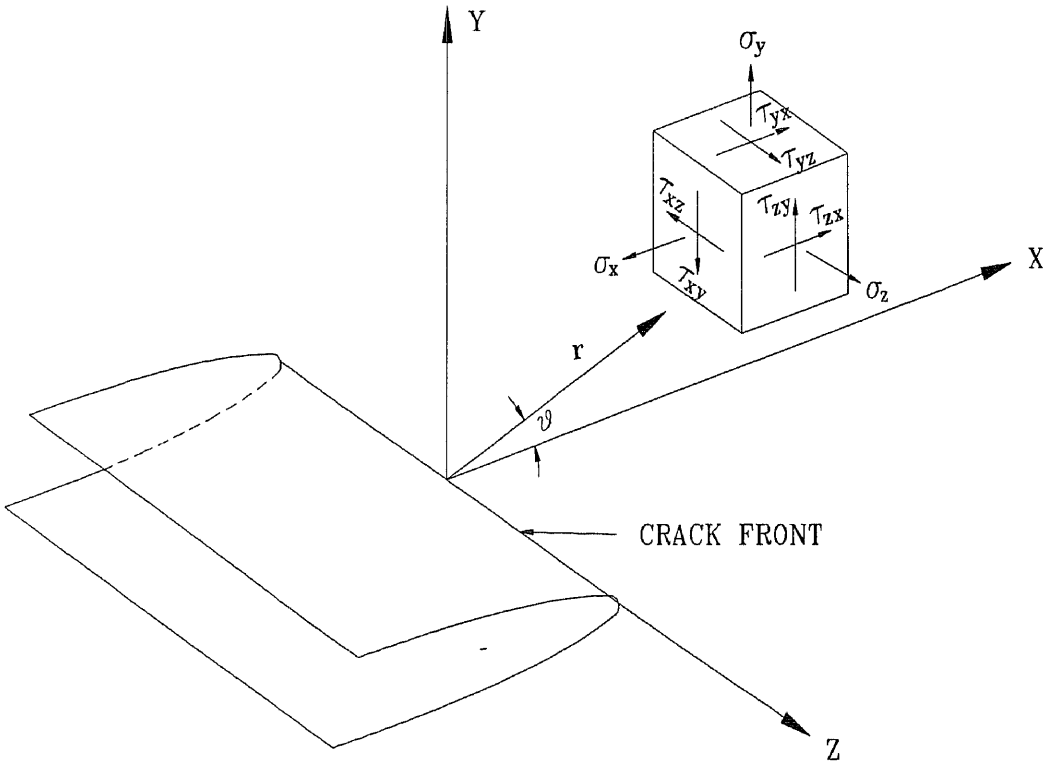

Figure 2.1 Stress component of a body ahead of a crack

$$\sigma_x = \frac{K_I}{(2\pi r)^{1/2}} \cos\frac{\theta}{2}\left(1 - \sin\frac{\theta}{2} \sin\frac{3\theta}{2}\right)$$

$$\sigma_y = \frac{K_I}{(2\pi r)^{1/2}} \cos\frac{\theta}{2}\left(1 + \sin\frac{\theta}{2} \sin\frac{3\theta}{2}\right)$$

$$\sigma_z = \nu\ (\sigma_x + \sigma_y) \qquad (2.2)$$

$$\tau_{xy} = \frac{K_I}{(2\pi r)^{1/2}} \cos\frac{\theta}{2} \sin\frac{\theta}{2} \sin\frac{3\theta}{2}$$

$$\tau_{yz} = \tau_{zx} = 0$$

Each stress component is proportional to a single constant, K_I which is called the stress intensity factor. If the stress intensity factor is known, then entire stress field in the vicinity of crack tip also is known from Equation 2.2. The stress intensity factor completely characterizes the crack tip conditions in a linear elastic material.

The stress intensity factor has the dimension of stress x (length)$^{1/2}$ and is considered to be a single parameter description of the stresses and displacements in the vicinity of crack tip. The subscript I stands for mode I. The stress intensity factor has the following form

$$K_I = \sigma\sqrt{\pi a}\ f(a/w) \qquad (2.3)$$

where a is the crack length, σ is the applied external stress and *f(a/w)* a function of the ratio of the crack length to the thickness, *w*, in the crack plane. *f(a/w)* has unit value for a through crack in an infinite plate and is usually fit to a polynomial expression for a through crack in a finite plate. Stress intensity factors and the finite size polynomials for a number of practical configurations are reported by Tada, Paris and Irwin [1976].

The K_I factor is a LEFM parameter because it is assumed that the material is linearly elastic, isotropic, and homogeneous. Most cementitious materials are neither linear elastic, isotropic nor homogeneous.

Equation 2.2 is exact in the limit as r approaches zero. However, when r is equal to zero a stress singularity exists (the stresses become infinite at the crack tip). In reality at the crack tip the stress may reach an idealized maximum strength or plastic deformation taking place at the crack tip to keep the stresses finite.

2.2 Energy Release Rate

Griffith's proposal to find the fracture strength (i.e., load carrying capacity) of brittle solids in 1920 has become one of the basic equations of linear elastic fracture mechanics. He first postulated the existence of flows or cracks in materials and associated their growth with the consumption of surface energy. Secondly, he suggested that the fracture strength can be found by using an energy balance criterion which has since come to be known as Griffith's energy criterion. He stated that crack propagation will occur if the energy released upon crack growth is sufficient to provide all energy that is required for crack growth. If this is not the case the stress must rise. The condition for crack growth then can be stated as

$$\frac{dU}{da} = \frac{dW}{da} \tag{2.4}$$

where U is the total potential energy, W the energy required for crack growth, and a is the crack length of the through-thickness crack of an infinite plate of unit thickness. Based on the stress field calculation for an elliptical flaw by Inglis [1913], Griffith calculated dU/da as

$$\frac{dU}{da} = \frac{\pi\sigma^2 a}{E'} \tag{2.5}$$

per unit plate thickness, where $E'=E$ for plane stress and $E' = E/(1-\nu^2)$ for plane strain. E is Young's modulus, ν is Poisson's ratio, and σ is the applied normal stress. The derivative dU/da is indicated by G, which is called the strain energy release rate or sometimes referred to as the crack driving force. The strain energy release rate has the dimension of energy per unit crack surface where the crack surface is the product of unit thickness and unit crack extension.

The energy consumed in crack propagation is denoted by $R = dW/da$ which is called crack resistance. Following the Griffith criterion, the energy required to produce a crack is the same for each increment da. This means that R is a constant. Griffith derived this equation for glass which is a very brittle material. A truly brittle material such as glass has a small process zone preceding a crack tip. For this reason R derived by Griffith consists of surface energy only for a single crack. The energy to create the process zone at the crack tip is the required energy for crack propagation and is assumed to be negligible for truly brittle material. Concrete is classified as quasi-brittle material.

Equation 2.5 can written as

$$G = \frac{\pi\sigma^2 a}{E'} \tag{2.6}$$

since R is a constant. Based on linear elastic fracture mechanics the strain energy release rate G can be related with the stress intensity factor as

$$\frac{K_I^{\,2}}{E'} = G = \frac{\pi\sigma^2 a}{E'} \tag{2.7}$$

Thus, if the stress intensity factor is used as a failure criterion, the energy criterion is also satisfied simultaneously.

2.3 Experimental Determination of Fracture Parameters

2.3.1 Critical Stress Intensity Factor

Crack propagation will occur when the combination of stress and strain (stress intensity) reaches a critical value commonly referred to as the critical stress intensity factor, K_{IC}. This value is also referred to as the material fracture toughness, which describes the ability of a material to deform plastically and to absorb energy before and during rupture.

Fracture toughness testing of metals is based on the ASTM E399-83 which gives the standard test method for determining the linear elastic fracture toughness for metallic materials [ASTM 1983]. Since no similar standard exists for concrete, investigators have commonly used the E399 standard as a reference in establishing guidelines for concrete.

The critical stress intensity factor is usually determined from the measured peak load, the initial notch depth and related specimen geometry. A number of investigators have produced the quite different results for K_{IC} in concrete specimens depending on specimen geometry and size. The results of these experiments show that when fracture toughness is evaluated from notched beam specimens using conventional linear elastic fracture mechanics a significant size effect is observed [Francois 1984]. The K_{IC} values increase with increasing specimen size as shown in Figure 2.2. This size effect has been attributed to nonlinear stable crack growth (fracture process zone development) that occurs prior to the peak load. Microcracking, slow crack growth and a large size process zone ahead of the traction-free cracks are all independent characteristics inherent to the inhomogeneous composition of concrete. To accurately determine the critical stress intensity factor the stable crack growth has to be added to the initial notch length.

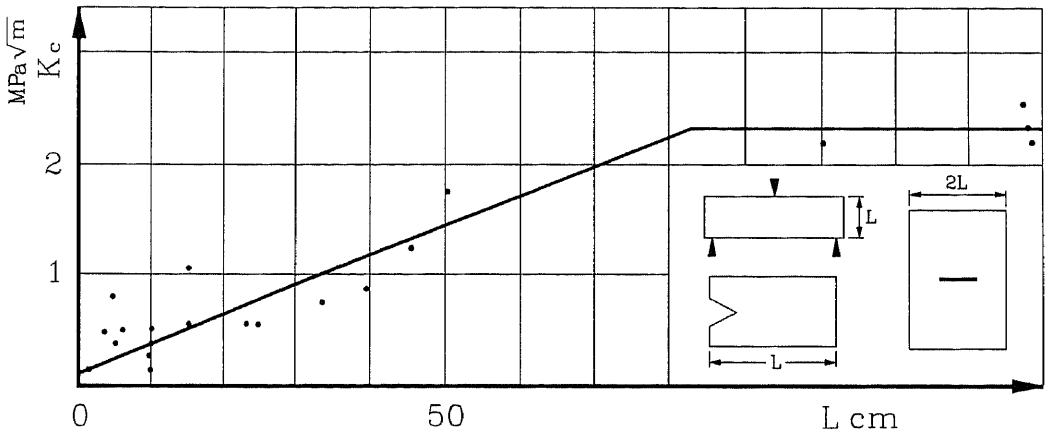

Figure 2.2 Various Results of the fracture toughness K_{IC} [Francois 1984]

2.3.2 Critical Strain Energy Release Rate

The strain energy release rate is defined as the energy required to generate a unit crack surface. As was shown in Equation 2.7, the critical strain energy release rate , G_{IC} can be expressed in terms of the critical stress intensity factor as

$$G_{IC} = \frac{K_{IC}^2}{E'} \tag{2.8}$$

since G_{IC} is closely related to K_{IC}.

2.3.3 Fracture Energy

The fracture energy G_F has a physical meaning similar to the critical strain energy release rate. However, unlike the determination of G_{IC} which is directly related to the peak load, the fracture energy is determined from the work needed to completely separate the specimen into two halves. Peterson [1980; 1981] has described in detail how G_F is determined from three-point bend test on notched beam. The values of G_F should be calculated using direct uniaxial tensile tests. But, due to the difficulties in performing a direct uniaxial tensile test, a three-point bend test on notched beams was proposed by RILEM [1985] to determine the fracture energy of mortar and concrete. From the load-deflection curve obtained in a stable condition, the fracture energy is calculated from the following equation.

$$G_F = \frac{W_o + mg\delta_o}{A_{lig}} \tag{2.9}$$

where W_o is the energy represented by the area under the load-deflection curve, m is the mass of the specimen, g is the acceleration due to gravity, δ_o is maximum deflection of the beam at failure, A_{lig} is area of uncracked ligament and, $mg\delta_o$ represents the energy supplied by the weight of the beam itself.

The energy terms of Equation 2.9 can be described graphically as shown in Figure 2.3. W_o represents the area under the measured load-deflection curve. However, the weight of the beam also contributes energy to the system, and this is represented by W_1 and W_2. W_1 is equal to $mg\delta_o/2$, and it has been shown by Petersson [1981] that the value of W_2 equals W_1.

Based on the RILEM recommendation, G_F values have been experimentally determined by several laboratories [1985]. The G_F values were reported to be dependent on specimen sizes. For specimens with the same notch-depth ratio of 0.5, larger specimen sizes always yield higher values of G_F . For the specimens of the same size with different notch-depth ratio, lower notch-depth ratios give higher G_F values. The size dependency of G_F has been attributed to settlement of the support and, energy consumption taking place outside the noncritical sections.

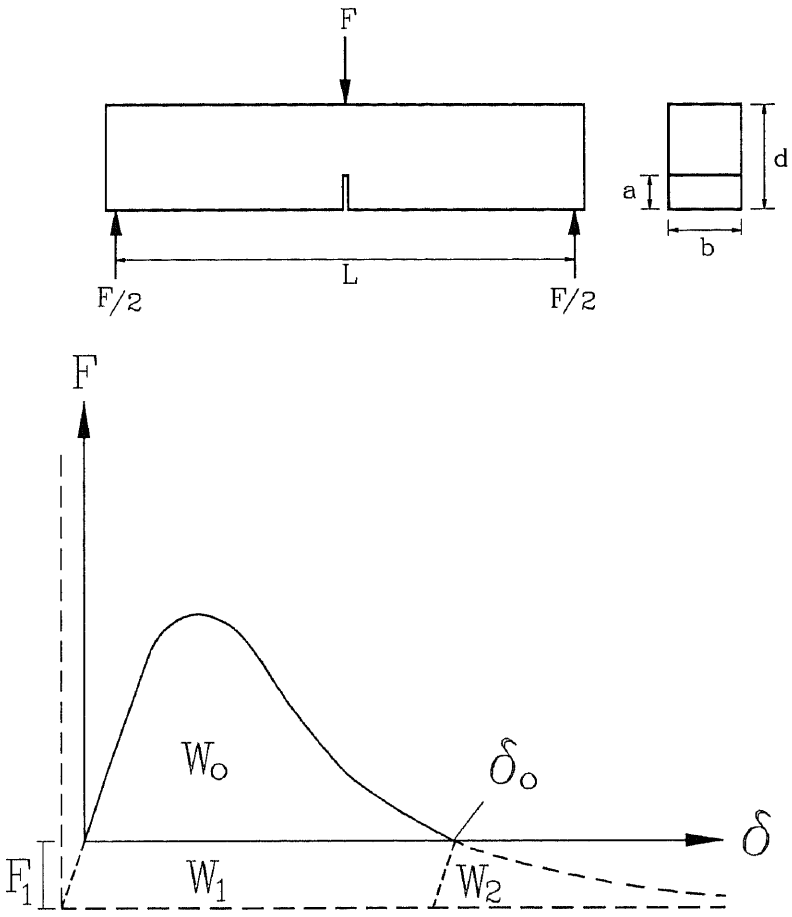

Figure 2.3 RILEM recommendation on determination of fracture energy G_F

CHAPTER 3

FRACTURE MECHANICS MODELS FOR CONCRETE

3.1 Phenomenological Aspects

The phenomenological aspects of the cracking of concrete are well understood and have been confirmed using different methods, including microscopic, X-ray and acoustic emission techniques. These aspect may be described by considering a specimen loaded in tension with prescribed displacement increments. Pre-existing microcracks, mostly located on the aggregate-matrix interface, after initial settling, assume an equilibrium position with respect to the load. As loading increases a process zone develops where bond cracks grow, and, after a specific displacement, microcracks start developing from the existing voids and bridging between the bond cracks. Even at and after the peak load, crack surface are not completely separated, but still resist some tensile stress, probably because of aggregate interlocking effects and traction between surfaces. Slowly, with increasing displacements, stress transfer across the micro cracked region drops to zero, and specimen fails.

A load-displacement (or stress-strain) curve obtained from a displacement controlled test up to failure has two distinct regions: an ascending branch before, and a descending, softening, branch after the peak load (see Figure 3.1). The modulus of elasticity is usually used to characterize the stress-strain relation in the elastic domain, and the peak stress characterizes the tensile strength of an elastic material. However, in the process zone, it has been postulated, after analysis of the softening branch of uniaxial tension test results, that stress and the process zone displacements are functionally dependent through a local, process zone softening constitutive relation. The material in the process zone supports stresses after the peak load which is proportional to the displacement in the process zone. One constitutive relation holds between stress-strain

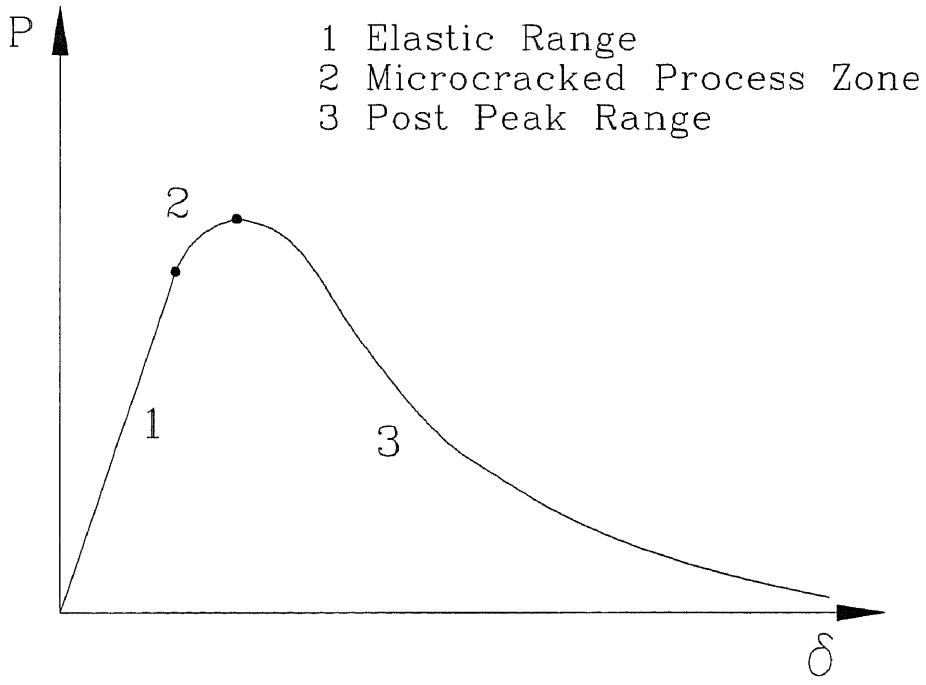

Figure 3.1 Typical load-displacement curve of concrete

in the elastic domain, e.g., modulus of elasticity, and another holds between stress and process zone displacements in the process zone.

3.2 Nonlinear Fracture Models

Many nonlinear fracture models for the fracture process zone have been proposed. Three of the most well-known fracture models are the fictitious crack model (FCM) [Hillerborg 1976], the crack band model (CBM) [Bazant and Cedolin 1979; Bazant and Oh 1983] and the two-parameter fracture model (TPFM) [Jenq and Shah 1985]. These models are all intended to incorporate the nonlinear behavior of concrete into the analysis of the fracture processing of concrete.

3.2.1 Fictitious Crack Model (FCM)

Hillerborg, et al. proposed the FCM for predicting crack growth behavior in concrete. Figure 3.2 shows a typical crack tip stress distribution based on the proposed model. The stress-crack width (σ - w) relationship, considered a material property, defines the post-peak behavior of the material. The pre-peak behavior of the material is assumed to be linear elastic and is defined by a stress-strain (σ - ε) relation. Pre-peak nonlinearity is often neglected for mathematical convenience and, is very small compared to the post-peak inelastic behavior (Figure 3.3) The fracture energy in the FCM is given by

$$G_F = \int_0^w \sigma(w)\, dw \tag{3.1}$$

G_F is one of the key parameters needed to implement the FCM. To determine G_F, a notched beam specimen is tested until it is completely fractured. The amount of total energy absorbed during the fracture process divided by the fracture area will be the fracture energy of the concrete material. Although the actual G_F should be determined

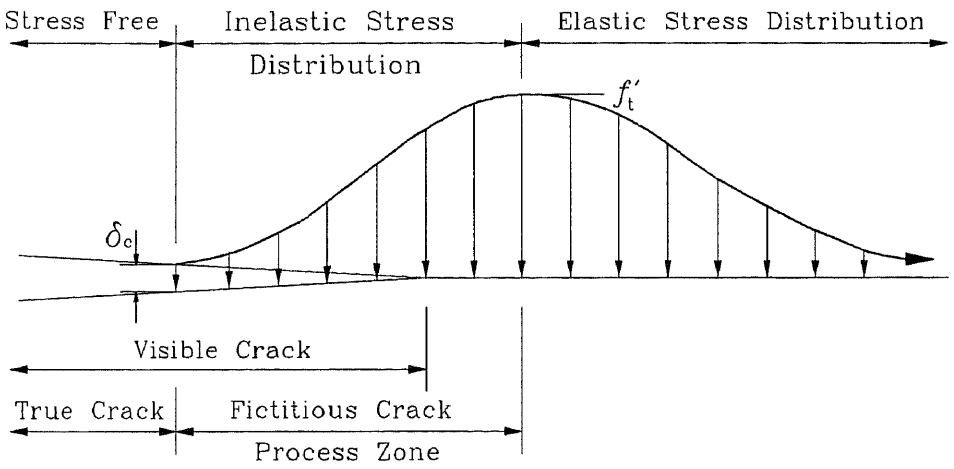

Figure 3.2 Stress distribution in front of a crack tip

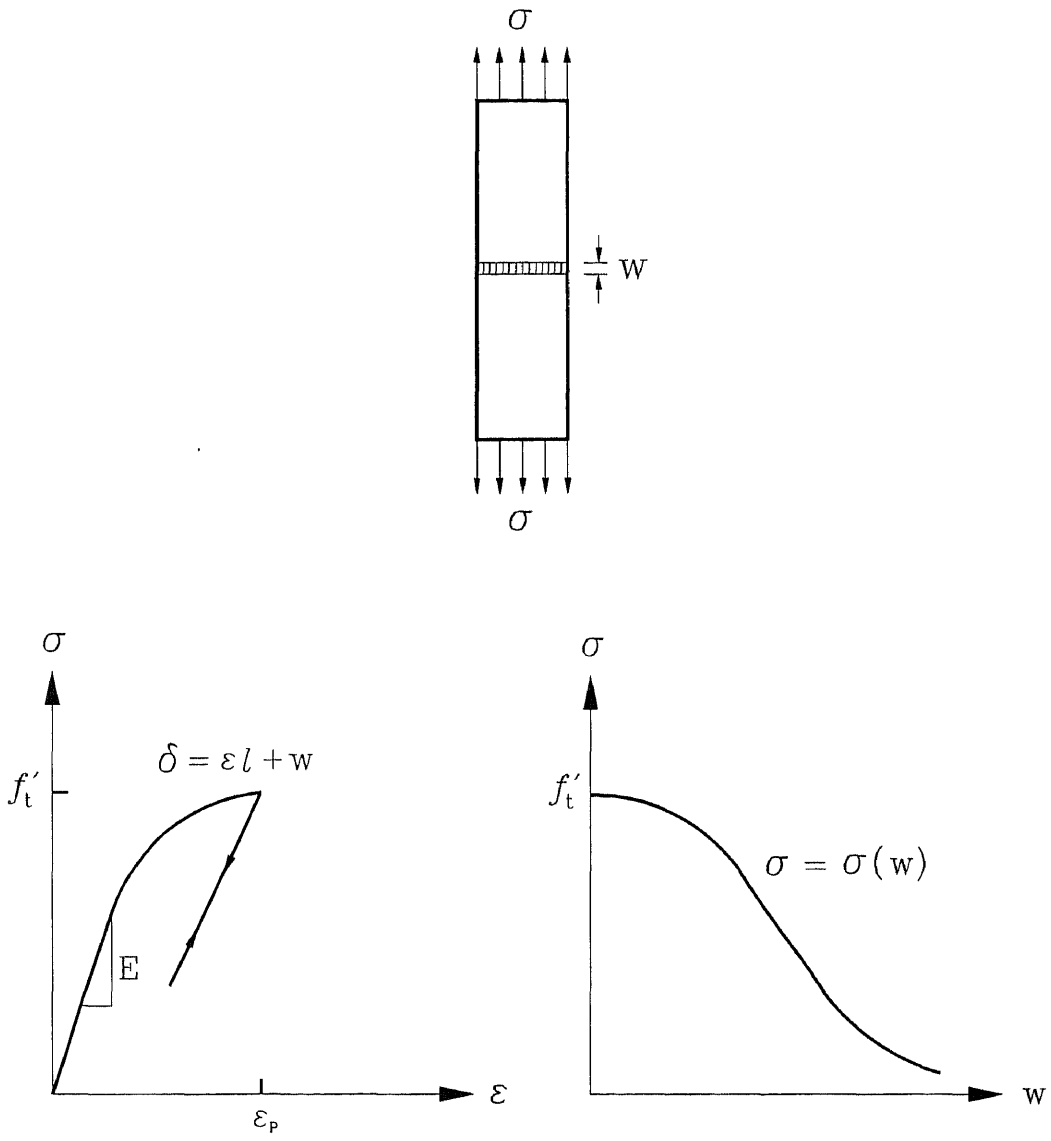

Figure 3.3 Modeling of softening characteristics for FCM

from a direct uniaxial tensile test, due to the difficulty of conducting the direct tensile test most researchers accept the indirect method using a notched beam specimen. The standard notched beam specimen has specific dimensions since it was shown that the fracture parameters measured from notched beam specimens was specimen size dependent. Therefore, the dimension of the test specimen must strictly adhere to the recommended requirements.

Finite element analysis is necessary to implement the model. The model has been shown to correctly predict the experimentally observed size effects for notched and unnotched beam specimens. However, it has been pointed out that the experimentally observed values of fracture energy are dependent on the specimen size. The values obtained by the model are quite sensitive to the uniaxial tensile strength which is not easy to determine. Furthermore, to obtain the peak load of the specimen from the model, the whole load-deflection curve needs to be numerically calculated which requires considerable computational time.

3.2.2 Crack Band Model (CBM)

Arguing that energy can not be dissipated in a diminishing volume of material, Bazant and Cedolin, and Bazant and Oh have proposed the crack band model which treats the localization as a band of distributed cracks. The pre-peak and post-peak behavior are both described by a stress-strain relationship (pre-peak modulus E_1 and post-peak modulus E_2, see Figure 3.4). The width of the crack band w_c can be used to relate the stress-strain response to the fracture energy

$$G_F = w_c \int_0^{\varepsilon_0} \sigma \, d\varepsilon = \frac{w_c^{\,2}}{2} f_t' \left(\frac{1}{E_1} - \frac{1}{E_2}\right) \tag{3.2}$$

The results are similar to those obtained from fictitious crack model if the same values of G_F and f_t' are used in the crack band model. The major difference between the

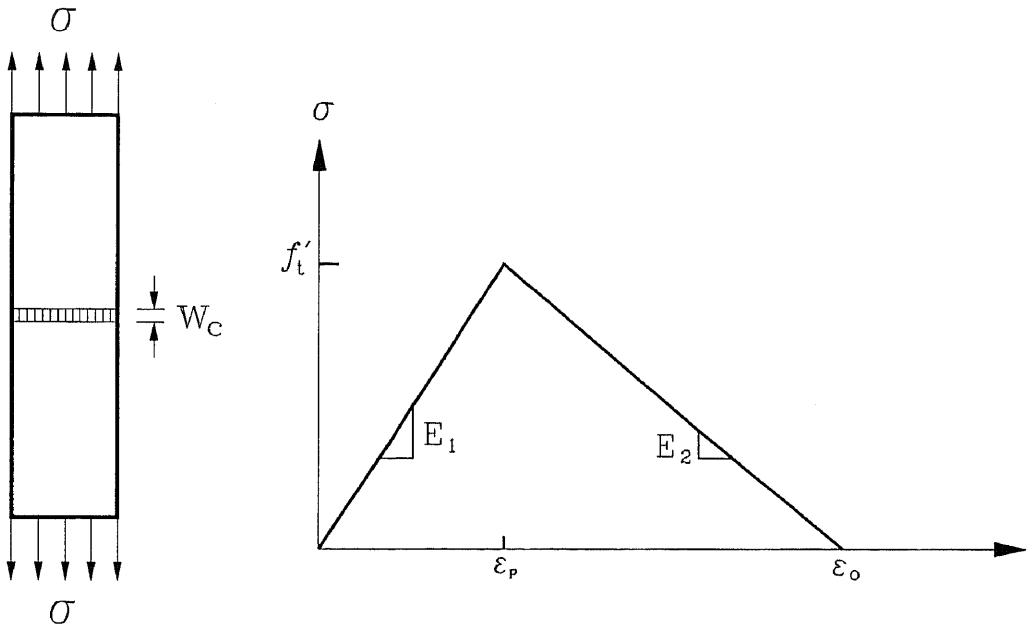

Figure 3.4 Modeling of softening characteristics for CBM

FCM and the CBM models is that the FCM uses a discrete crack concept while the CBM approach is based on the smeared crack principle. In some cases, these two models provided similar results while in some other instances, their predictions are completely different. Nonetheless, the results predicted using both models were claimed to be in good agreement with the observed experimental data which was obtained from testing a standard notched beam specimens.

3.2.3 Two-Parameter Fracture Model (TPFM)

Realizing the tediousness involved in implementation of the FCM, Jenq and Shah proposed the two-parameter fracture model which does not require the post-peak constitutive relation. The stress intensity factor calculated at the tip of the effective crack is determined in such a way that the measured elastic crack mouth opening displacement ($CMOD_e$) is equal to the one calculated using the LEFM. By either assuming the crack profile or directly using the LEFM formulae, the elastic critical crack tip opening displacement ($CTOD_c$) can be obtained. Based on the three-point bend test on different beam sizes and mix-proportion, they concluded that both K_{IC}^{S} and $CTOD_C$ are size independent. Since both fracture parameters are directly determined from LEFM formulae, crack tip singularity is automatically incorporated in the model. Figure 3.5 shows the typical load-*CMOD* response with the two critical fracture parameters.

As proposed in the TPFM, the initial crack growth, the maximum applied load and the corresponding elastic $CMOD_e$ are all directly obtained by experiment. With known specimen geometry and the Young's modulus, the effective elastic crack length a_{eff} can be calculated from the LEFM formulae using measured $CMOD_e$ and the measured maximum load. It is not a simple task to calculate a_{eff} using the LEFM formulae. Iteration or a trial and error method may be needed to obtain a_{eff}. With the calculated effective crack length, K_{IC}^{S} and $CTOD_C$ can be obtained.

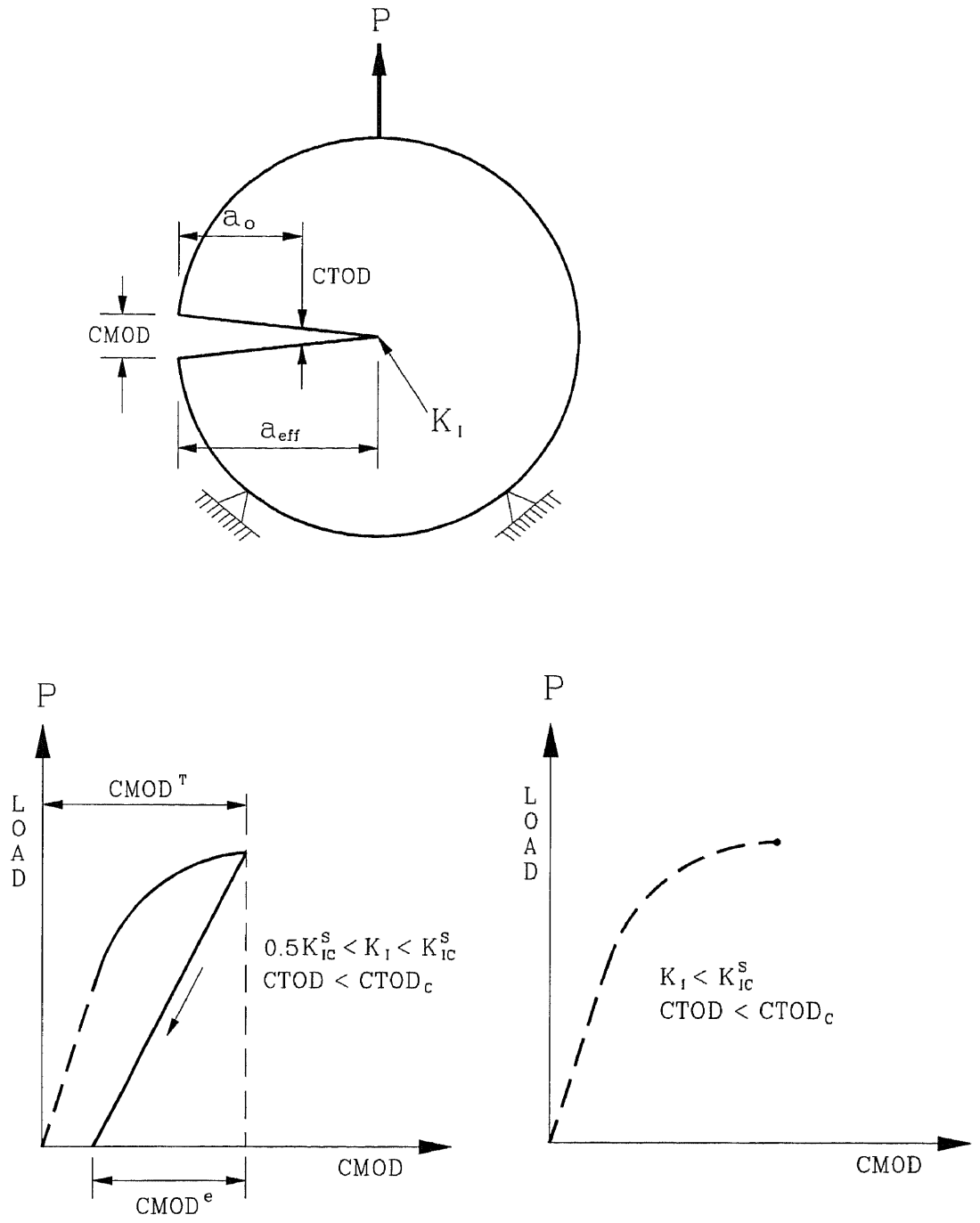

Figure 3.5 Two-parameter fracture model

3.3 Proposed Model (Constant Fracture Angle Model)

For the fictitious crack model and the crack band model, a constitutive relationship in terms of stress versus separation, which is only obtained by performing the direct tensile testing, is required and finite element analysis is needed to implement the models.

In the case of two-parameter fracture model, the effective elastic crack length a_{eff} is calculated from LEFM formulae using measured $CMOD_e$ and the measured maximum load. Unloading around the maximum load point, which needs a special care, is required to obtain the $CMOD_e$. Additionally, it is not a simple task to calculate a a_{eff} using LEFM formulae.

The indirect method for obtaining fracture energy G_F, suggested by RILEM, requires the whole load versus deflection curve from a deformation controlled test. It is hard to obtain a stable fracture in the case of beam under the deformation control. To obtain an accurate load-line deformation, a special test setup which eliminates the effect of support crushing on the load-line deflection is required.

The constant fracture angle model can be used to predict the process zone growth and fracture energy. It is based on the relationship between the *CMOD* and the load-line deflection in the post-peak region.

To develop the constant fracture angle model, the LEFM concept and the relationship between *CMOD* and load-line deflection in the post-peak region were used. *CMOD* measurement is used because it is more accurate than load-line deflection measurement since *CMOD* is not affected by support crushing.

3.3.1 Linear Elastic Range

For the initial portion, the linear elastic range, the LEFM concept can be used to obtain a *CMOD* - load-line deflection (see Figure 3.6 for the LEFM based equations used). Crack mouth opening displacement is

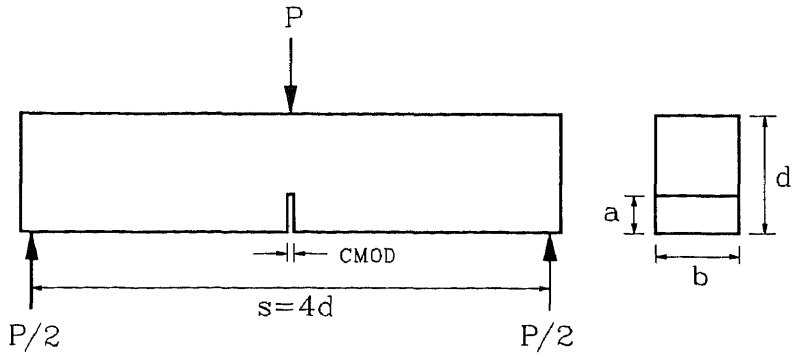

Stress Intensity Factor (K_I)

$$K_I = \frac{6P}{bd}\sqrt{\pi a}\, f(A)$$
$$f(A) = 1.090 - 1.735A + 8.20A^2 - 14.18A^3 + 14.57A^4$$
$$A = \frac{a}{d}$$

Crack Mouth Opening Displacement (*CMOD*)

$$CMOD = \frac{6Psa}{Ebd^2} V_1(A)$$
$$V_1(A) = 0.76 - 2.28A + 3.87A^2 - 2.04A^3 + \frac{0.66}{(1-A)^2}$$

Additional Load-Line Displacement due to Crack

$$\delta_{crack} = \delta_{total} - \delta_{nocrack}$$
$$\delta_{crack} = \frac{\sigma}{E} s V_2(A)$$
$$V_2(A) = \left(\frac{A}{1-A}\right)^2 (5.58 - 19.57A + 36.82A^2 - 34.94A^3 + 12.77A^4)$$

Figure 3.6 Three-point bend notched specimen and the associated LEFM formulas

$$CMOD = \frac{6Psa}{Ebd^2} V_1(A) = \frac{6Ps}{Ebd} AV_1(A) \tag{3.3}$$

where P is the load, *s*, the span of the beam, *b*, the beam width, *d*, the beam height, *a*, the initial notch depth, *A*, is the ratio of the initial notch length to beam depth (*a/d*) and $V_1(A)$ is a correction factor dependent on the loading type and the ratio of the span to the beam depth. In the case of the three-point bend test specimen for *s/d* = 4, $V_1(A)$ is

$$V_1(A) = 0.76 - 2.28A + 3.87A^2 - 2.04A^3 + \frac{0.66}{(1-A)^2} \tag{3.4}$$

The total load-line deflection of beam δ_P can be expressed as

$$\delta_P = \delta_c + \delta_u = \delta_c + (\delta_b + \delta_s) \tag{3.5}$$

where δ_c is the deflection due to the crack, δ_u the deflection of the uncracked beam, δ_b the deflection due to bending and δ_s the deflection due to shear.

$$\delta_b = \frac{Ps^3}{4Ebd^3}$$

$$\delta_s = \frac{3(1+\nu)Ps}{5Ebd} \tag{3.6}$$

$$\delta_c = \frac{3Ps^2}{2Ebd^2} V_2(A)$$

where

$$V_2(A) = \left(\frac{A}{1-A}\right)^2 (5.58 - 19.57A + 36.82A^2 - 34.94A^3 + 12.77A^4)$$

Substituting Equation 3.6 into Equation 3.5 and dividing by Equation 3.3 gives

$$\frac{\delta_p}{CMOD} = \frac{30dsV_2(A) + 5s^2 + 12(1+\nu)d^2}{120daV_1(A)} \tag{3.7}$$

The value of $\nu = 0.2$ is commonly used for concrete and other cementitious materials. The derived formula should leave *s/d* as a variable but substitute the value of $\nu = 0.2$. Hence

$$\frac{\delta_p}{CMOD} = \frac{30(s/d)\,V_2(A) + 5(s/d)^2 + 14.4}{120\,A\,V_1(A)} \tag{3.8}$$

If *s/d* = 4 as recommended by ASTM standard, Equation 3.8 is

$$\frac{\delta_p}{CMOD} = \frac{V_2(A)}{A\,V_1(A)} + \frac{23.6}{30\,AV_1(A)} \tag{3.9}$$

Based on the Equation 3.7, load-line deflection can be expressed as follows:

$$\delta_p = S_1 \,.\, CMOD \tag{3.10}$$

where S_1 is a constant determined by loading type and specimen geometry.

3.3.2 Post-Peak Range (Crack Propagation Range)

To derive the relationship between *CMOD* and load-line deflection, following assumptions are used.

(1) Fracture energy, G_F, is a material property.

(2) Microcracks are fully developed at the peak load, and when a crack propagates the size of fracture process zone does not change.

(3) The ratio of the change of *CMOD* to the change in crack length is constant (see Figure 3.7).

The incremental ratio of load-line deflection to *CMOD*, $\Delta\delta_P / \Delta CMOD$, can be expressed using chain rule as

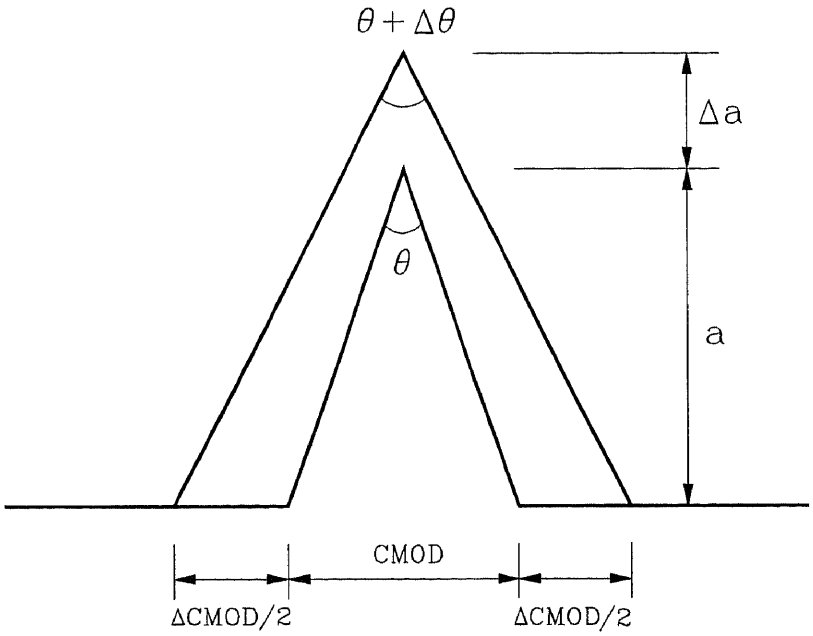

Figure 3.7 Relation between *CMOD* and crack length *a*

$$\frac{\Delta \delta_P}{\Delta CMOD} = \frac{\Delta a}{\Delta CMOD} \frac{\Delta \delta_P}{\Delta a} \tag{3.11}$$

The energy needed to produce a small increment of load-line deflection, ΔU is

$$\Delta U = P \, \Delta \delta_P \tag{3.12}$$

Substituting Equation 3.12 into Equation 3.11 gives

$$\frac{\Delta \delta_P}{\Delta CMOD} = \frac{\Delta a}{\Delta CMOD} \frac{\Delta U}{P \, \Delta a} \tag{3.13}$$

Since $\Delta U / \Delta a$ is the fracture energy G_F, Equation 3.13 changes to Equation 3.14.

$$\frac{\Delta \delta_P}{\Delta CMOD} = \frac{G_F}{b P} \frac{\Delta a}{\Delta CMOD} \tag{3.14}$$

The right side of above equation is a constant because G_F is a material property and $\Delta a / \Delta CMOD$ is a constant. Therefore, $\Delta \delta_P / \Delta CMOD$ is a constant.

$$\frac{\Delta \delta_P}{\Delta CMOD} = S_2 \tag{3.15}$$

S_2 is a material property, independent of size, and can be determined by experiments.

3.3.3 Microcracked Process Zone

In the microcracked process zone, microcracks start and fully develop at the peak load. Near the peak load, the coalescence of microcracks produces a traction-free surface in the process zone. This traction-free surface continuously changes causing a continuous slope change from S_1 to S_2 (see Figure 3.8).

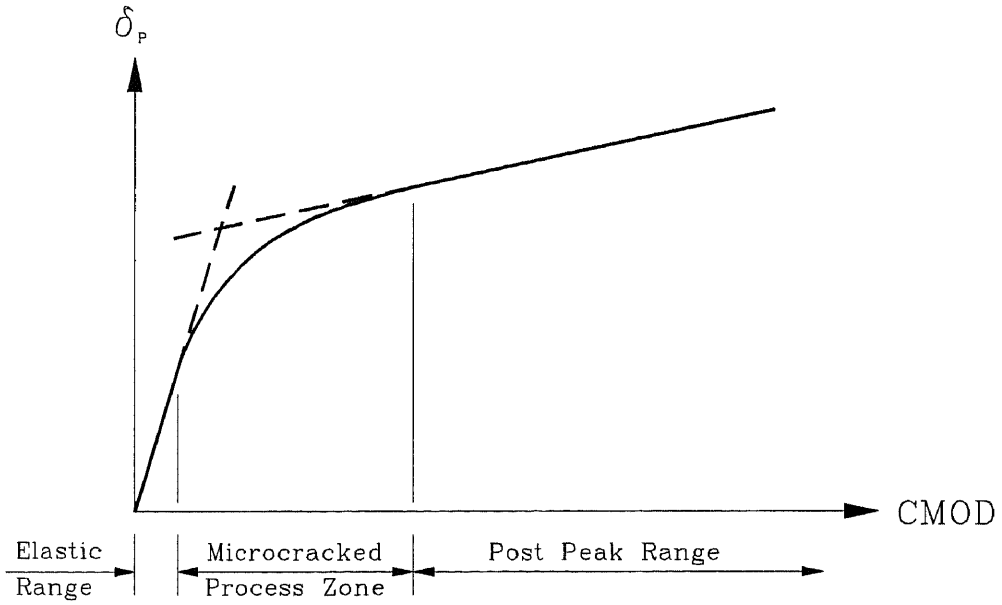

Figure 3.8 δ_p-*CMOD* curve

The change of slope, ΔS, due to increment of load ΔP is

$$\Delta S = \frac{\Delta \delta_P}{\Delta CMOD} = \frac{\frac{\partial \delta_P}{\partial a}\Delta a + \frac{\partial \delta_P}{\partial P}\Delta P}{\frac{\partial CMOD}{\partial a}\Delta a + \frac{\partial CMOD}{\partial P}\Delta P} \tag{3.16}$$

Rearranging the Equation 3.16 with respect to P by using LEFM gives Equation 3.17 (see Appendix A).

$$P = \frac{P_{\max}}{1+K} \tag{3.17}$$

where

$$K = \frac{K_1 \frac{3s^2}{2Ebd^3} - K_2 \frac{6s}{Ebd^2}\Delta S}{\frac{\partial CMOD}{\partial P}\Delta S - \frac{\partial \delta_P}{\partial P}}\Delta a \tag{3.18}$$

$$K_1 = \left[2\frac{A}{(1-A)^3}(5.58 - 19.57A + 36.82A^2 - 34.94A^3 + 12.77A^4) + \left(\frac{A}{1-A}\right)^2(-19.57 + 73.64A - 104.82A^2 + 51.08A^3)\right] \tag{3.19}$$

$$K_2 = V_1(A) + A\left(-2.28 + 7.74A - 6.12A^2 + \frac{1.32}{(1-A)^3}\right) \tag{3.20}$$

Δa in Equation 3.18 is calculated from the *CMOD* value at the peak load using Equation 3.3 (see Figure 3.9). Equation 3.3 is a polynomial function of A requiring a numerical method for the determination of A. Since $a = a_o + \Delta a$, Δa can be found. So, Equation 3.17 can be solved for P, which is the proportional limit in this case.

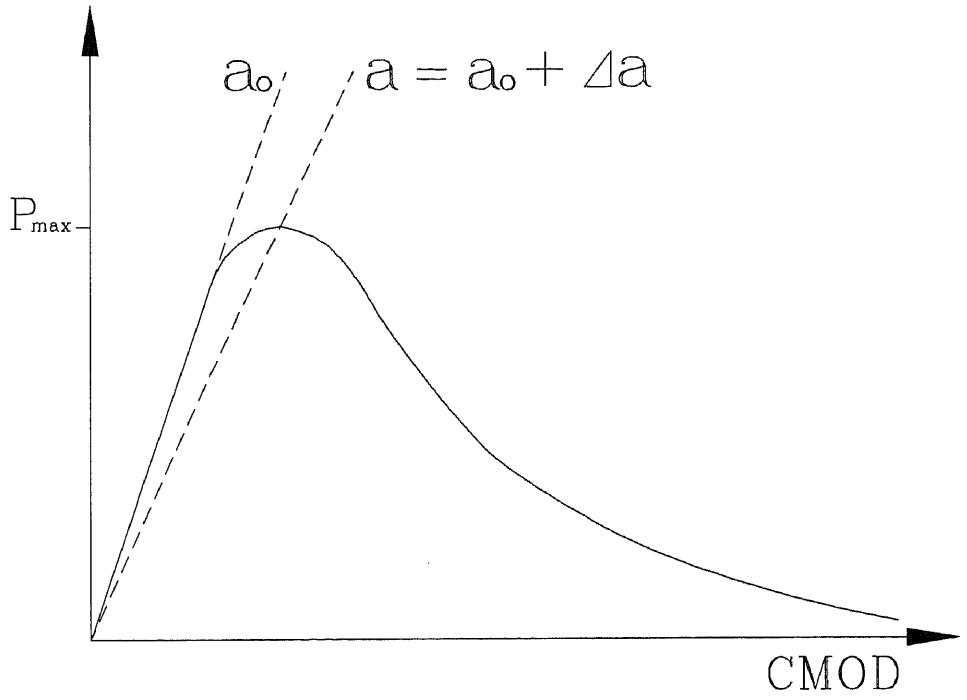

Figure 3.9 Schematic diagram for determination of Δa

CHAPTER 4

EXPERIMENTAL PROGRAM

The experimental program was designed to verify the proposed model, and to evaluate the applicability of the LEFM concept to concrete. Notched beams of three different sizes and a variety of different initial notch lengths were prepared and tested under *CMOD* controlled loading in a 100,000 pound MTS closed loop servo controlled testing machine.

Concrete mix-proportion, casting and curing procedure were kept constant for all specimens in order to minimize scatter by keeping the concrete as consistent as possible for all samples. Type III cement was used with sand passing through sieve #4 and coarse basalt of 3/8 in. maximum size. Mix-proportion by weight is presented in Table 4.1. An additional series of fiber reinforced concrete beam were also tested to determined the effect of fiber addition on S_2 values [Tindukasiri 1993]. The results are shown in Table 5.3.

ϕ 3 x 6 in cylinder specimens were cast in disposable plastic molds to determine compressive strength and Young's modulus. The small and medium size beams were cast in plexy-glass molds and large size beams were cast in plywood molds. The beam dimensions are shown in Table 4.2. All specimens, both beams and cylinders, were cured in a lime saturated water until one day before testing, when they were taken out to cut the notch, attach the clip gage holders and the beam mounted reference frame holders. The compressive strength and modulus of elasticity were determined according to standard procedures, ASTM C-39 and ASTM C-469. The specimens were tested at the age of 8 days. The average compressive strength and average Young's modulus were 5720 psi and 3120 ksi, respectively.

The main object of the experimental program is to obtain the complete load vs.

Table 4.1 Mixture design

Materials	Specific Gravity	Weight Ratio	Weight (lb/yd^3)
Cement	3.15	1	674
Sand	2.60	2	1348
Aggregate	2.83	2.50	1685
Water	1.00	0.53	357

Table 4.2 Size of specimens and number of specimens tested

Beam Size	Width (b) (inch)	Depth (d) (inch)	Length (L) (inch)	Span (s) (inch)	Weight (pound)
Small (S)	3	3	15	12	11.5
Medium (M)	3	4.5	21	18	24.3
Large (L)	3	6	27	24	42.1

Series	Notch depth / Beam depth (a/d)			
	0.2 (N2)	0.33 (N3)	0.4 (N4)	0.5 (N5)
Small (S)	2	3	3	3
Medium (M)	2	3	3	3
Large (L)	3	3	3	3

CMOD and load vs. load point deflection curves then, to use them to analyze the material behavior for a variety of testing configurations. Table 4.2 summarizes the testing program. The parameter *a/d* is the ratio of the notch depth, *a*, to the depth of the beam, *d*. The three beam sizes and the four *a/d* ratios were selected to investigate how the beam size and the notch depth effect the fracture parameters.

All samples were tested on an MTS system 442 closed-loop servo controlled hydraulic testing machine. The closed-loop system enabled the use of *CMOD* control under which the *CMOD* was increased at a rate of 0.002 inch per minute. This mode of control produces a controlled failure of the sample allowing all parameters of interest to be measured. Raw data was recorded using a PC based IBM data acquisition and control board (DACA) running the Unkelscope data acquisition program sampling at 2 Hz.

Before testing the exact beam dimensions, notch depth and span were measured and recorded. Samples were installed on a flexural testing stand as shown in Figure 4.1. The sample supports were semicircles. The load was applied through a swiveling arrangement that adjusted for sample irregularities.

Four measurements were made and electronically recorded by the data acquisition system. The load was measured by a 5,000 pound load cell, calibrated and traceable to NIST just prior to the start of the testing, attached to the MTS piston. Two measurements of the load-line deflection were made. The first, LVDT1, was made using a linear variable differential transformer (LVDT), resolving 0.05 inch into ten volts, measuring between the beam and a reference frame attached at the level of one half the unnotched depth, as seen in Figure 4.1. The reference frame was hinged above one support and free to move laterally above the other. The second measurement, LVDT2, was a conventional measurement, made also using an LVDT with the same range characteristics of LVDT1, between the beam and a fixture attached to the test stand. The last measurement was of the *CMOD*, made with an MTS clip-on gage which resolved 0.02 inch into ten volts.

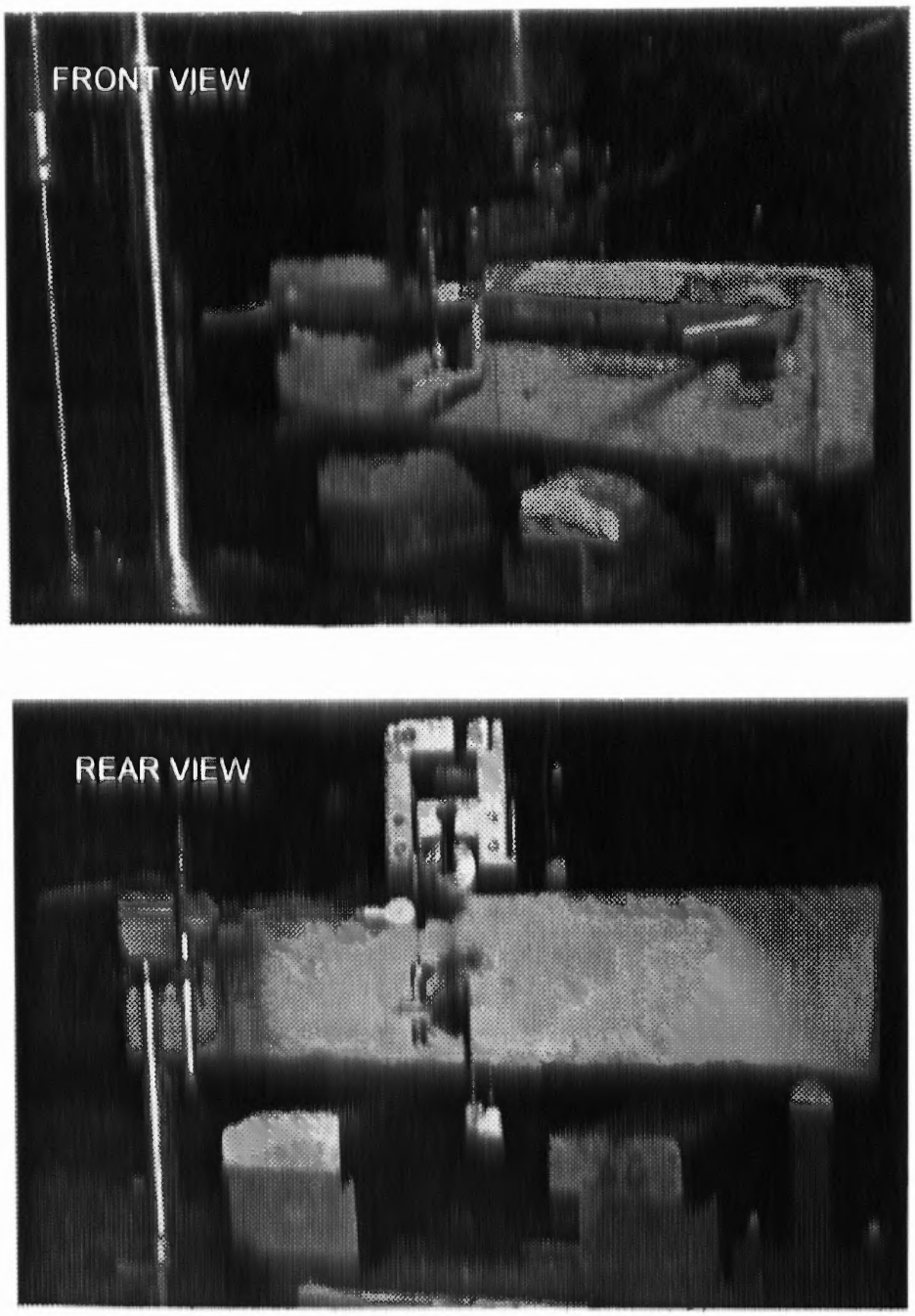

Figure 4.1 Testing setup

CHAPTER 5

RESULTS AND DISCUSSIONS

5.1 Extraneous Deformations

The experimental results allow for a direct comparison of two methods of measuring the beam deflection. The results indicate that measurements made from a reference off the beam tend to overstate the actual deflection. Figures 5.1 through 5.3 show some typical load deflection curves. These figures, as well as additional figures for other specimens found in appendix B, show that for all beam sizes and all notch conditions the deflection measured with reference off the beam (LPD2) measured with LVDT2 is greater than deflections measured with reference to the neutral axis of the beam (LPD1) measured with LVDT1. The same phenomena was also observed in Figure 5.4 on fiber reinforced composites [Gopalaratnam, V. S., S. P. Shah, G. B. Batson, M. E. Criswell, V. Ramakrishnan, and M. Wecharatana 1991]. No one else seems to have considered this issue. This effect, which has heretofore been believed to be negligible, is primarily due to crushing at the supports. Unfortunately, the magnitude of the extraneous deformation is of the same order as the actual beam deflection. The failure to consider the extraneous deformations has led to some misconceptions about the behavior of concrete samples. Table 5.1 shows the ratio of LPD2 to LPD1 at the peak load. In all cases, except in a couple of cases when LVDT2 failed to move, LVDT2 always indicates a larger deformation than LVDT1 so the ratio always exceeds 1.0, which shows that LPD2 always includes some degree of settlement. It can also be noted that after the peak load no further crushing occurs. A calculation of fracture energy, G_F, based upon this overstated deflection will give an inflated value. When this value is used in fictitious crack model erroneous results will occur. For accurate measurement of beam deflections a reference attached to the beam, of the sort used in these experiments, should be used.

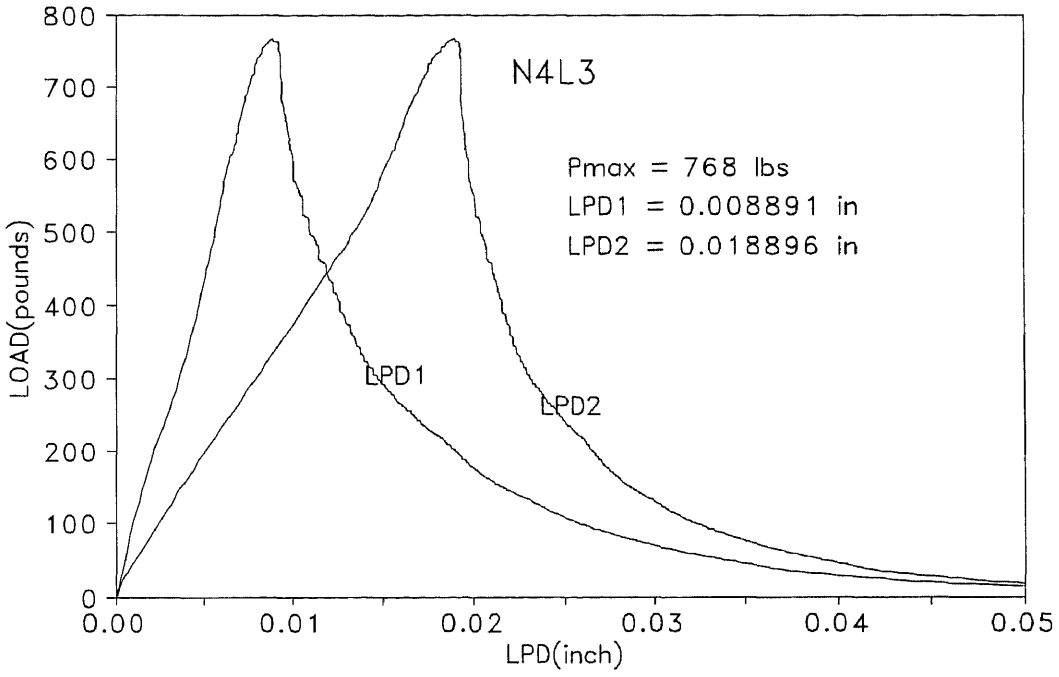

Figure 5.1 Load-deflection relationship (N4L3 b x d x s x a = 3 x 6 x 24 x 2.4)

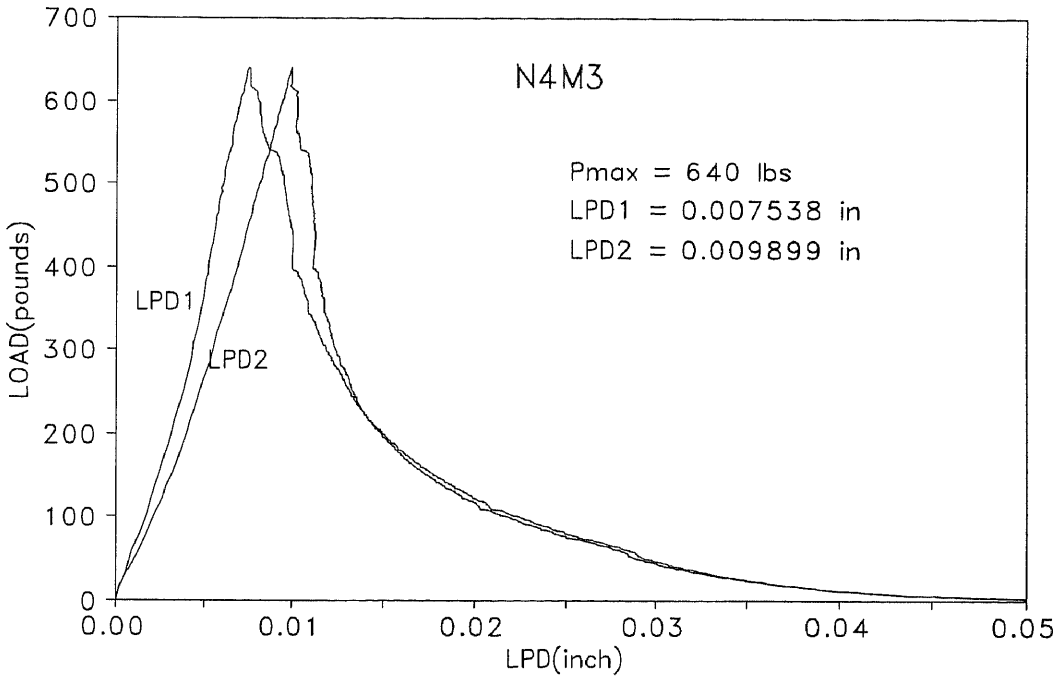

Figure 5.2 Load-deflection relationship (N4M3 b x d x s x a = 3 x 4.5 x 18 x 1.8)

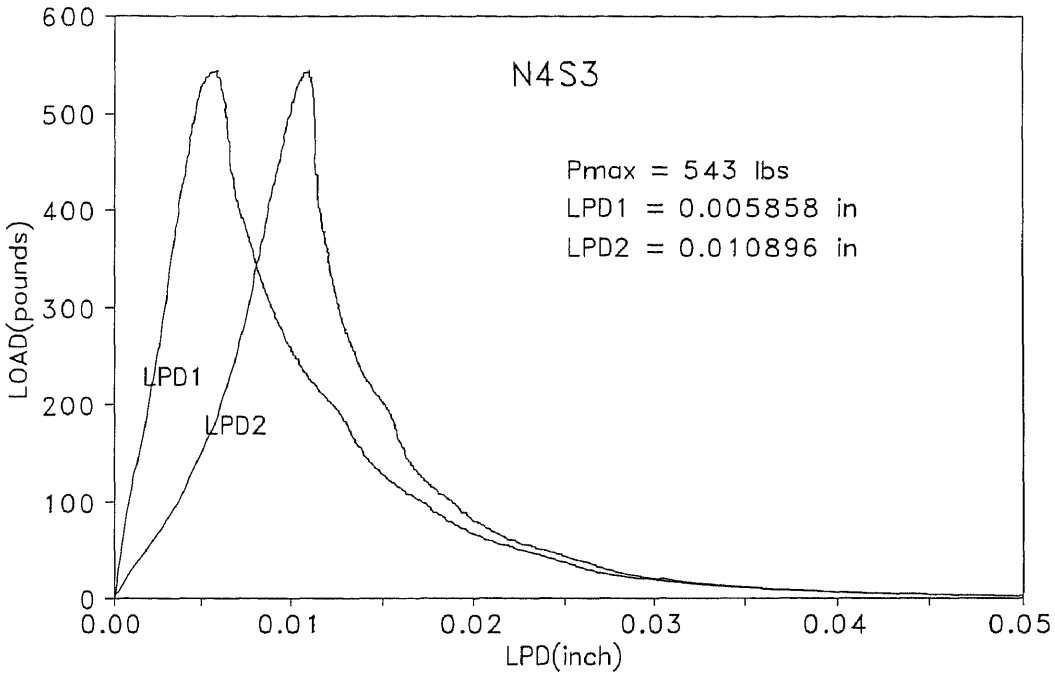

Figure 5.3 Load-deflection relationship (N4S3 b x d x s x a = 3 x 3 x 12 x 1.2)

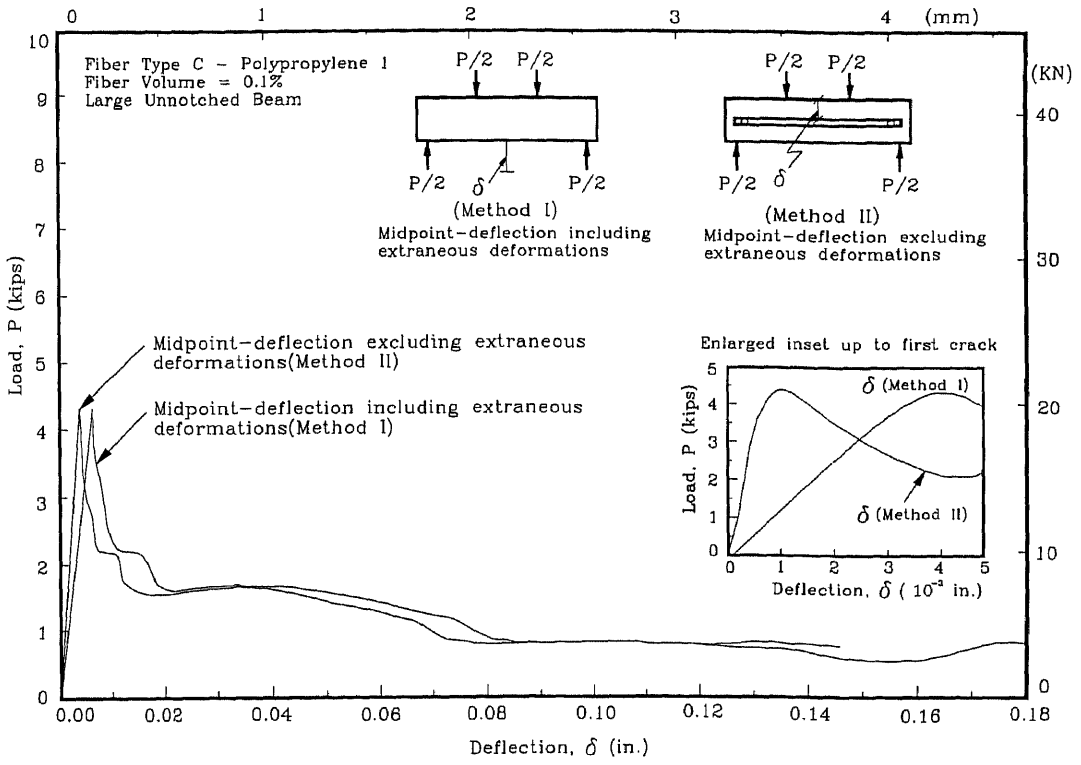

Figure 5.4 Load-deflection plots for a large unnotched polypropylene fiber reinforced beam

Table 5.1 The ratio LPD2 to LPD1 at the peak load

Specimen	LPD1 (10^{-3} inch)	LPD2 (10^{-3} inch)	LPD2/LPD1
N2L1	7.29	8.21	1.13
N2L2	6.74	13.77	2.04
N2L3	6.54	16.14	2.47
N2M1	6.05	16.91	2.79
N2M2	5.43	11.17	2.06
N2S1	4.92	8.78	1.79
N2S2	5.19	12.61	2.43
N3L1	7.83	8.06	1.03
N3L2	7.03	LVDT2 failed to move	
N3L3	8.06	21.34	2.65
N3M1	6.53	11.44	1.75
N3M2	7.23	LVDT2 failed to move	
N3M3	6.75	10.87	1.61
N3S1	6.15	11.43	1.86
N3S2	5.58	11.60	2.08
N3S3	5.05	7.63	1.51
N4L1	8.74	20.09	2.30
N4L2	8.06	12.25	1.52
N4L3	8.89	18.90	2.13
N4M1	7.02	16.74	2.39
N4M2	7.04	10.73	1.52
N4M3	7.54	9.90	1.31
N4S1	4.96	10.95	2.21
N4S2	5.19	12.15	2.34
N4S3	5.86	10.89	1.86
N5L1	9.27	15.49	1.67
N5L2	9.88	19.97	2.02
N5L3	9.40	18.13	1.93
N5M1	6.37	7.15	1.12
N5M2	6.74	12.65	1.88
N5M3	7.17	13.23	1.84
N5S1	3.88	7.66	1.97
N5S2	3.86	8.86	2.30
N5S3	2.61	6.46	2.47

Until the current study the *CMOD* has primarily been used to control the specimen loading rate. However, since the *CMOD* is relatively unaffected by support settlements it was thought that it might be a more reliable fracture parameter. Figure 5.5 is a typical load-*CMOD* curve, it has a strong resemblance to typical load-deflection curves. Typical deflection-*CMOD* curves are shown in Figure 5.6. The lower curve shows the LVDT2 deflection vs. *CMOD* and apparently there is no clear relationship between the deflection and the *CMOD*. Strikingly, the LVDT1 deflection vs. *CMOD* shows a simple bilinear relationship. This study is the first to observe this relationship because it has eliminated the extraneous deformations and is thereby able to relate the correct load-line deflection to the *CMOD*.

5.2 Bilinear Deflection-*CMOD* Relationship

The deflection-*CMOD* relationship, shown in Figure 5.6 is observed to be bilinear. The first linear part, S_1, shows the deflection-*CMOD* relationship in the linear elastic region. As the microcracked process zone develops the slope gradually changes until the peak load is reached. At this point the process zone is completely developed and cracking begins. The second linear portion, S_2, is sustained as the crack grows until complete failure. Since nonlinearity of concrete is mainly a contribution of the microcracked zone, the size of the process zone in front of the crack tip remains fully developed and shifts forward as the macrocrack grows. It can be noted on Figure 5.6 that if the LVDT2 deflection (LPD2), which includes the extraneous deformations, is considered this relationship is not at all apparent.

S_2 is the slope of the deflection-*CMOD* curve as the crack propagate through the specimen. The values of S_2 for the concrete used in this study are shown in Figure 5.7. It can be seen from Table 5.2 that the values, which average 0.8720, are very consistent. Table 5.3 shows the resuls from the fiber reinforced beam tests [Tindukasiri 1993].These results shows consistantly higher values for S_2 which are due to the presence of

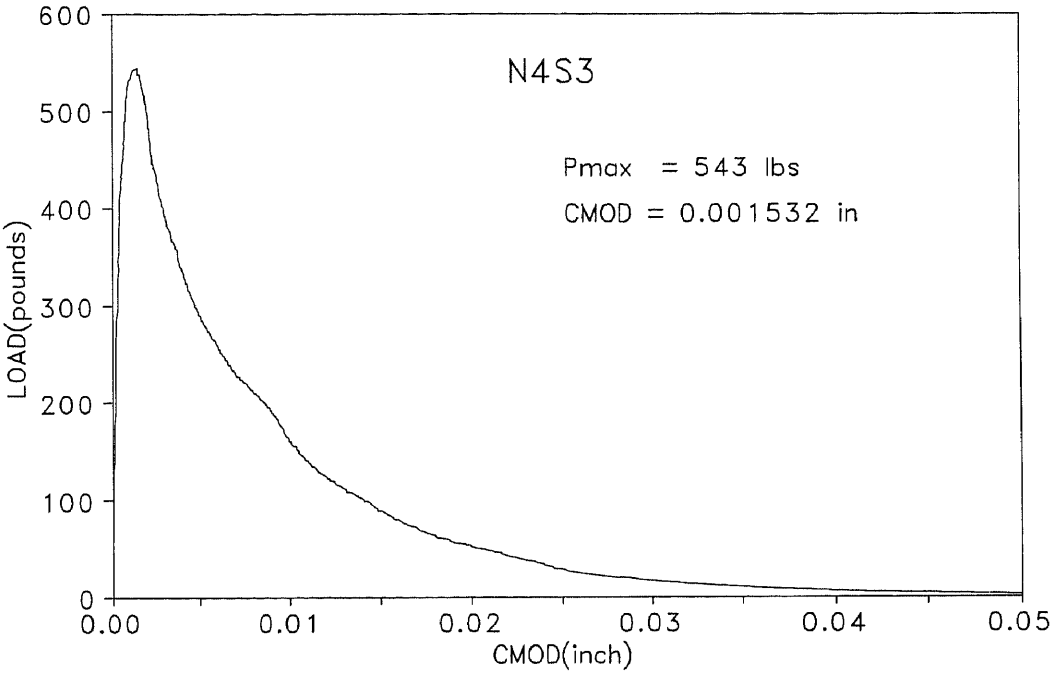

Figure 5.5 Typical load-*CMOD* curve

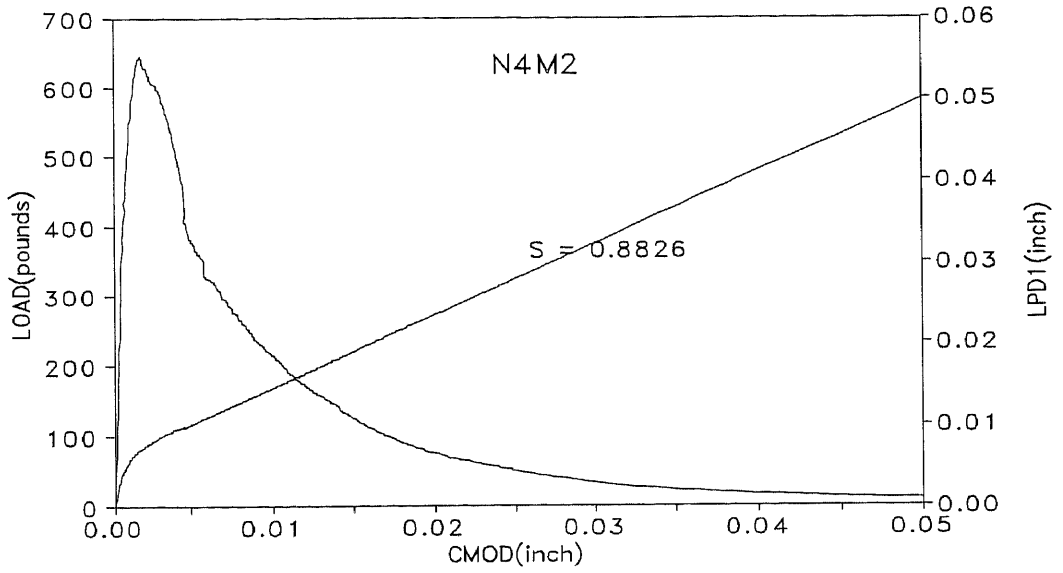

LVDT1

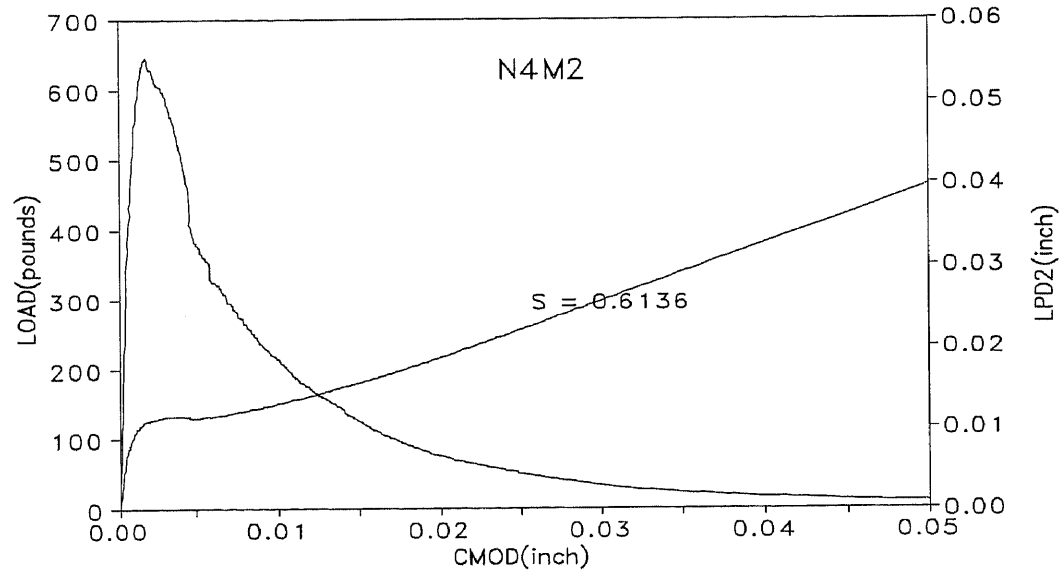

LVDT2

Figure 5.6 Load-*CMOD*-deflection relationship

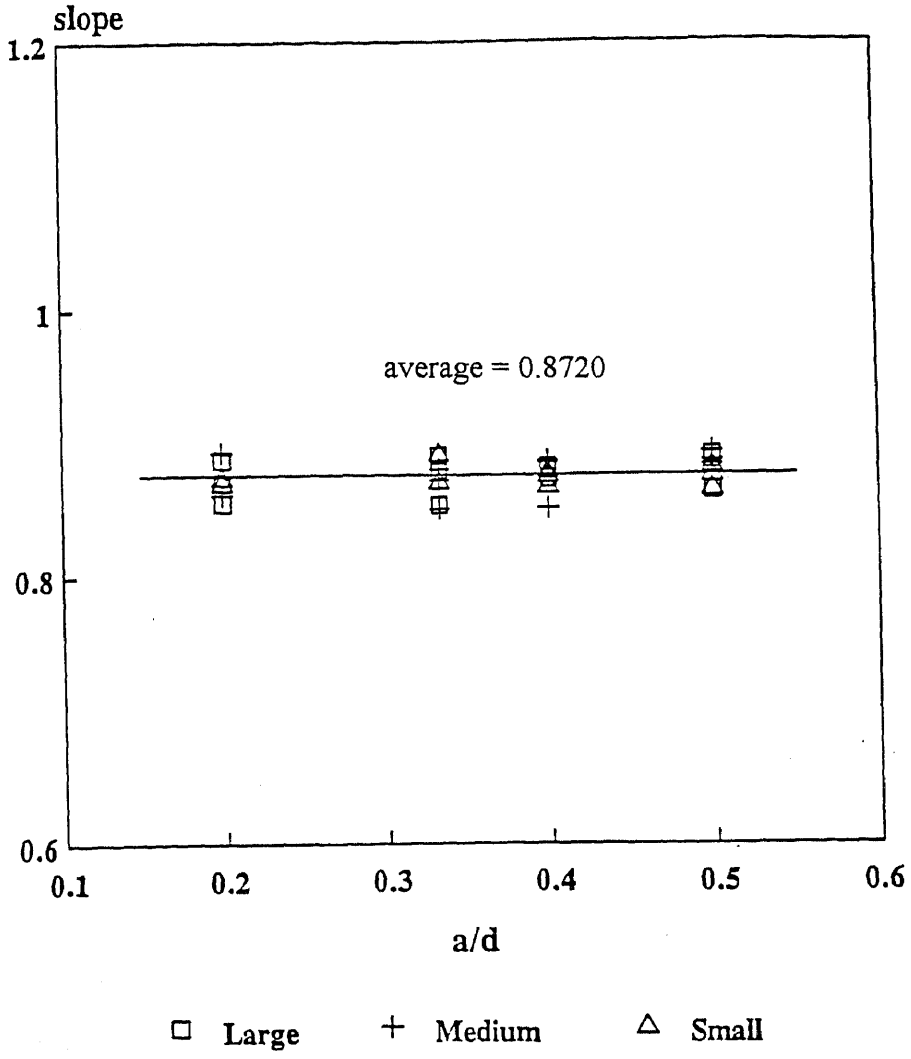

Figure 5.7 Observed values of S_2

Table 5.2 The values of S_2

Specimen	S_2	Average
N2L1	0.8505	
N2L2	0.8694	0.8676
N2L3	0.8828	
N2M1	0.8548	
N2M2	0.8824	0.8686
N2S1	0.8670	
N2S2	0.8698	0.8684
N3L1	0.8860	
N3L2	0.8752	0.8710
N3L3	0.8519	
N3M1	0.8722	
N3M2	0.8520	0.8656
N3M3	0.8727	
N3S1	0.8649	
N3S2	0.8757	0.8763
N3S3	0.8882	
N4L1	0.8728	
N4L2	0.8764	0.8758
N4L3	0.8781	
N4M1	0.8455	
N4M2	0.8826	0.8700
N4M3	0.8819	
N4S1	0.8673	
N4S2	0.8869	0.8786
N4S3	0.8816	
N5L1	0.8631	
N5L2	0.8512	0.8671
N5L3	0.8870	
N5M1	0.8854	
N5M2	0.8756	0.8846
N5M3	0.8927	
N5S1	0.8627	
N5S2	0.8756	0.8707
N5S3	0.8739	
		0.8720

Table 5.3 Results of fiber reinforced concrete testing

Specimen	Fiber type	Wt. of Fiber (lb)	Max. Load (lb)	E (ksi)	S_2
D05B1	0.5%, 1 in	3.43	1420.90	2963.95	1.04
C05B1	0.5%, 1 in	3.43	1640.63	3079.91	1.05
H05B1	0.5%, 1 in	3.43	1494.14	2933.90	0.94
D10B2	1.0%, 2 in	6.86	4165.04	3031.31	0.98
D10B1	1.0%, 1 in	6.86	1469.73	3044.80	0.98
C10B1	1.0%, 1 in	6.86	2036.13	3241.10	1.00
H10B1	1.0%, 1 in	6.86	2187.50	3084.98	0.88
D15B1	1.5%, 1 in	10.29	4155.27	3210.21	1.06
C15B1	1.5%, 1 in	10.29	2646.48	3210.21	0.97
H15B1	1.5%, 1 in	10.29	2778.32	3202.59	0.96

fibers.This indicates that S_2 is a material property in the same way that G_F is a material property.

The fracture energy is usually taken as the area under the load-deflection curve. However, there have been many discrepancies for determining the fracture energy for cementitious composites, now thought to have been due, in large part, to the difficulties encountered making exact measurements of the load-line deflection. These problems can be eliminated using the bilinear concept because the *CMOD* value is used to calculate the fracture energy. The fracture energy is computed using the following expression:

$$G_F = \int_0^{\delta_0} P \, d\delta = C \int_0^{\delta_0} P \, dCMOD \tag{5.1}$$

where C is S_1 in the elastic range and S_2 in the post-peak region as long as S_1 and S_2 are constants.

5.3 Pe/Pmax Limit

The ratio of load at the elastic limit, Pe, to the maximum load, Pmax, indicates the extent of the fracture process zone. The assumption of the current fracture mechanics theory, as it applies to concrete, is that up until the proportional limit there is no process zone or microcracking. After the proportional limit the process zone gradually develops until it reaches its full extent when the peak load is reached and the macrocrack begins to propagate. A small ratio of Pe/Pmax would indicate a relatively larger process zone than a larger ratio for the same configuration. Values of Pe/Pmax, calculated using the model, plotted against *a/d* for all samples are shown in Figure 5.8. This figure shows that as the notch depth increases the ratio of Pe/Pmax increases until it exceeds 1.0. This result explains the presence of the so called "size effect" in notched beams observed by other researchers. The size effect is used to explain the decrease in fracture energy as deeper notches are made. For smaller notches the process zone is relatively larger than for larger

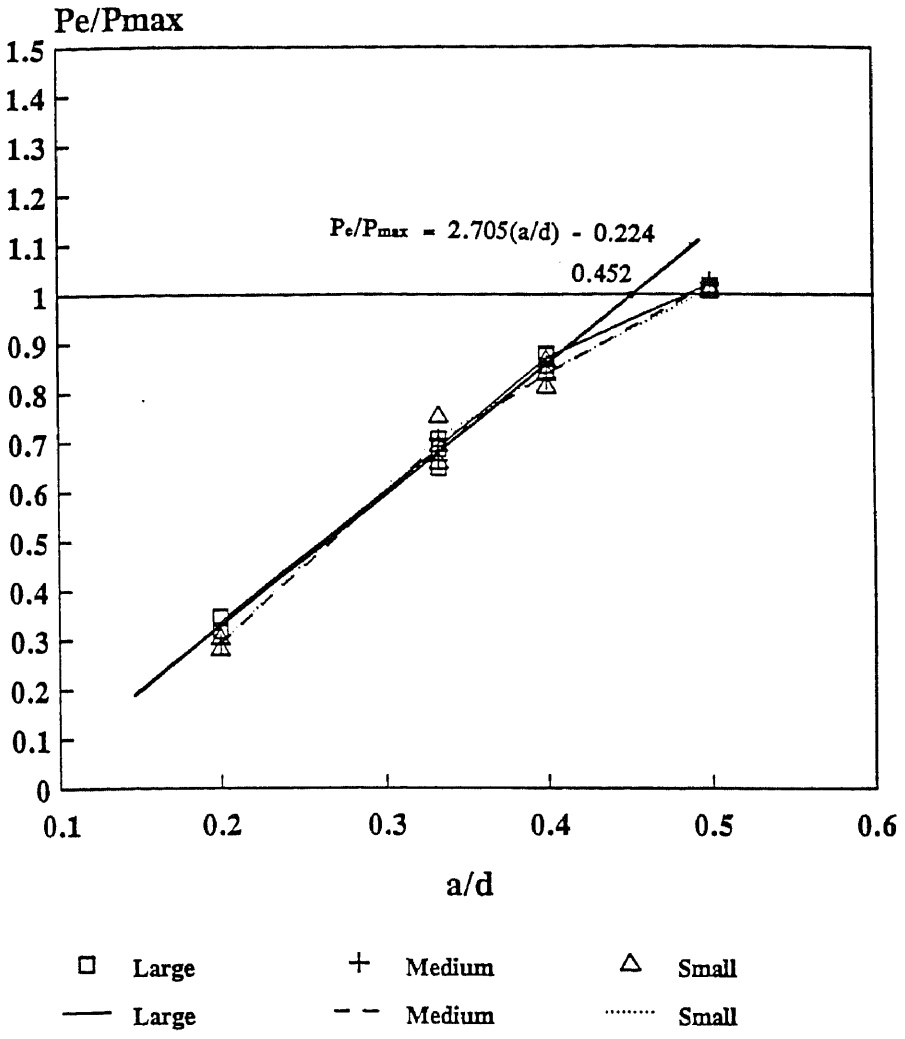

Figure 5.8 Relationship between Pe/Pmax and *a/d*

notches. This leads to the observation that as the notch size increases the fracture energy decreases.

Conceptually, the value of Pe/Pmax can not be greater than 1.0. However, when *a/d* equal to 0.5 Pe/Pmax was found to exceed 1.0. The interpretation of this result is that at this notch size the process zone for the beam reaches the confinement of the compression zone before being fully developed. Therefore, the zone can develop no further so cracking starts relatively earlier than for other notch sizes resulting in a lower peak load and lower fracture energy.

RILEM's committee on fracture toughness of concrete recommends that when measuring the fracture energy of concrete using three-point bend notched beams *a/d* should be 0.5. Presently, most researchers follow these recommendations. The results of this study indicate that there may be problems with this recommendation and that the recommendation for *a/d* should be changed. An *a/d* less than 0.4, which is *a/d* when Pe/Pmax is appropriately 1.0 should be used.

5.4 Fracture Energy

Fracture energy is a very important parameter used in studying the properties of concrete. It is the amount of energy required to extend a crack a unit area through the material. If the fracture energy is known then the behavior of a structure can be predicted more accurately. The most widely used fracture mechanics model for analyzing structures is the fictitious crack model (FCM). To implement FCM the G_F, a material property, needs to be considered. If this value is not determined accurately the analysis will not be correct. Figure 5.9 shows G_F calculated based on the LVDT2 measurements. The value of G_F is seen to be widely scattered, an effect not uncommon when many measurements of the same sort are made. Figure 5.10 shows G_F calculated based on the bilinear concept. The value is seen to be essentially constant until it drops when *a/d* equals 0.5, for the reasons discussed above in the section on Pe/Pmax. The constant

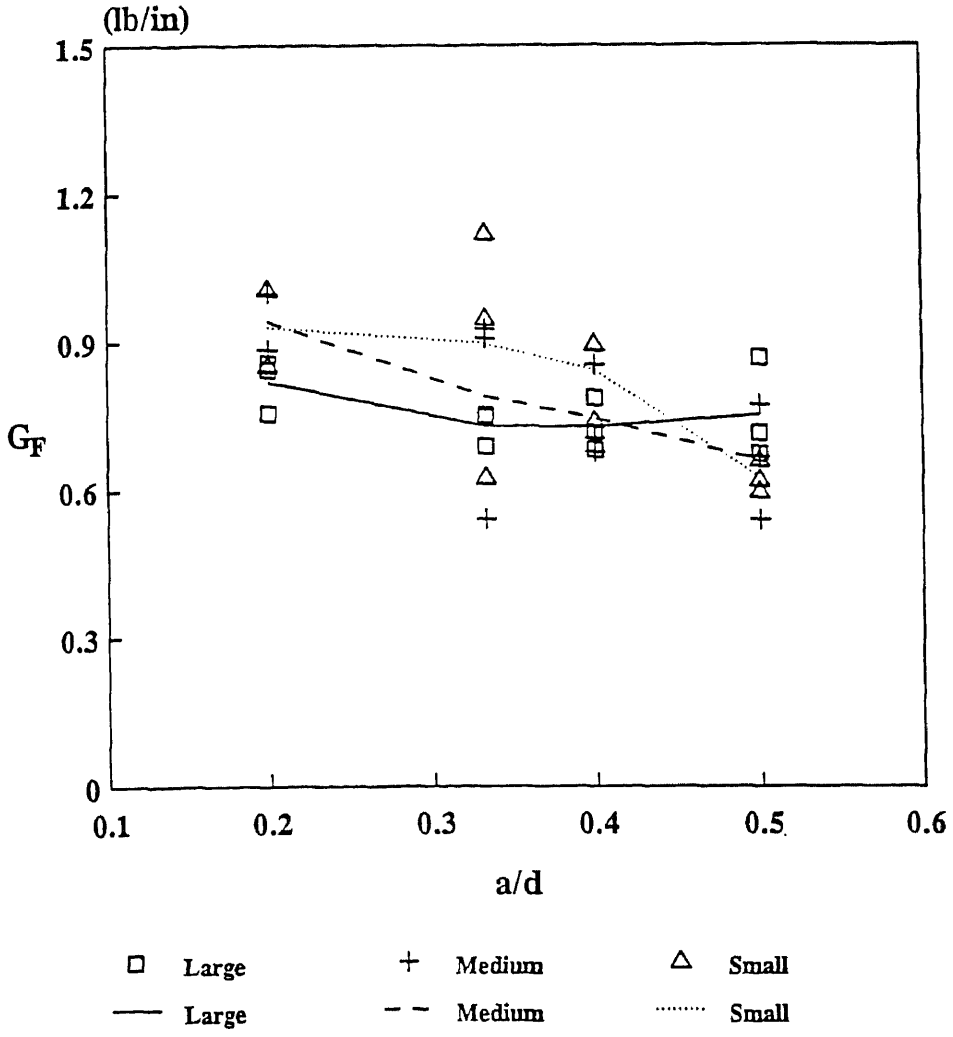

Figure 5.9 Fracture energy calculated based on deflection measurement

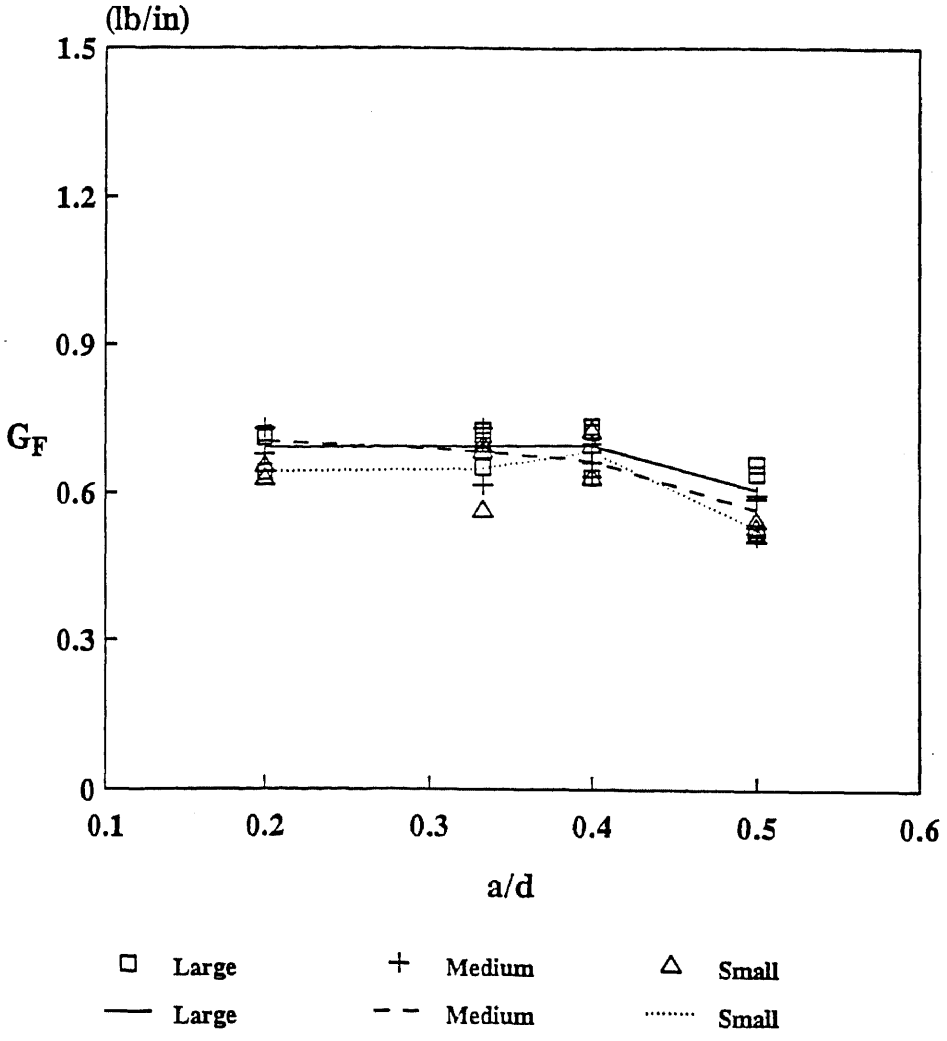

Figure 5.10 Fracture energy calculated based on proposed model

value shows that this method is independent of the specimen size and notch depth. Again, since the fracture energy is one of the parameters sought when testing using RILEM recommendations, the current recommendation of 0.5 needs to be changed.

5.5 Fracture Toughness

In order to apply LEFM to concrete the microcracked zone (process zone) must be incorporated into the analysis. In the elastic region there is no process zone. In the region between the proportional limit and the peak load the process zone gradually grows until it reaches its full size. After the peak, the zone shifts upwards as the macrocrack grows but the size of the process zone remains unaltered unless a confinement is encountered. If the fracture toughness is a material property its value should be a constant, regardless of the specimen or the notch size. Figure 5.11 shows the K_{IC} value computed based on LEFM without consideration of the process zone. It is derived solely on the basis of the initial notch depth and the peak load. The value of the fracture toughness seems to vary with the notch depth.

Figure 5.12 shows the fracture toughness computed on the basis of the effective crack length, which accounts for the process zone. It shows K_{IC} to be constant except until the initial notch depth ratio is 0.5 where it seems to drop. The reason for this is that because the ligament of the beam has become so small the process zone reaches the compression zone of the beam before the process zone reaches its full size. Therefore, the load can not be increased further so the corresponding K_{IC} value is smaller than for the other notch sizes.

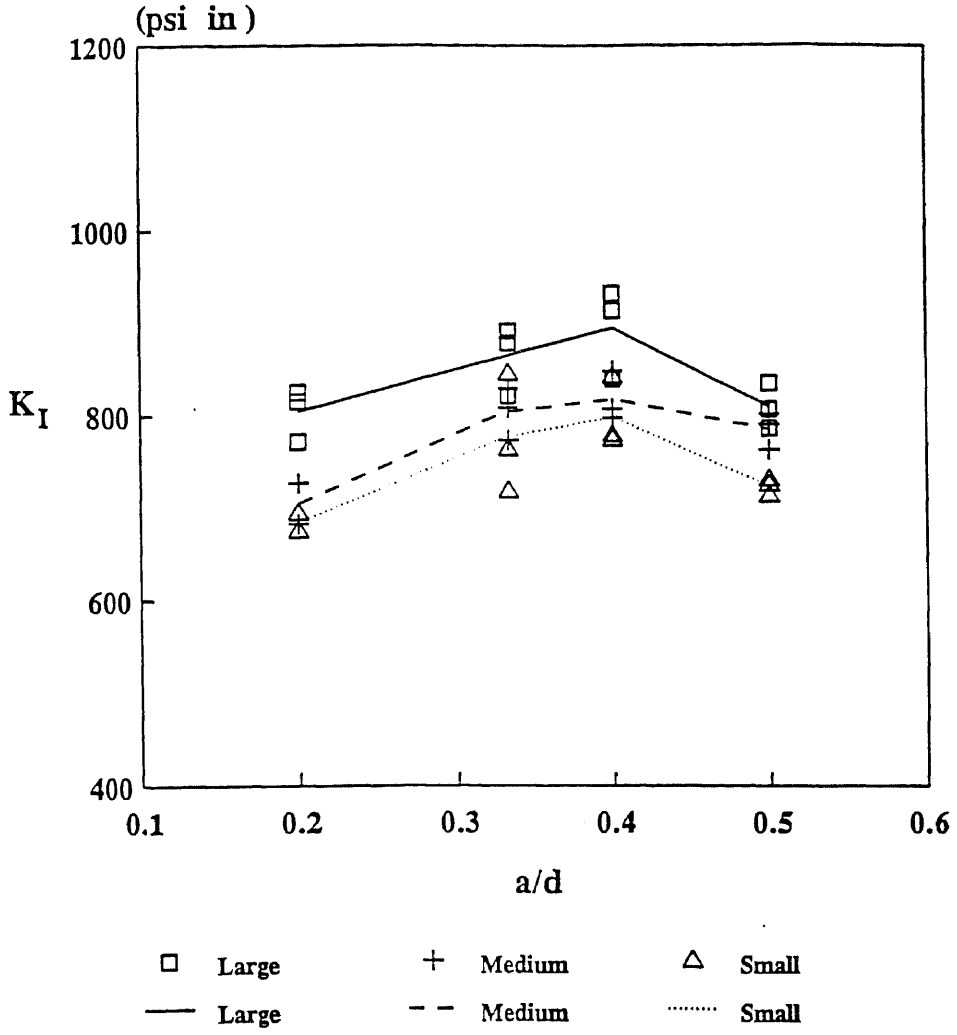

Figure 5.11 Fracture toughness (K_{IC} value) based on LEFM without considering the effect of the microcracked process zone

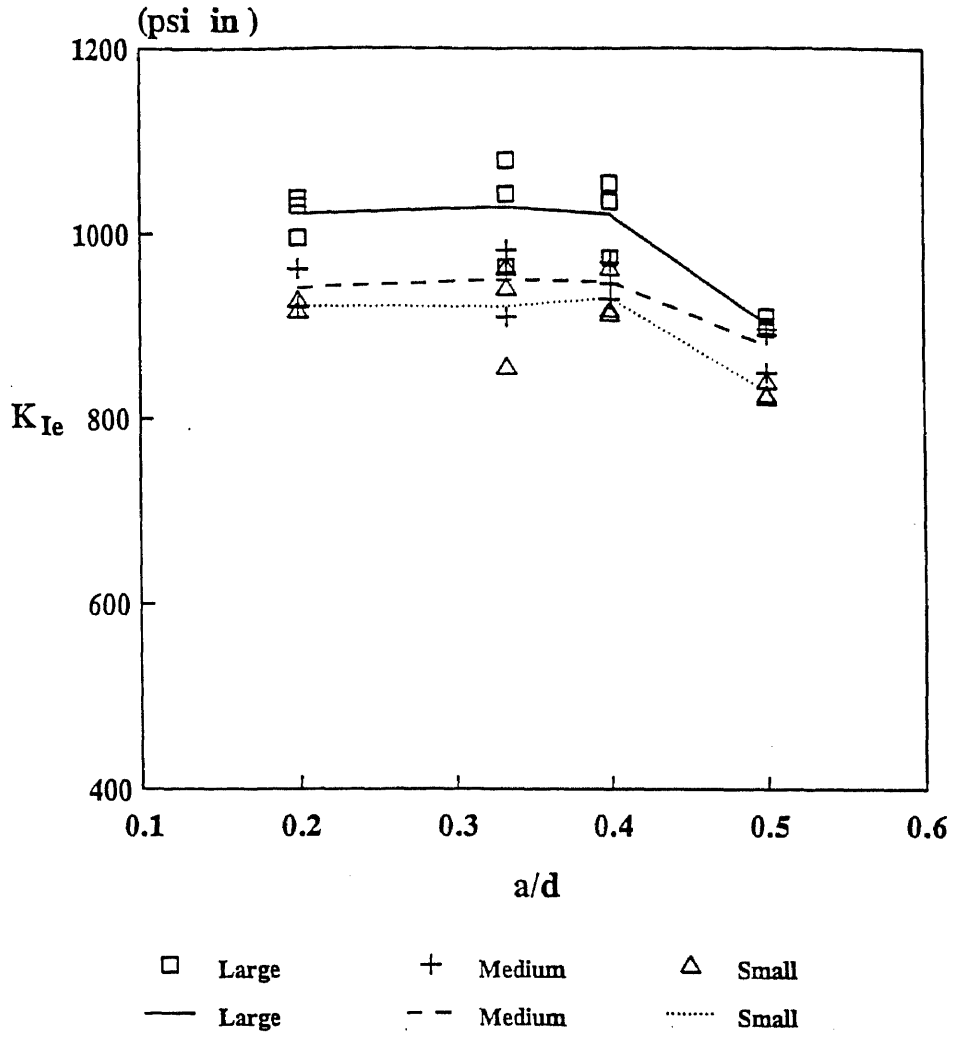

Figure 5.12 Fracture toughness (K_{IC} value) based on LEFM considering the effect of the microcracked process zone

CHAPTER 6

CONCLUSIONS

Based on the results obtained through this study the following conclusions can be drawn:

1. Traditional methods of measuring load-line deflections in beams, which is commonly measured with respect to the base of the testing machine, contain extraneous measurements that are of the same order of magnitude as the actual deflection of the beam. These extraneous measurements are mostly the result of support crushing., which can be eliminated by measuring the beam deflections with reference to its neutral axis using a reference frame attached to the beam. In this study, a new test setup for measuring the load-line deflection in a notched beam test is proposed.

2. When proper measurements of a beam's deflection are made, a bilinear relationship between the *CMOD* and the deflection is found to exist. This bilinear relationship serves as the critical tool to relate the *CMOD* to the fracture energy of the notched beam.

3. The presence of steel fibers in cementitious composites generally increases the ductility (nonlinearity) of the composites. In this study the addition of steel fibers tends to increase the S_2 values without effecting the linear nature of S_2.

4. The deflection-*CMOD* relationships in the pre and post peak regions, S_1 and S_2 respectively, are material properties.

5. To avoid using the complicated testing setup required for properly measuring the load-line deflection of beams, the *CMOD*, which is unaffected by support crushing or other extraneous measurements, is a more reliable parameter for predicting the fracture properties of cementitious composites. Use of the load-*CMOD* relationship along with the proposed S_1 and S_2 relationships could lead to a new testing standard for measuring fracture toughness and fracture energy of cementitious composites.

6. Analysis of Pe/Pmax for various notch depths indicates the progression of the process zone into the region of effective confinement caused by the compression zone of the beam. This inability of the process zone to fully develop explains the so-called "size effect" often noted by the variation of the fracture energy in the testing of notched beams. The analysis further indicates the need to change the current RILEM recommended *a/d* of 0.5 to a value of 0.4 to avoid this effect and improve measurement of fracture energy.

APPENDIX A

DERIVATION OF THE RATIO OF ELASTIC LIMIT LOAD TO PEAK LOAD (P_e/P_{max})

Derivation of the Ratio of Elastic Limit Load to Peak Load (P_e/P_{max})

Crack mouth opening displacement (*CMOD*) is

$$CMOD = \frac{6Psa}{Ebd^2} V_1(A) = \frac{6Ps}{Ebd} AV_1(A)$$

where

$$V_1(A) = 0.76 - 2.28A + 3.87A^2 - 2.04A^3 + \frac{0.66}{(1-A)^2}$$

$$A = \frac{a}{d}$$

Differentiate *CMOD* with respect to a

$$\frac{\partial CMOD}{\partial a} = \frac{\partial CMOD}{\partial A}\frac{\partial A}{\partial a} = \frac{1}{d}\frac{\partial CMOD}{\partial A}$$

Let $C = \frac{6Ps}{Ebd^2} = \frac{6s}{Ebd^2} P$

Substituting C and $V_1(A)$ into equation $\frac{\partial CMOD}{\partial a}$ gives

$$\frac{\partial CMOD}{\partial a} = CV_1(A) + CA\left(-2.28 + 7.74A - 6.12A^2 + \frac{1.32}{(1-A)^3}\right)$$

$$= K_2 \frac{6s}{Ebd^2} P$$

where

$$K_2 = V_1(A) + A\left(-2.28 + 7.74A - 6.12A^2 + \frac{1.32}{(1-A)^3}\right)$$

Differentiate *CMOD* with respect to P

$$\frac{\partial CMOD}{\partial P} = \frac{6s}{Ebd} AV_1(A)$$

Load point displacement δ_P is

$$\delta_P = \frac{3Ps^2}{2Ebd^2} V_2(A) + \frac{Ps^3}{4Ebd^3} + \frac{3.6Ps}{5Ebd}$$

where

$$V_2(A) = \left(\frac{A}{1-A}\right)^2 (5.58 - 19.57A + 36.82A^2 - 34.94A^3 + 12.77A^4)$$

Differentiate δ_P with respect to a

$$\frac{\partial \delta_P}{\partial a} = \frac{3Ps^2}{2Ebd^3} K_1 = K_1 \frac{3s^2}{2Ebd^3} P$$

where

$$K_1 = \left[2\frac{A}{(1-A)^3}(5.58 - 19.57A + 36.82A^2 - 34.94A^3 + 12.77A^4) + \left(\frac{A}{1-A}\right)^2 (-19.57 + 73.64A - 104.82A^2 + 51.08A^3) \right]$$

Differentiate δ_P with respect to P

$$\frac{\partial \delta_P}{\partial P} = \frac{3s^2}{2Ebd^2} V_2(A) + \frac{s^3}{4Ebd^3} + \frac{3.6s}{5Ebd}$$

The change of slope, ΔS, due to increment of ΔP is

$$\Delta S = \frac{\Delta \delta_P}{\Delta CMOD} = \frac{\frac{\partial \delta_P}{\partial a} \Delta a + \frac{\partial \delta_P}{\partial P} \Delta P}{\frac{\partial CMOD}{\partial a} \Delta a + \frac{\partial CMOD}{\partial P} \Delta P}$$

Rearranging the above equation gives

$$\left(\frac{\partial CMOD}{\partial a} \Delta a + \frac{\partial CMOD}{\partial P} \Delta P\right) \Delta S = \frac{\partial \delta_P}{\partial a} \Delta a + \frac{\partial \delta_P}{\partial P} \Delta P$$

$$\left(\frac{\partial CMOD}{\partial P} \Delta S - \frac{\partial \delta_P}{\partial P}\right) \Delta P = \left(\frac{\partial \delta_P}{\partial a} - \frac{\partial CMOD}{\partial a} \Delta S\right) \Delta a$$

$$\Delta P = P_{max} - P = \frac{\frac{\partial \delta_P}{\partial a} - \frac{\partial CMOD}{\partial a} \Delta S}{\frac{\partial CMOD}{\partial P} \Delta S - \frac{\partial \delta_P}{\partial P}} \Delta a$$

$$P = P_{\max} - \frac{K_1 \frac{3s^2}{2Ebd^3} - K_2 \frac{6s}{Ebd^2} \Delta S}{\frac{\partial CMOD}{\partial P} \Delta S - \frac{\partial \delta_P}{\partial P}} \Delta a \quad P = P_{\max} - KP$$

where

$$K = \frac{K_1 \frac{3s^2}{2Ebd^3} - K_2 \frac{6s}{Ebd^2} \Delta S}{\frac{\partial CMOD}{\partial P} \Delta S - \frac{\partial \delta_P}{\partial P}} \Delta a$$

Therefore the load at the starting point of microcracked process zone can be expressed as follows.

$$P = \frac{P_{\max}}{1 + K}$$

APPENDIX B

TESTING RESULTS

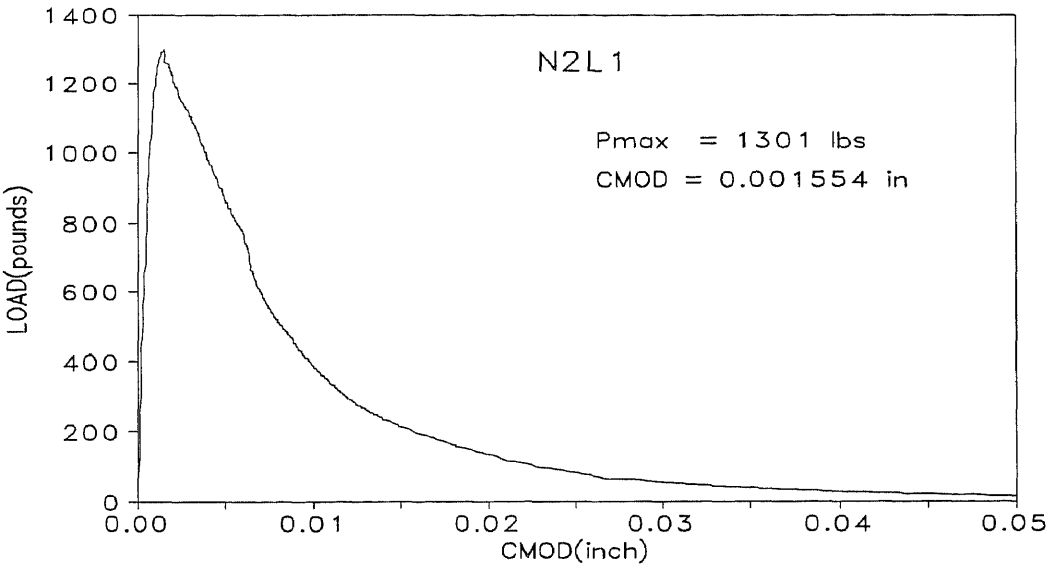

Figure A 1a Load-*CMOD* relationship (N2L1)

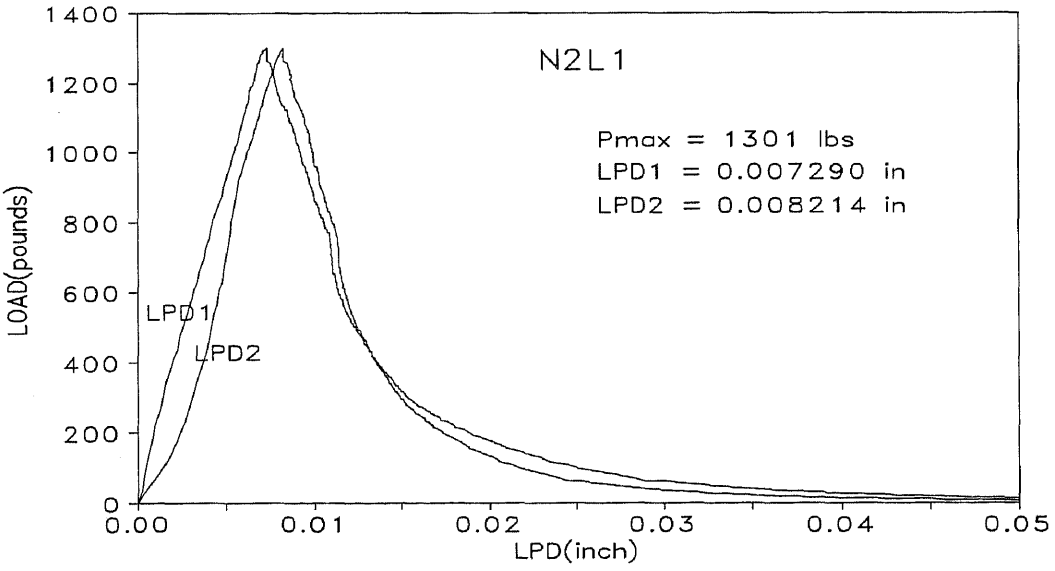

Figure A 1b Load-deflection relationship (N2L1)

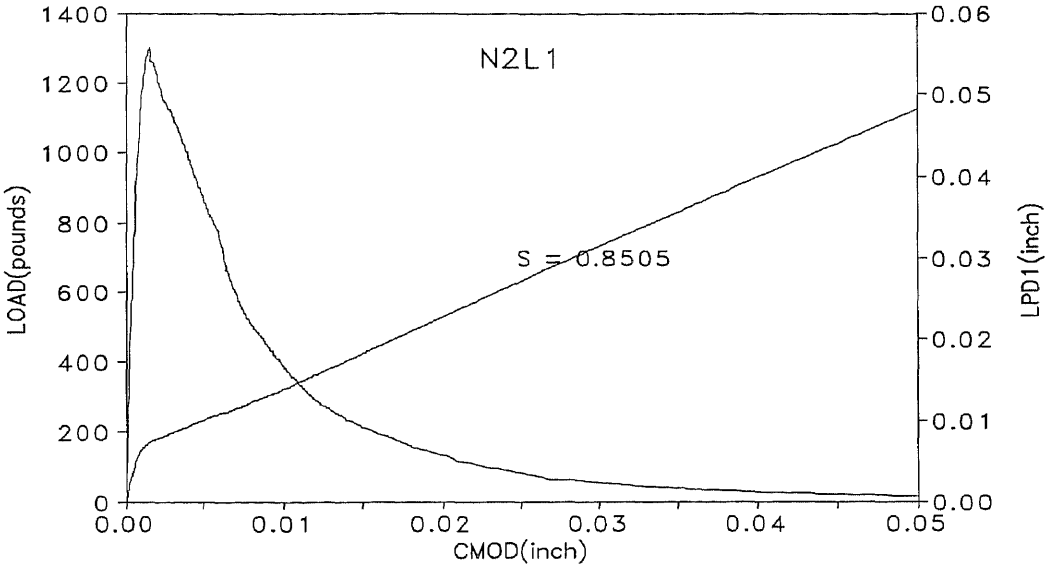

Figure A 1c Load-*CMOD*-deflection (LVDT1) relationship (N2L1)

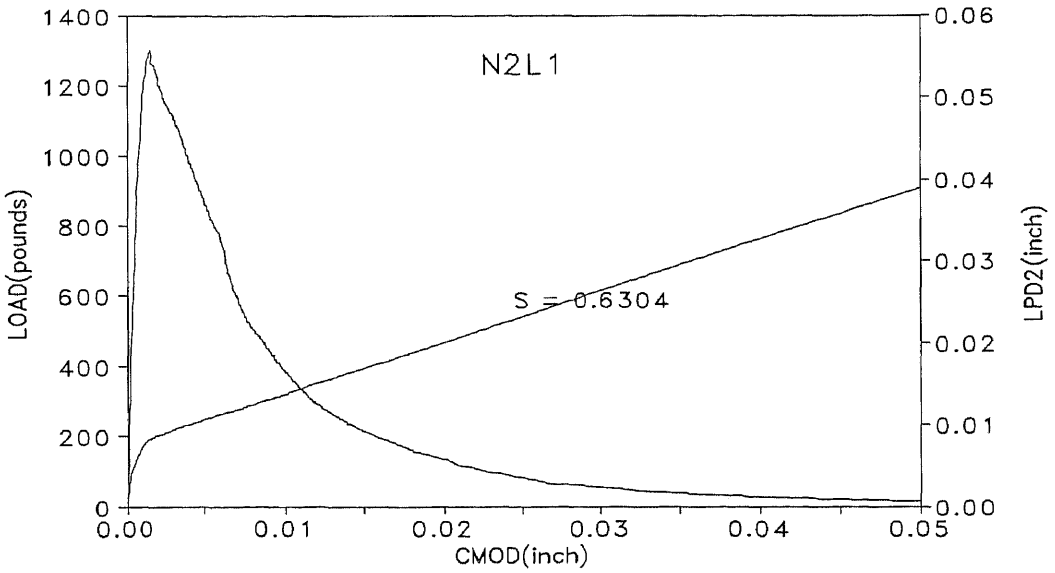

Figure A 1d Load-*CMOD*-deflection (LVDT2) relationship (N2L1)

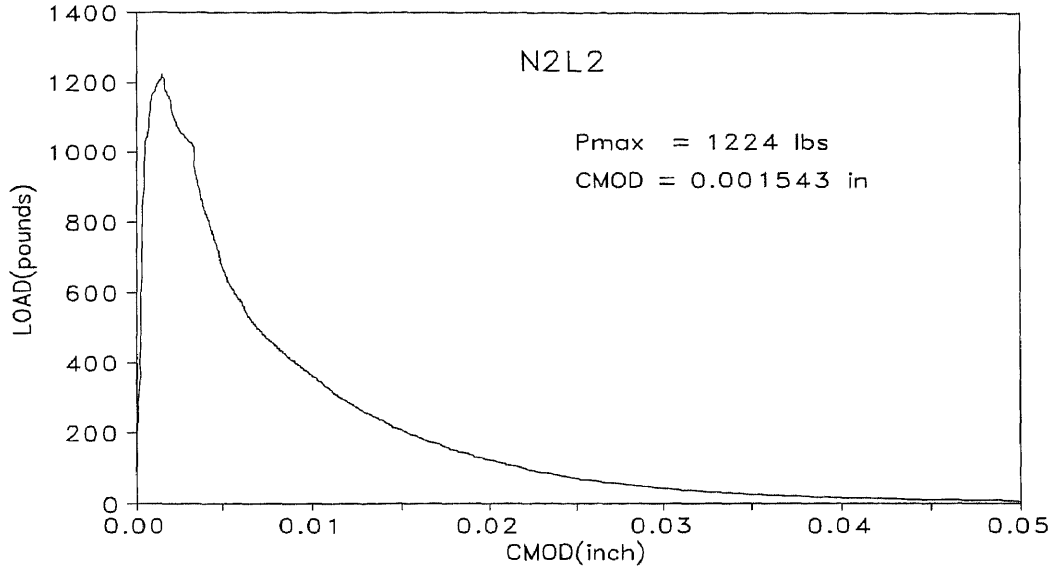

Figure A 2a Load-*CMOD* relationship (N2L2)

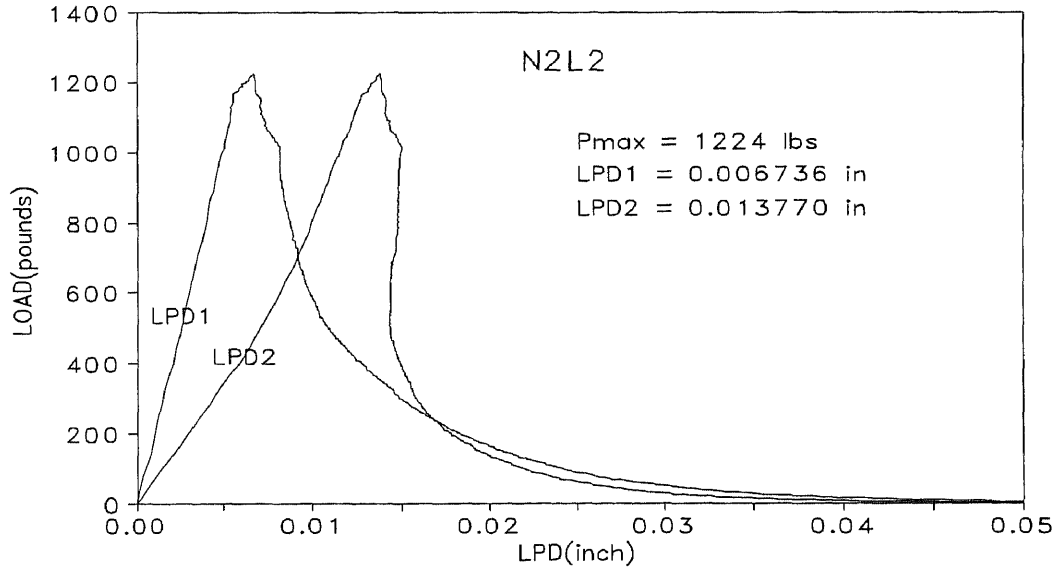

Figure A 2b Load-deflection relationship (N2L2)

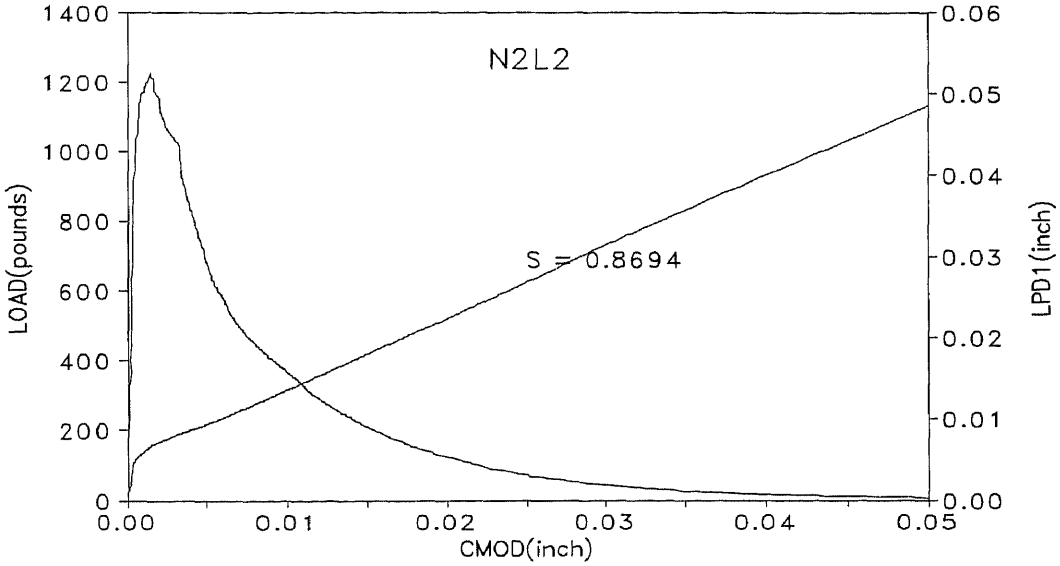

Figure A 2c Load-*CMOD*-deflection (LVDT1) relationship (N2L2)

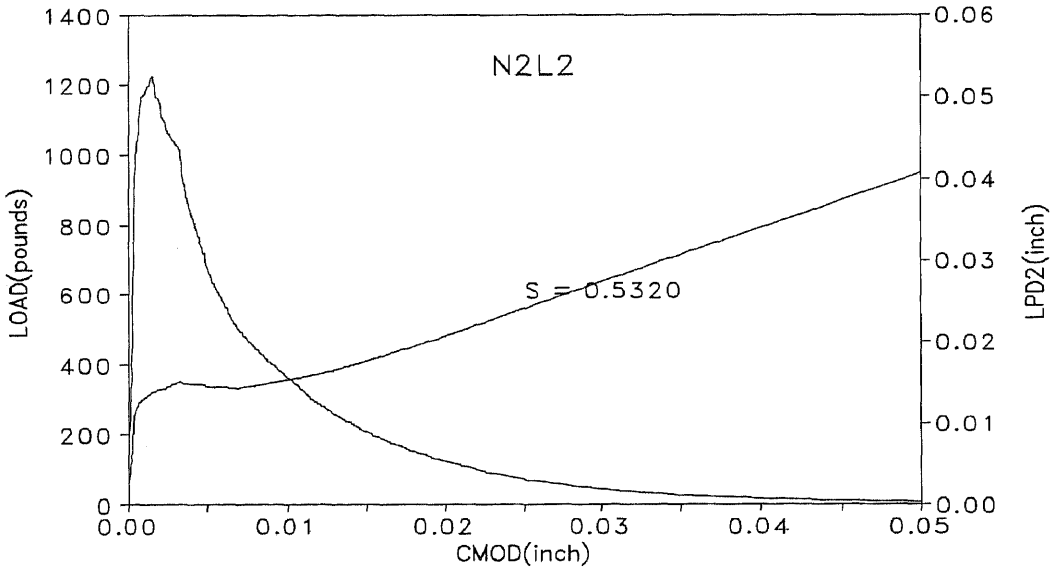

Figure A 2d Load-*CMOD*-deflection (LVDT2) relationship (N2L2)

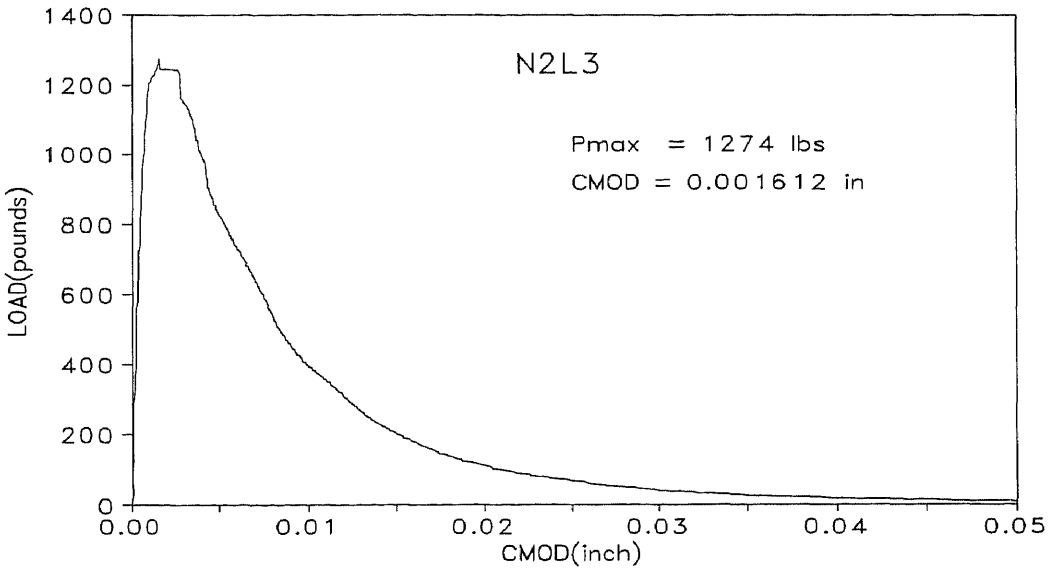

Figure A 3a Load-*CMOD* relationship (N2L3)

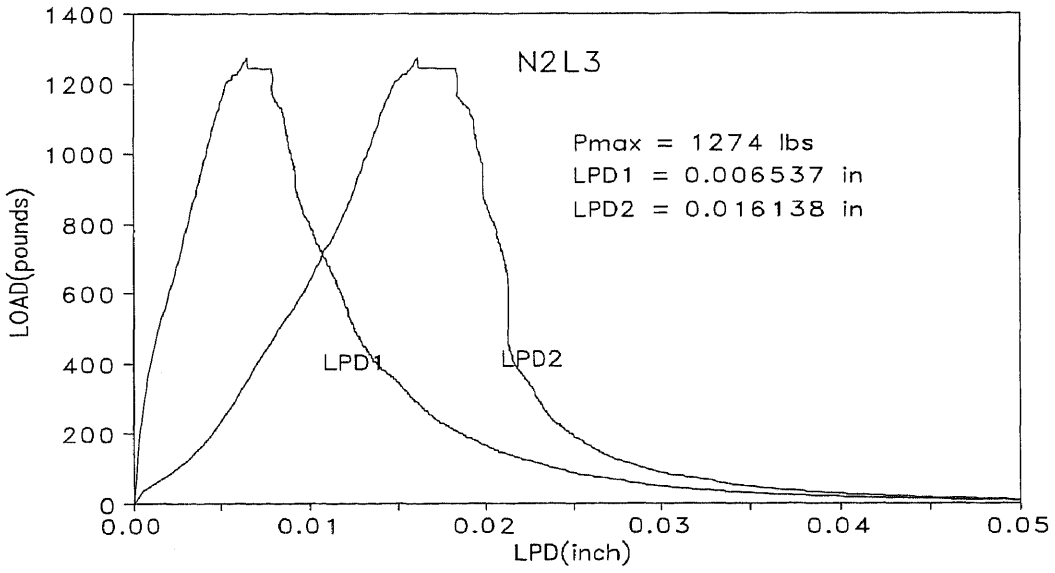

Figure A 3b Load-deflection relationship (N2L3)

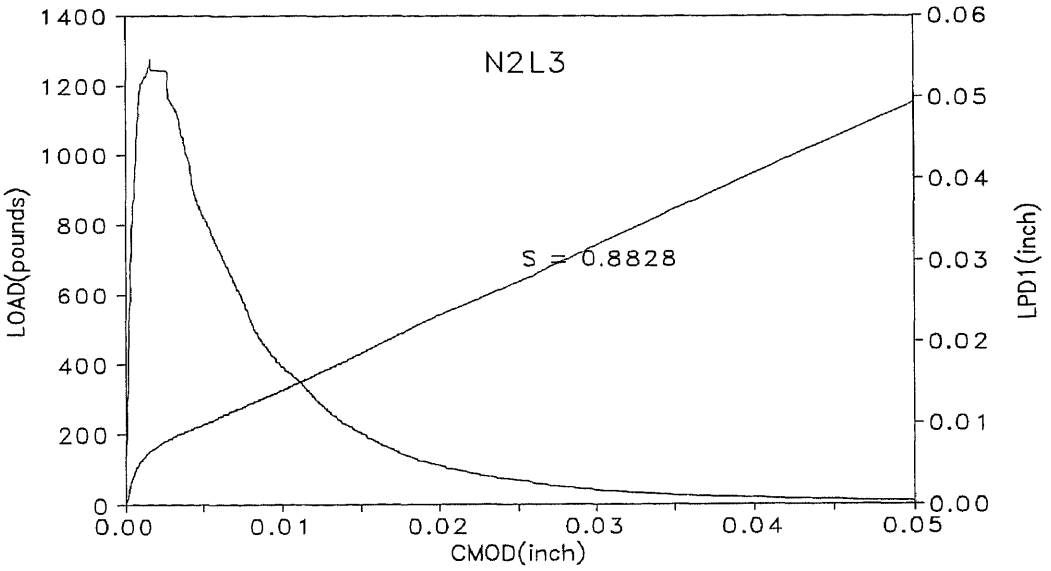

Figure A 3c Load-*CMOD*-deflection (LVDT1) relationship (N2L3)

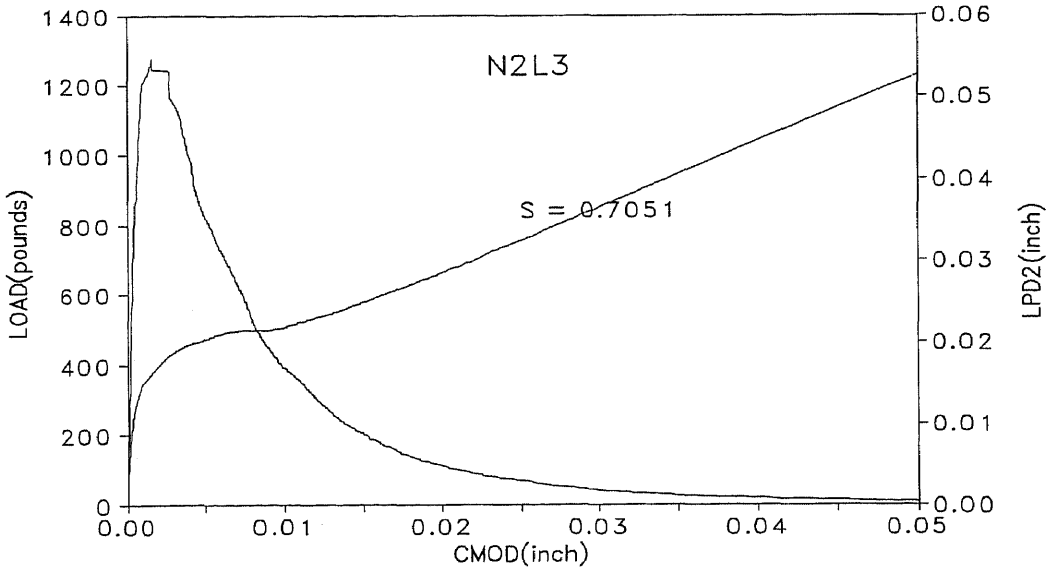

Figure A 3d Load-*CMOD*-deflection (LVDT2) relationship (N2L3)

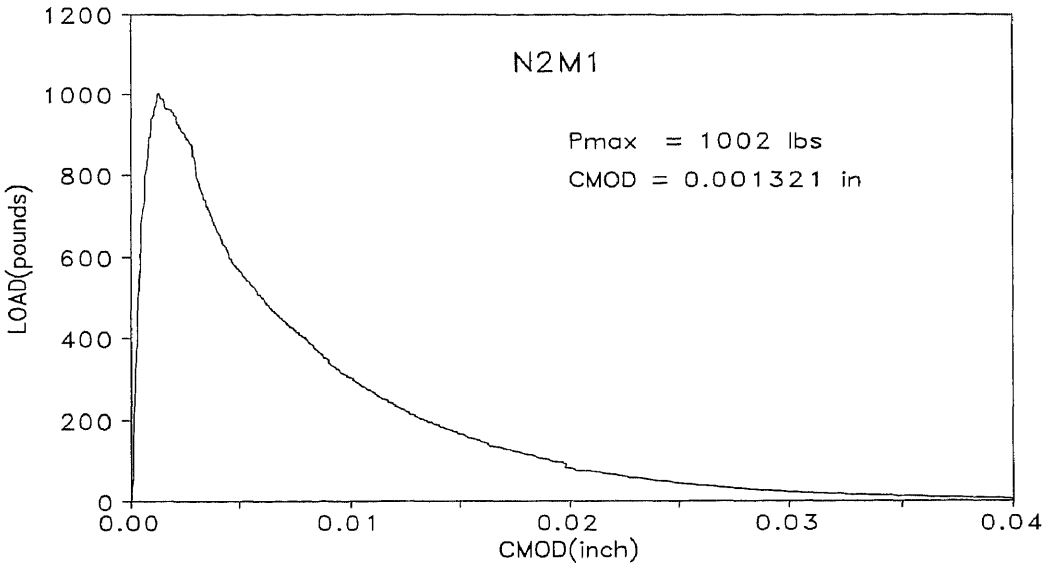

Figure A 4a Load-*CMOD* relationship (N2M1)

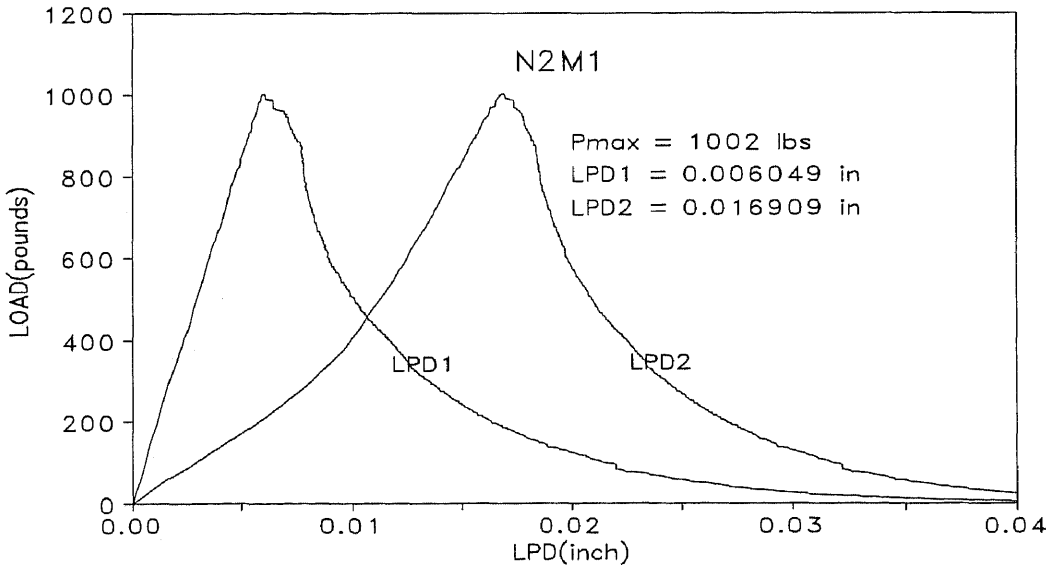

Figure A 4b Load-deflection relationship (N2M1)

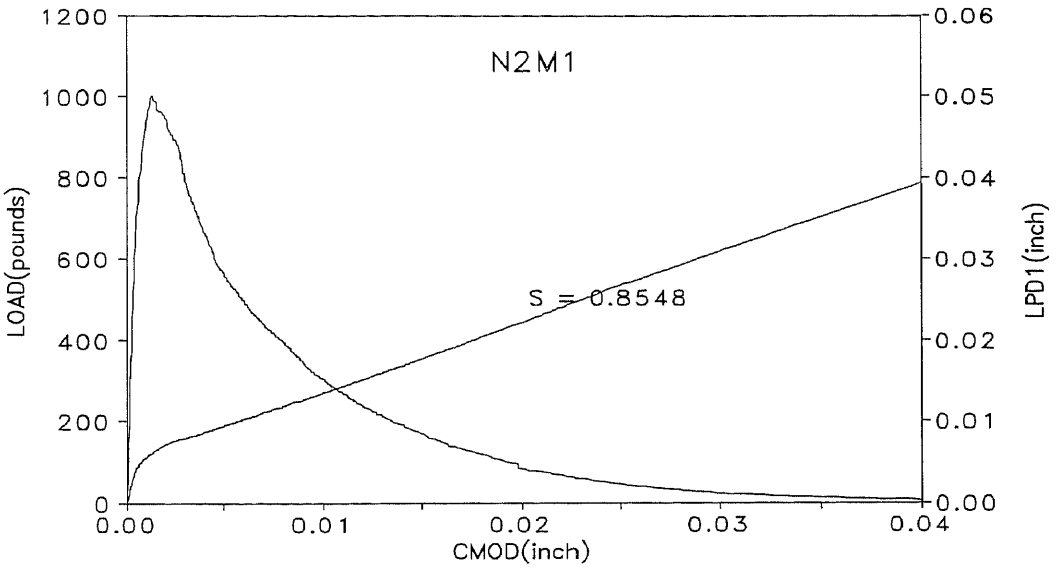

Figure A 4c Load-*CMOD*-deflection (LVDT1) relationship (N2M1)

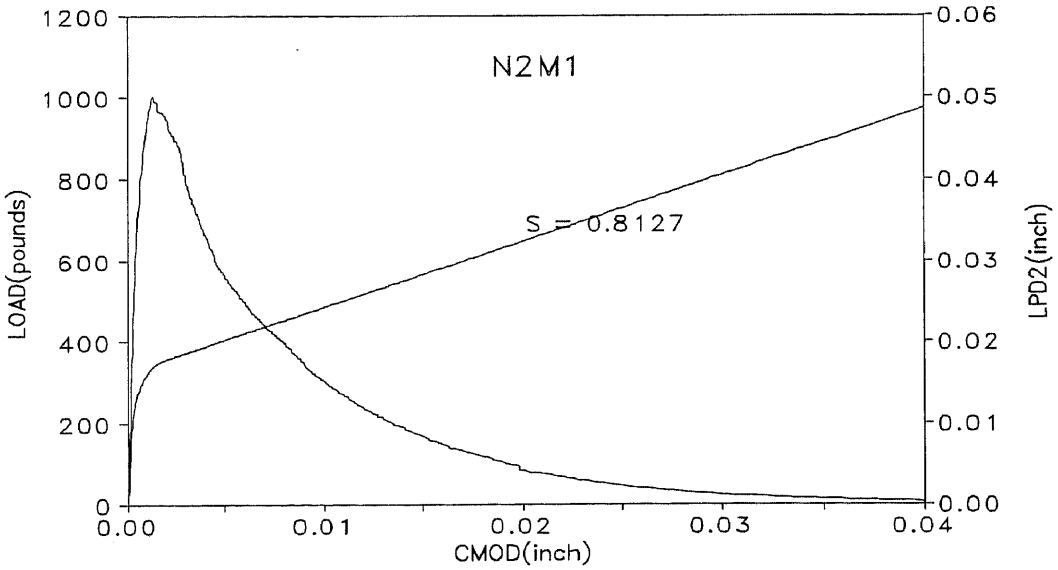

Figure A 4d Load-*CMOD*-deflection (LVDT2) relationship (N2M1)

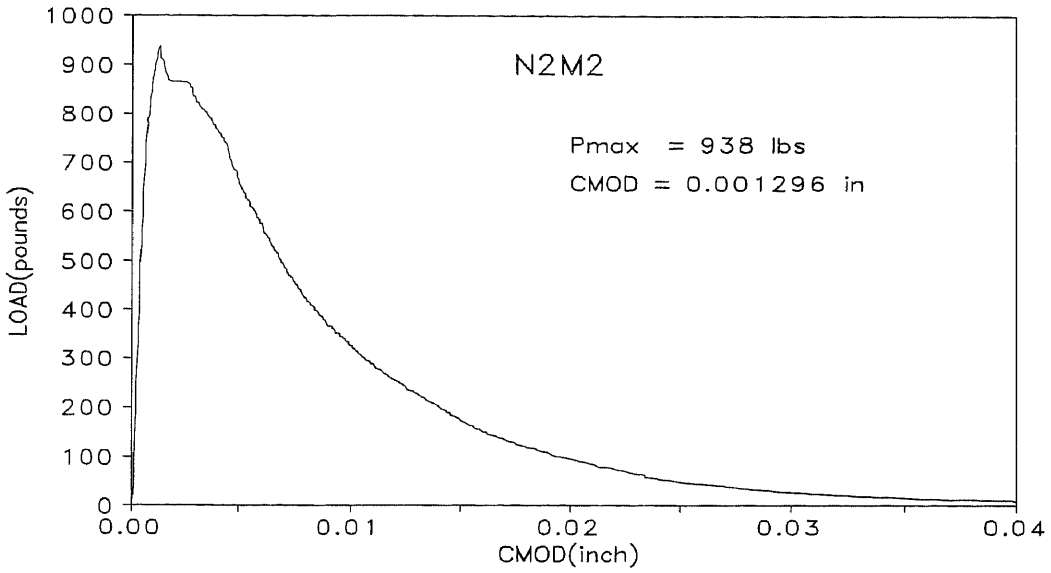

Figure A 5a Load-*CMOD* relationship (N2M2)

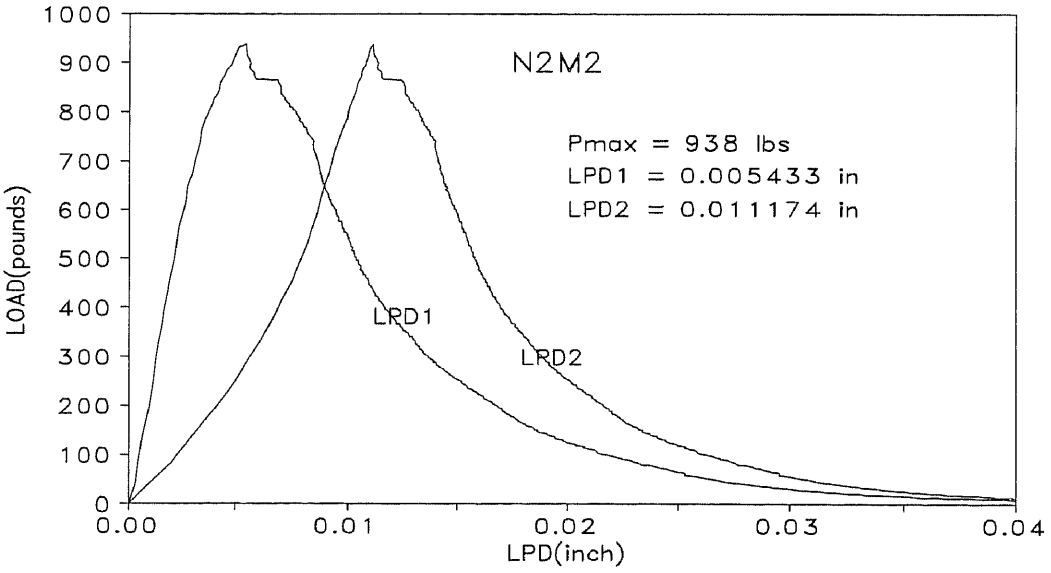

Figure A 5b Load-deflection relationship (N2M2)

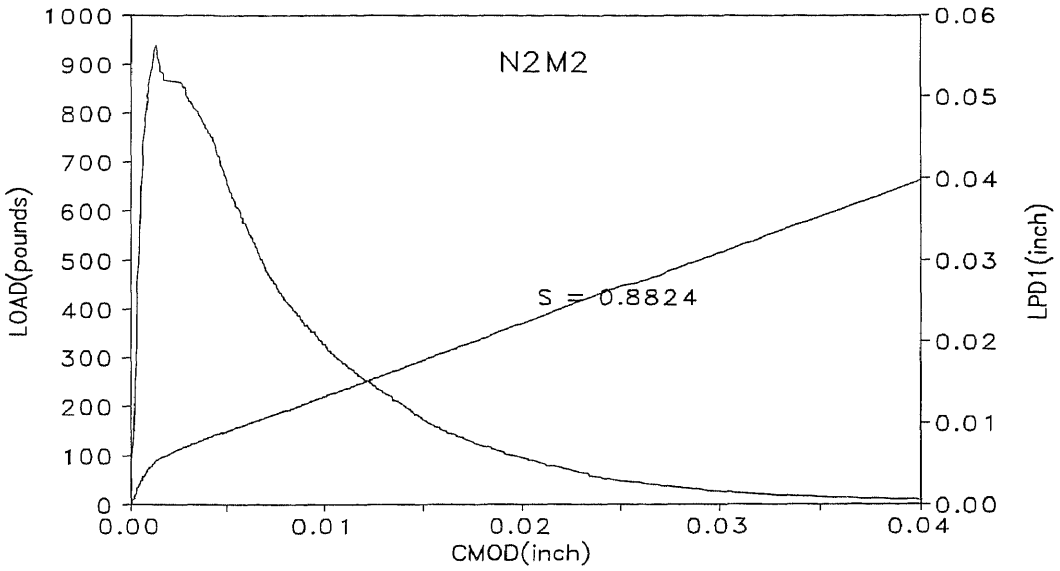

Figure A 5c Load-*CMOD*-deflection (LVDT1) relationship (N2M2)

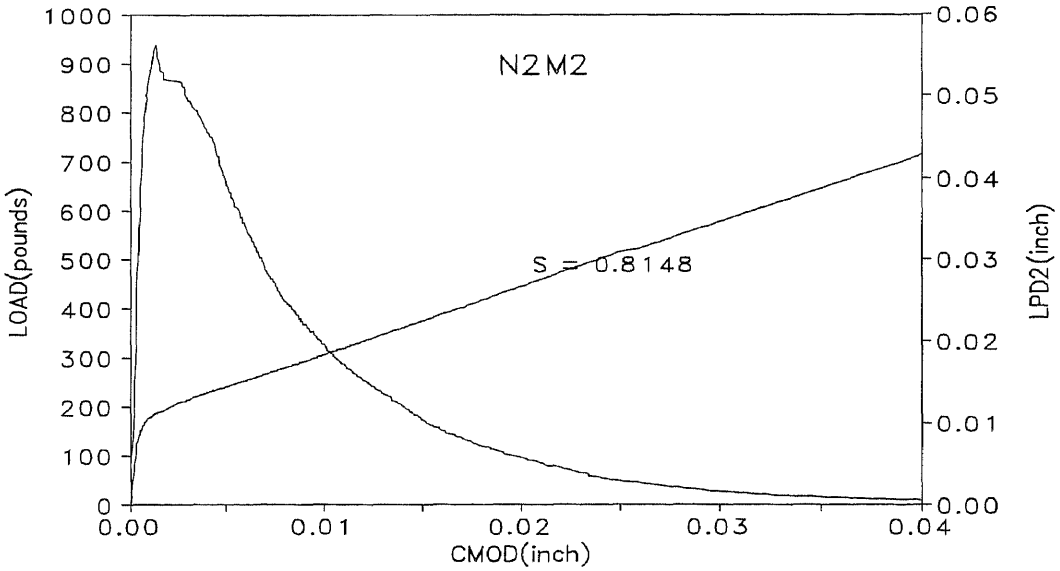

Figure A 5d Load-*CMOD*-deflection (LVDT2) relationship (N2M2)

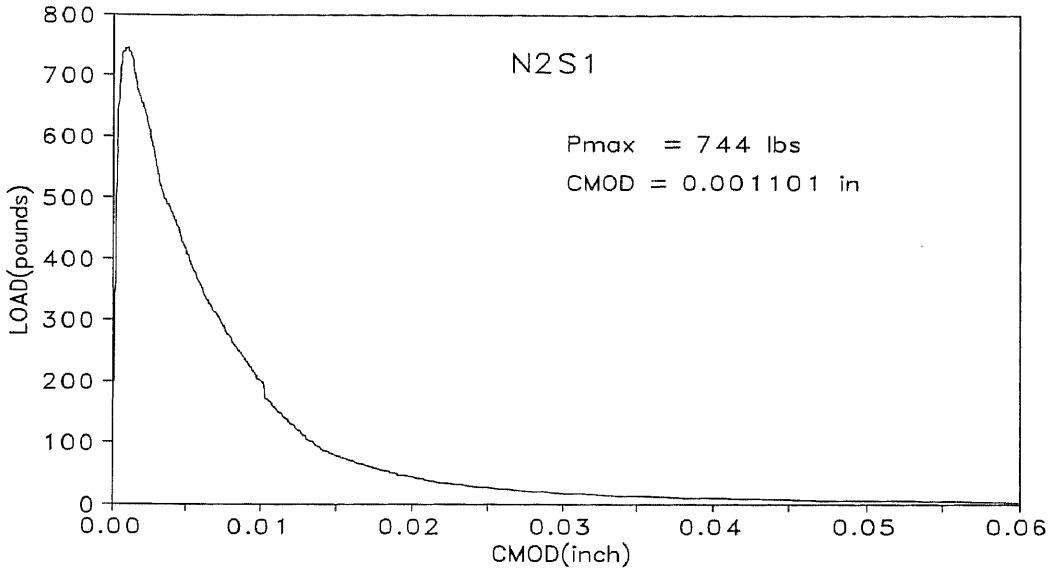

Figure A 6a Load-*CMOD* relationship (N2S1)

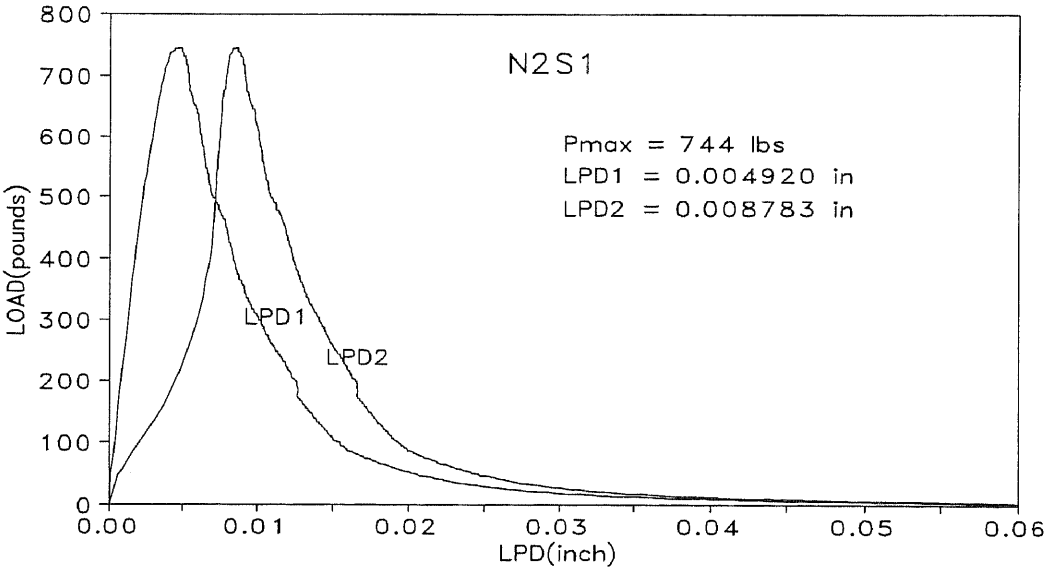

Figure A 6b Load-deflection relationship (N2S1)

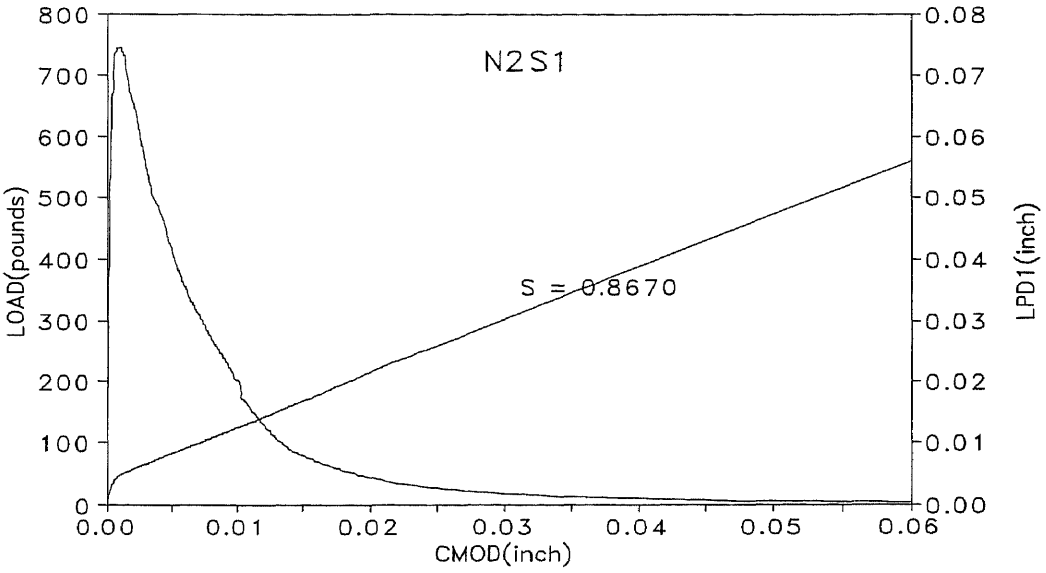

Figure A 6c Load-*CMOD*-deflection (LVDT1) relationship (N2S1)

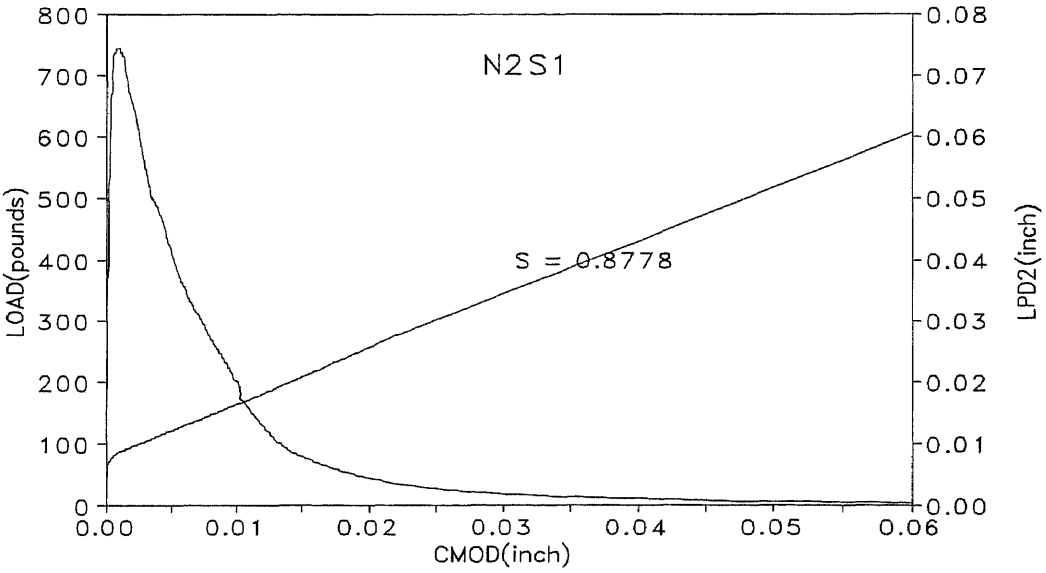

Figure A 6d Load-*CMOD*-deflection (LVDT2) relationship (N2S1)

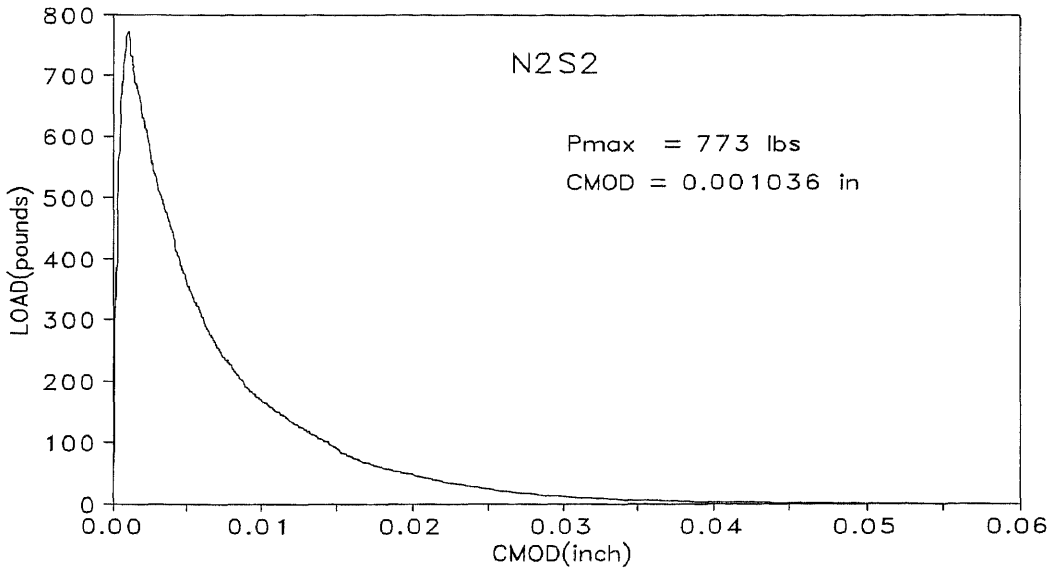

Figure A 7a Load-*CMOD* relationship (N2S2)

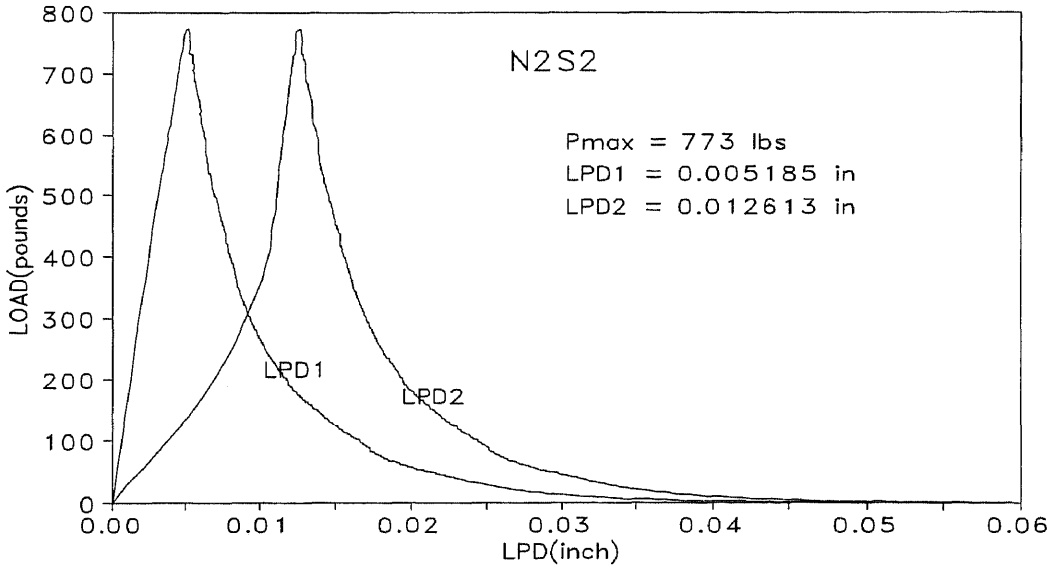

Figure A 7b Load-deflection relationship (N2S2)

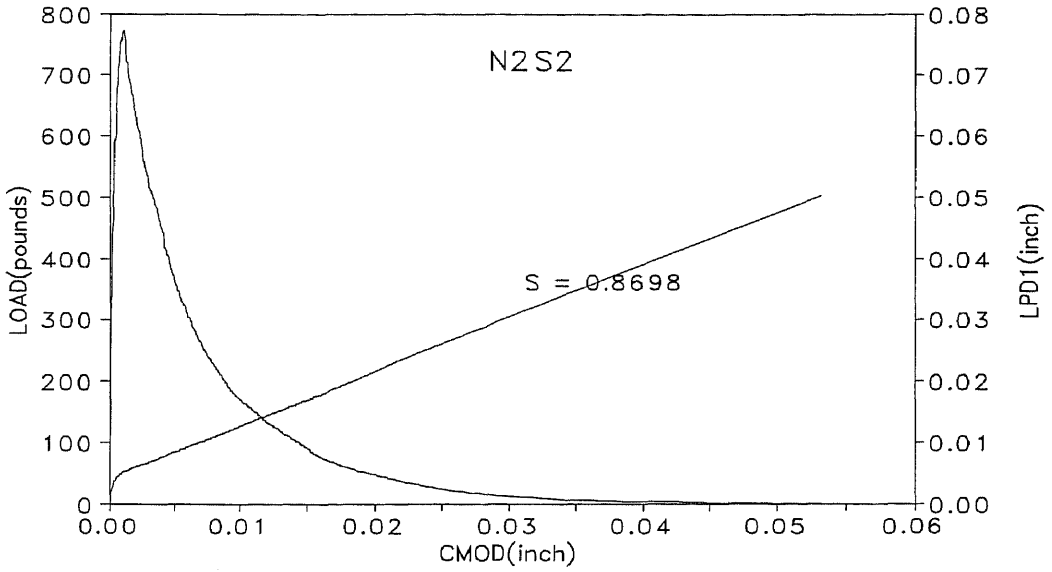

Figure A 7c Load-*CMOD*-deflection (LVDT1) relationship (N2S2)

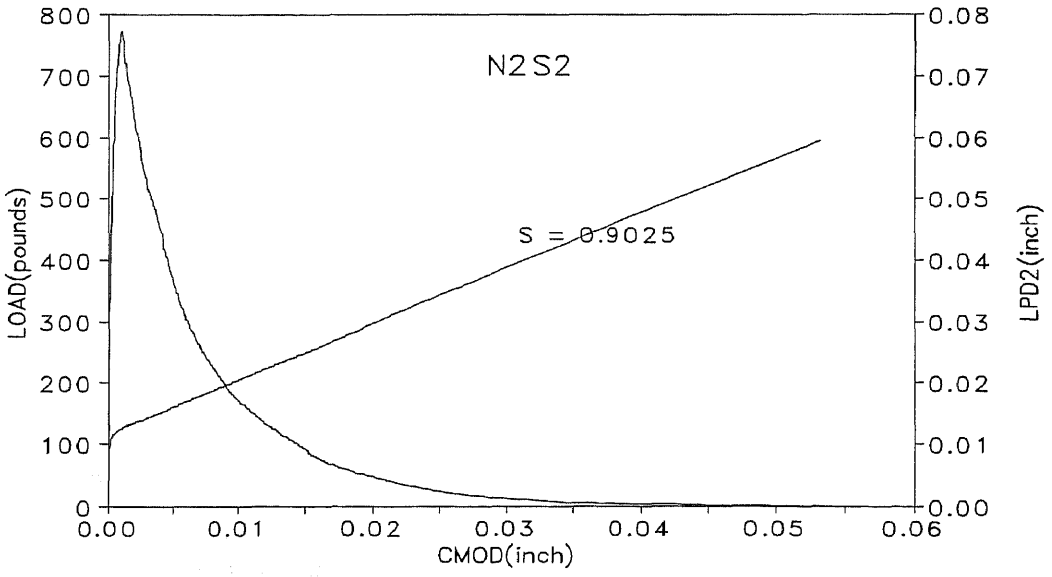

Figure A 7d Load-*CMOD*-deflection (LVDT2) relationship (N2S2)

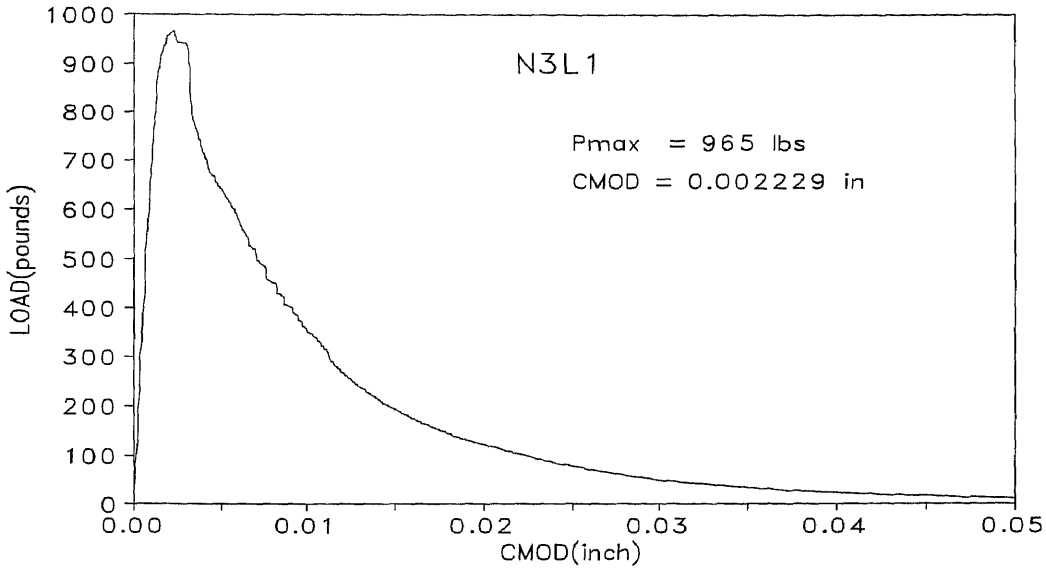

Figure A 8a Load-*CMOD* relationship (N3L1)

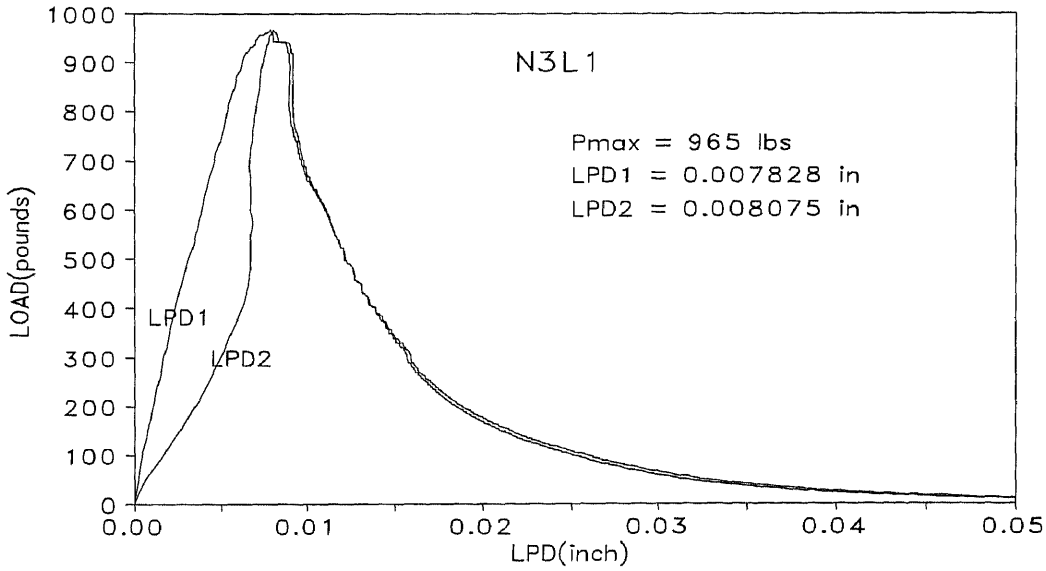

Figure A 8b Load-deflection relationship (N3L1)

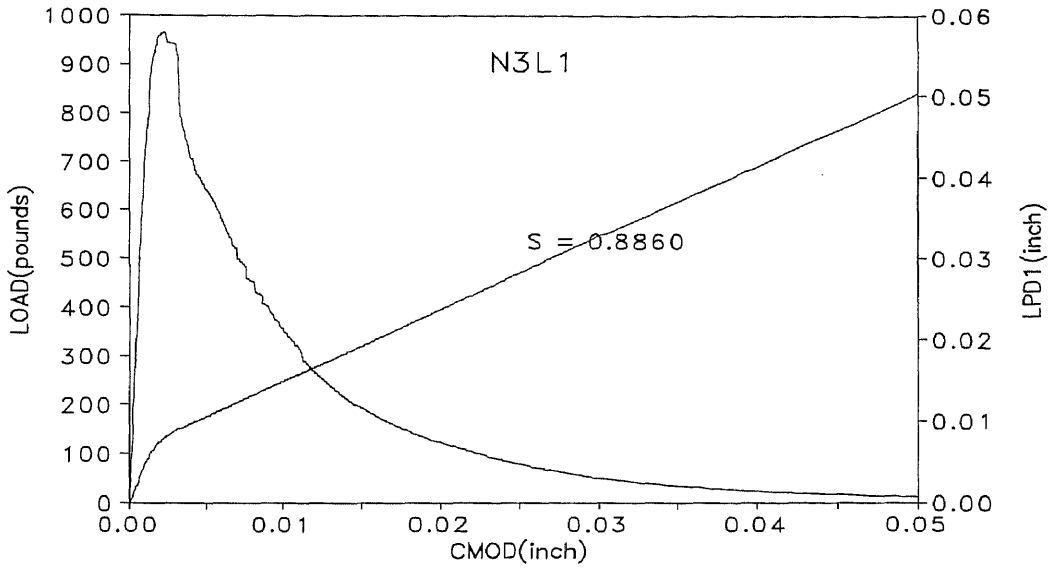

Figure A 8c Load-*CMOD*-deflection (LVDT1) relationship (N3L1)

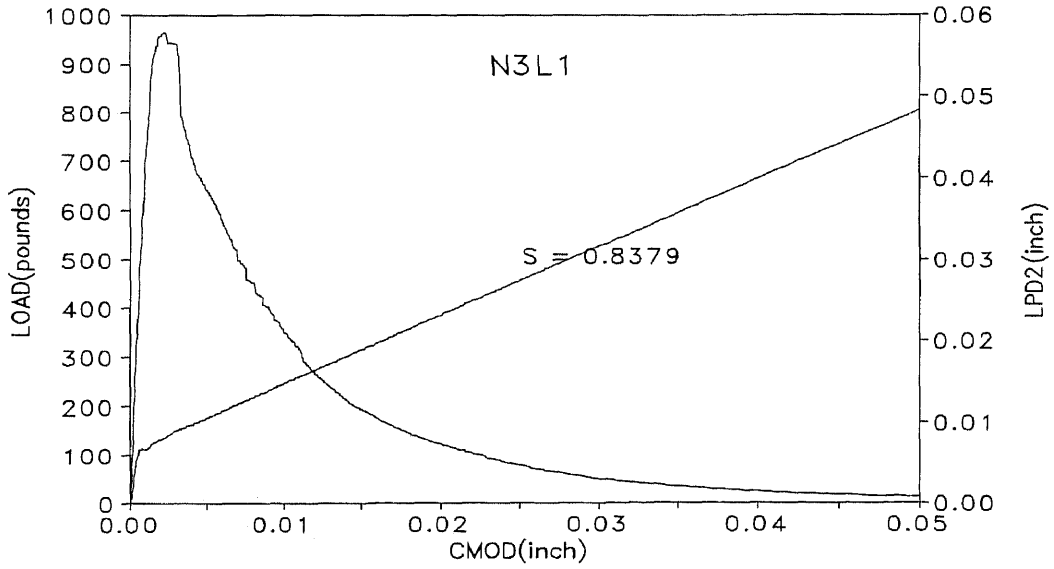

Figure A 8d Load-*CMOD*-deflection (LVDT2) relationship (N3L1)

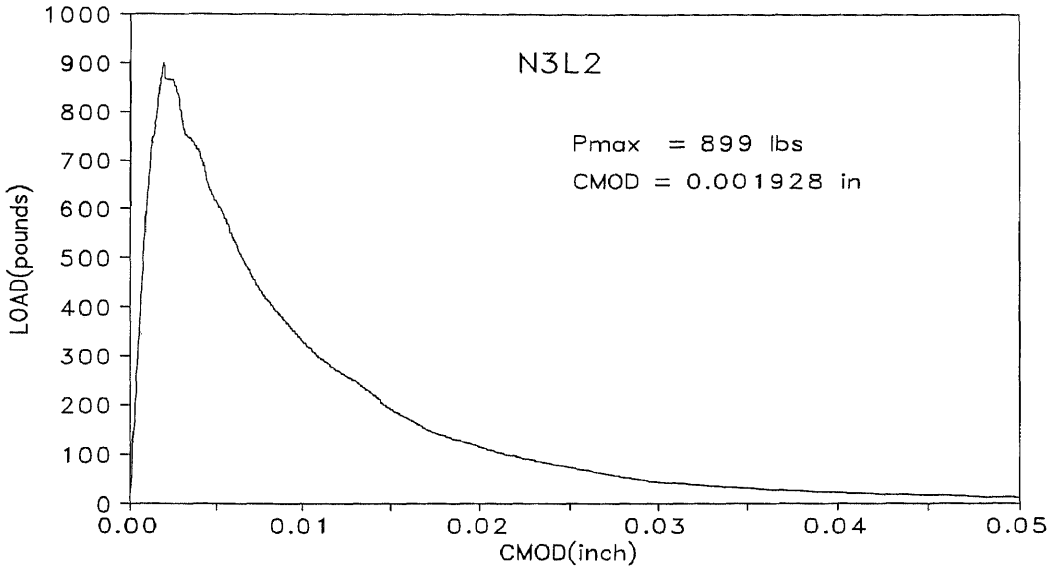

Figure A 9a Load-*CMOD* relationship (N3L2)

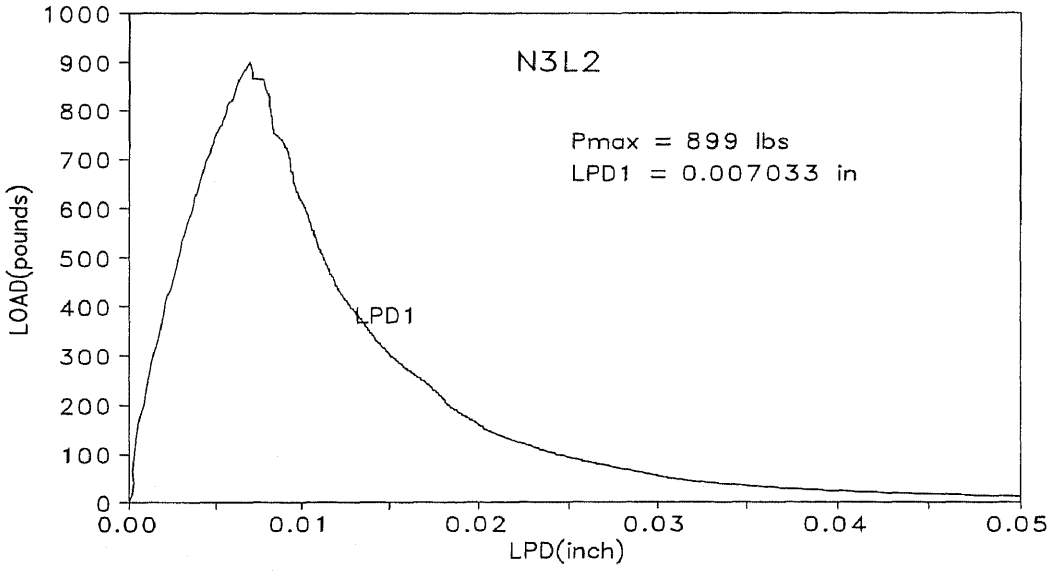

Figure A 9b Load-deflection relationship (N3L2)

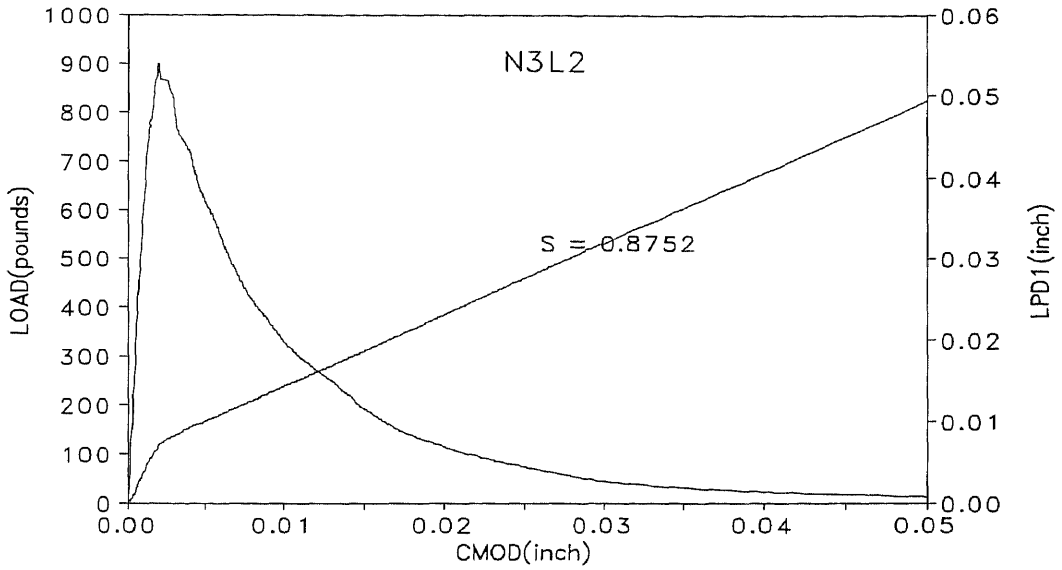

Figure A 9c Load-*CMOD*-deflection (LVDT1) relationship (N3L2)

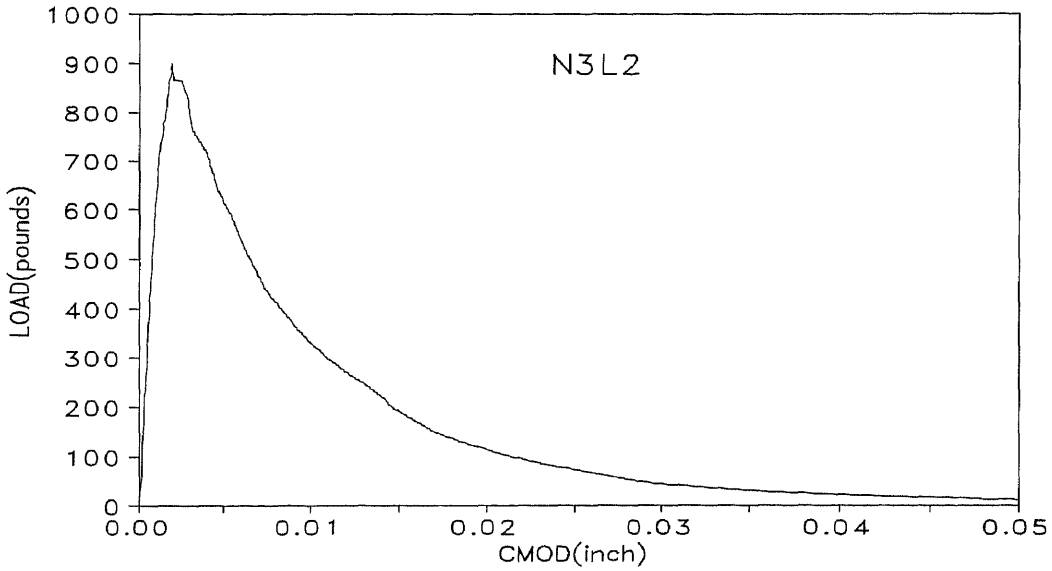

Figure A 9d Load-*CMOD*-deflection (LVDT2) relationship (N3L2)

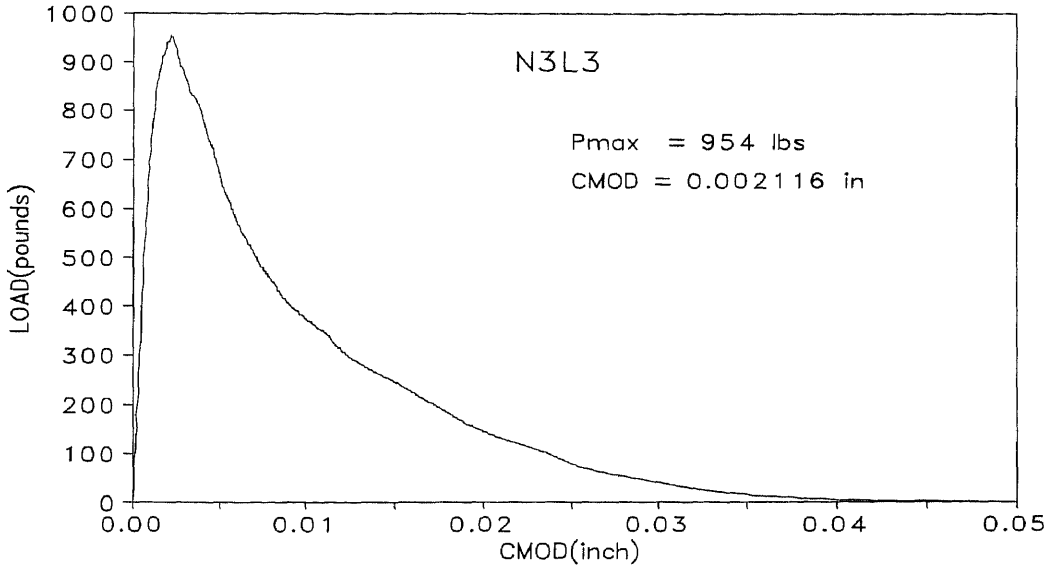

Figure A 10a Load-*CMOD* relationship (N3L3)

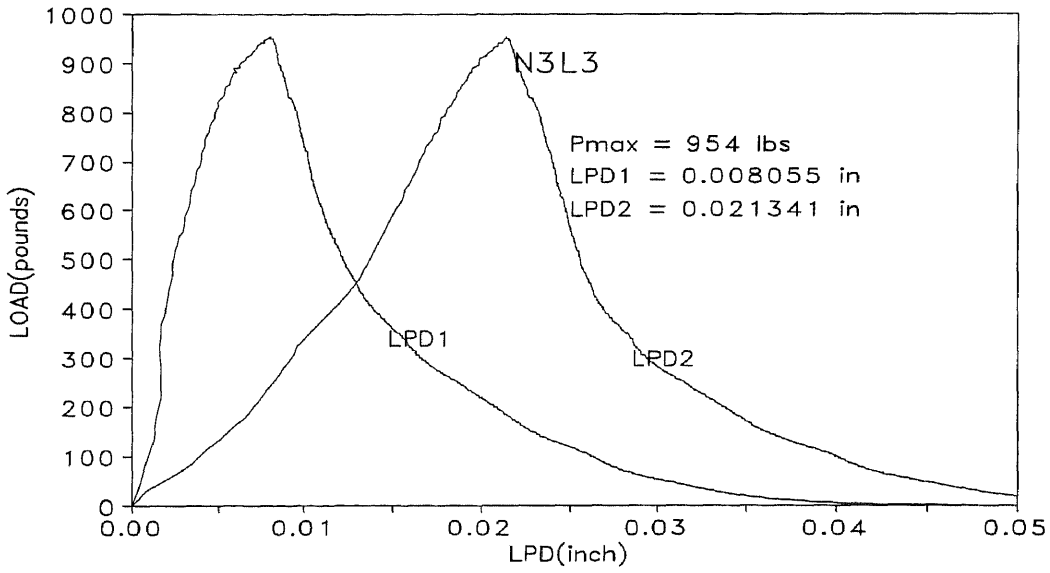

Figure A 10b Load-deflection relationship (N3L3)

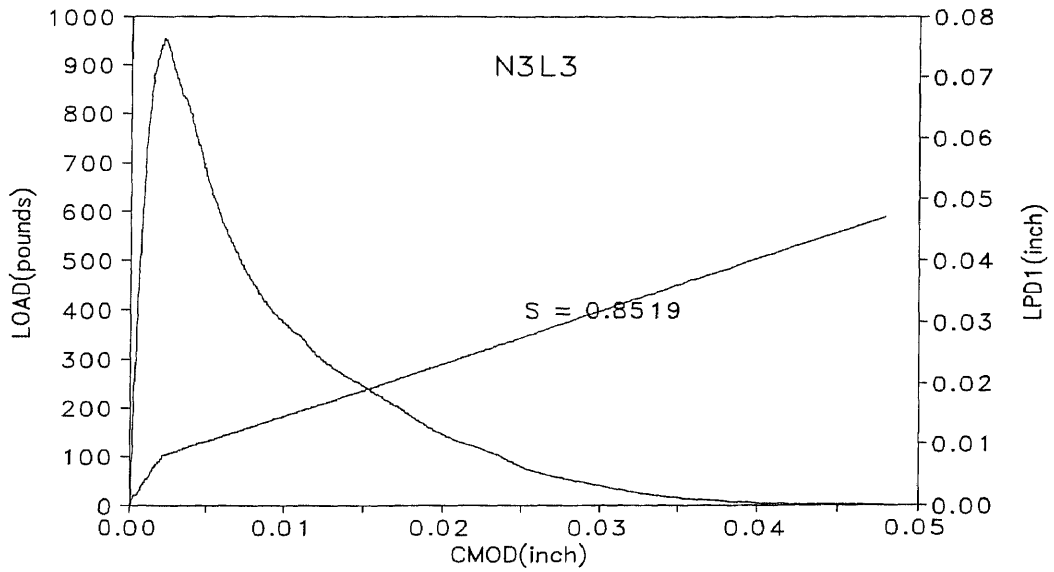

Figure A 10c Load-*CMOD*-deflection (LVDT1) relationship (N3L3)

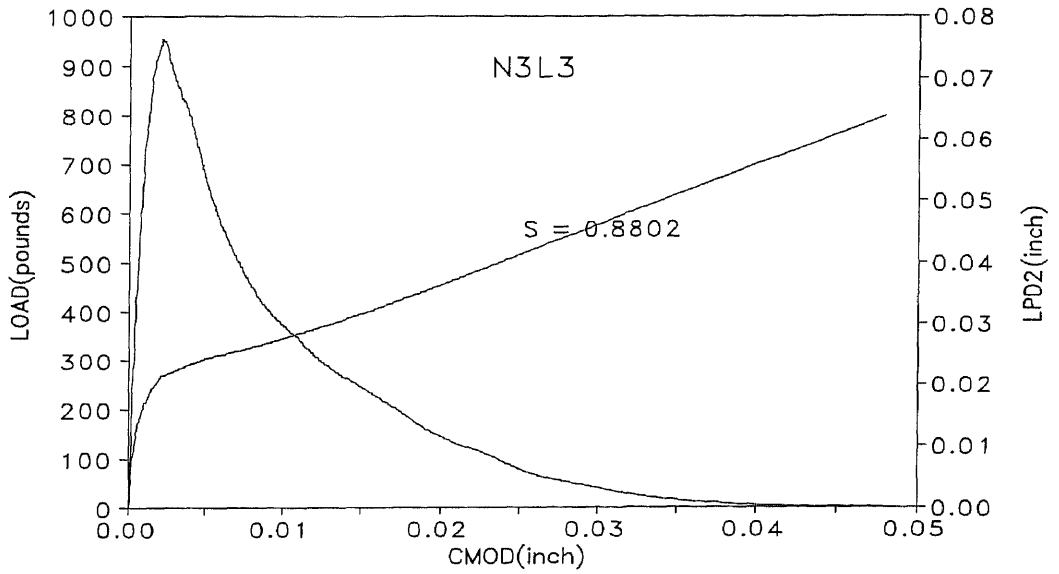

Figure A 10d Load-*CMOD*-deflection (LVDT2) relationship (N3L3)

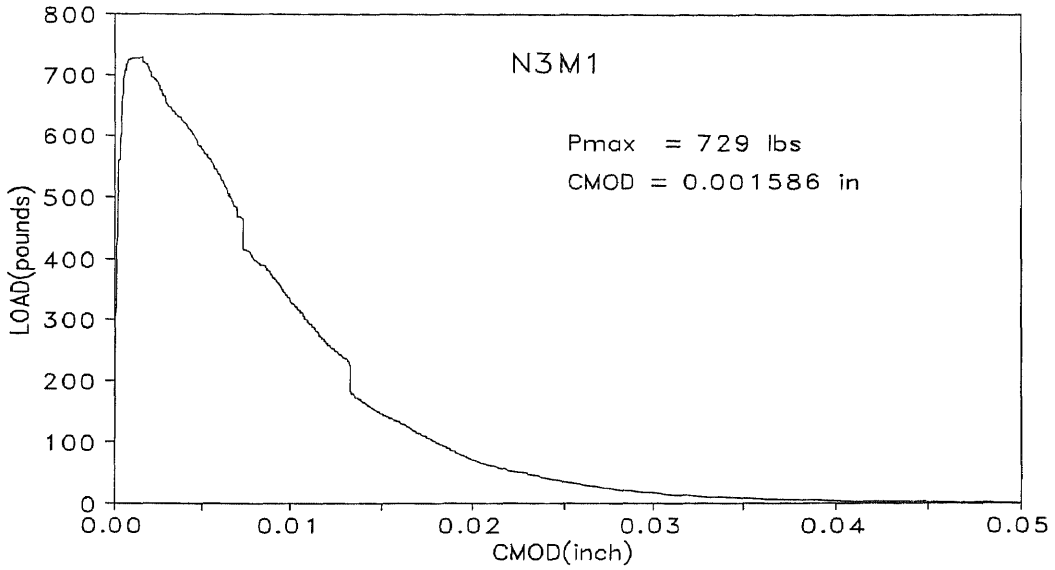

Figure A 11a Load-*CMOD* relationship (N3M1)

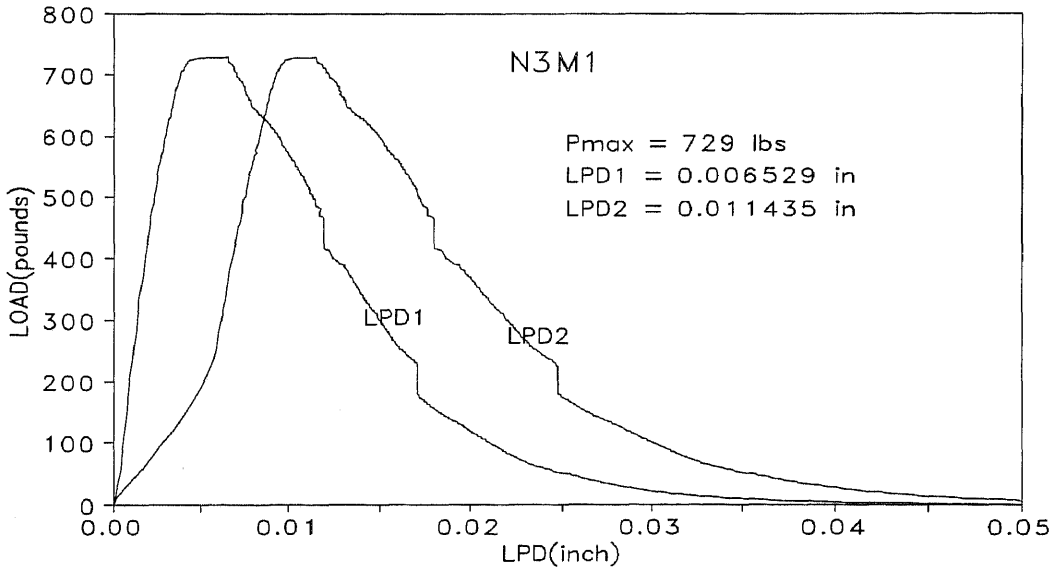

Figure A 11b Load-deflection relationship (N3M1)

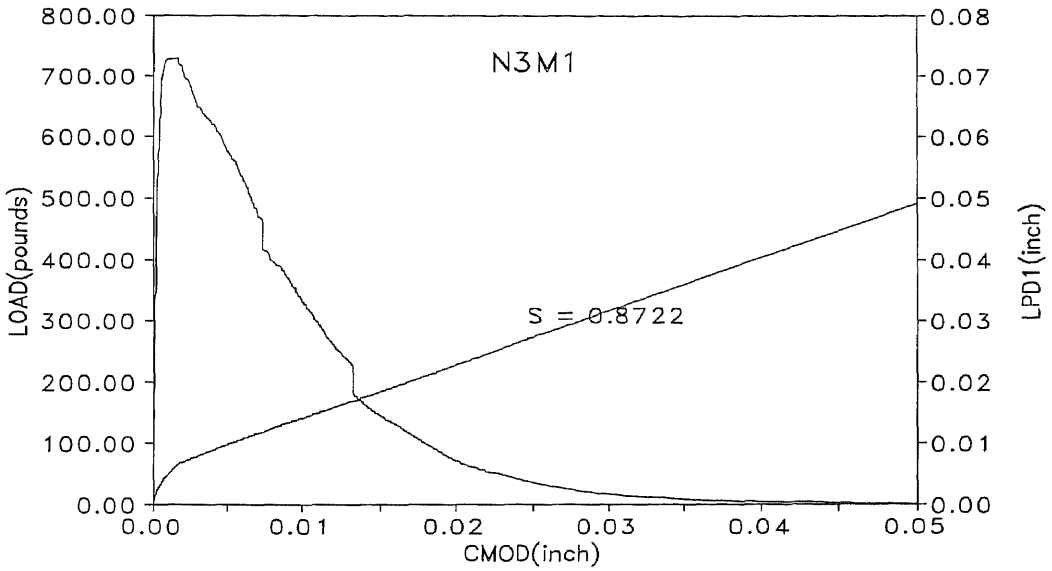

Figure A 11c Load-*CMOD*-deflection (LVDT1) relationship (N3M1)

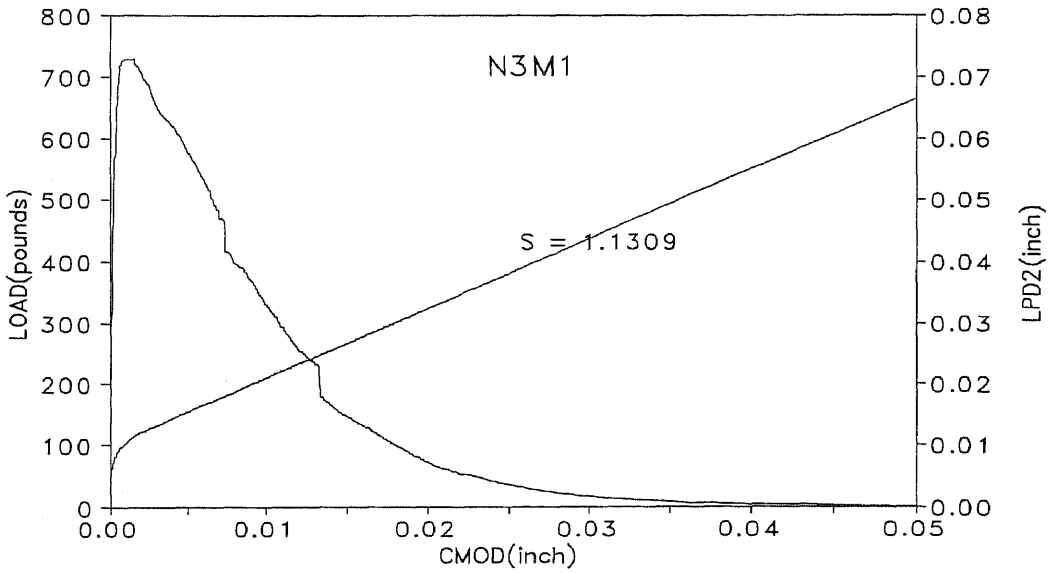

Figure A 11d Load-*CMOD*-deflection (LVDT2) relationship (N3M1)

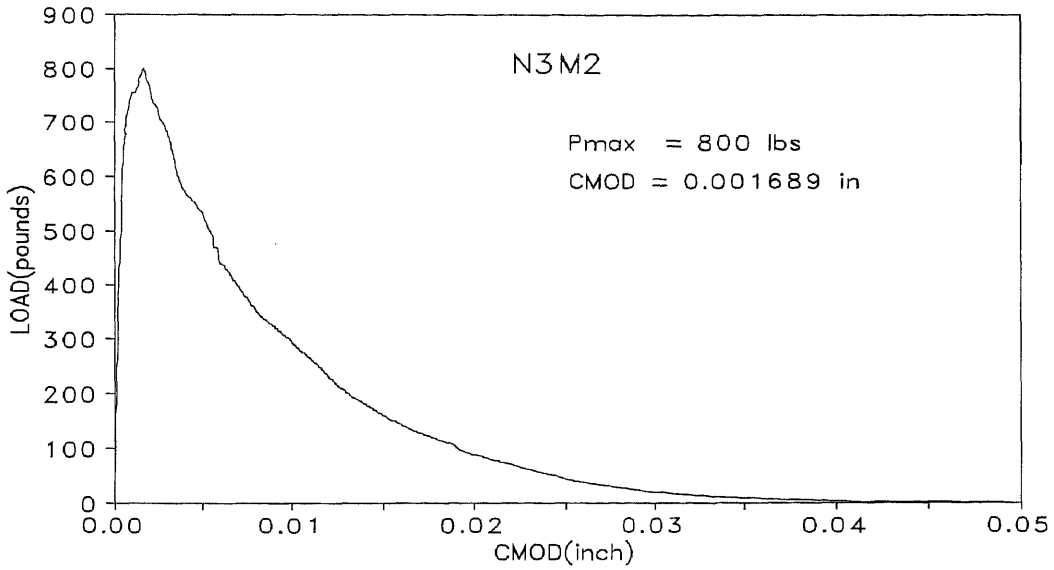

Figure A 12a Load-*CMOD* relationship (N3M2)

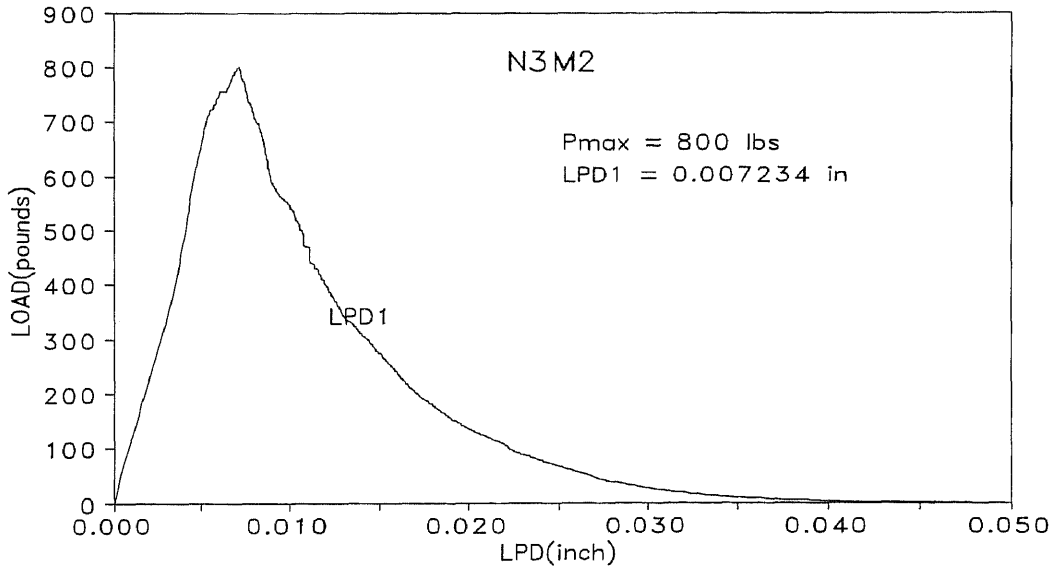

Figure A 12b Load-deflection relationship (N3M2)

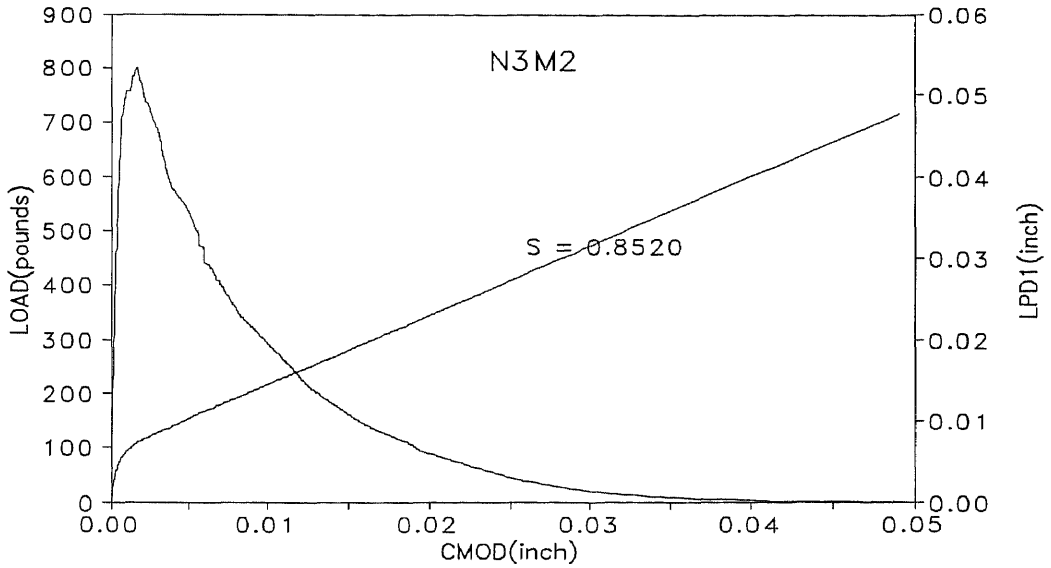

Figure A 12c Load-*CMOD*-deflection (LVDT1) relationship (N3M2)

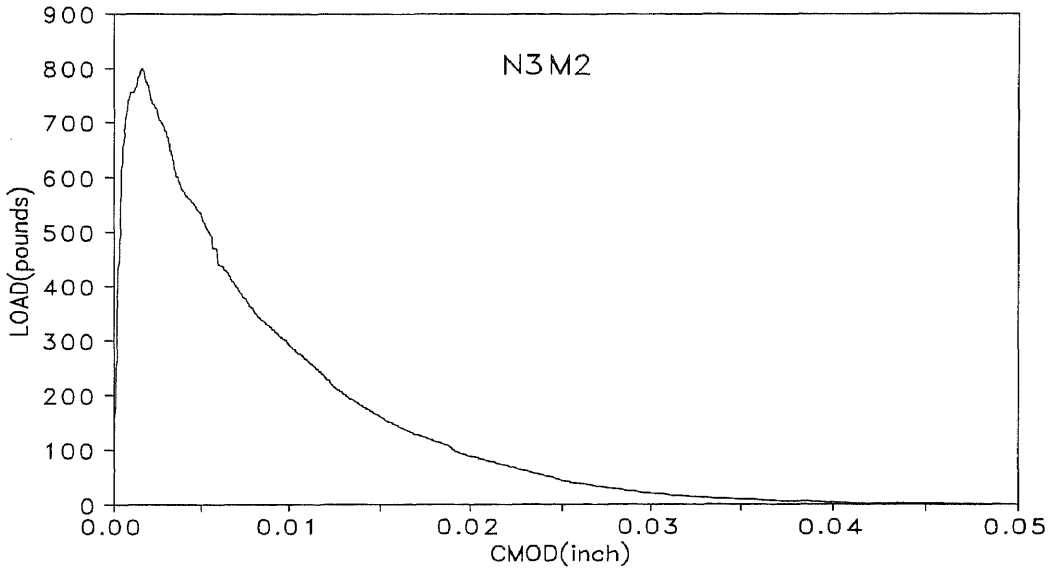

Figure A 12d Load-*CMOD*-deflection (LVDT2) relationship (N3M2)

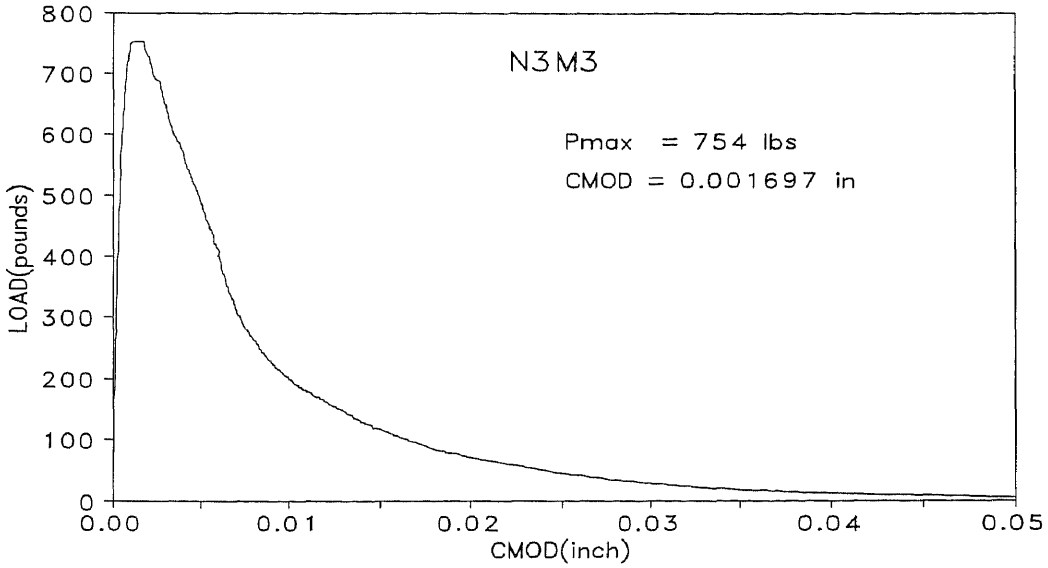

Figure A 13a Load-*CMOD* relationship (N3M3)

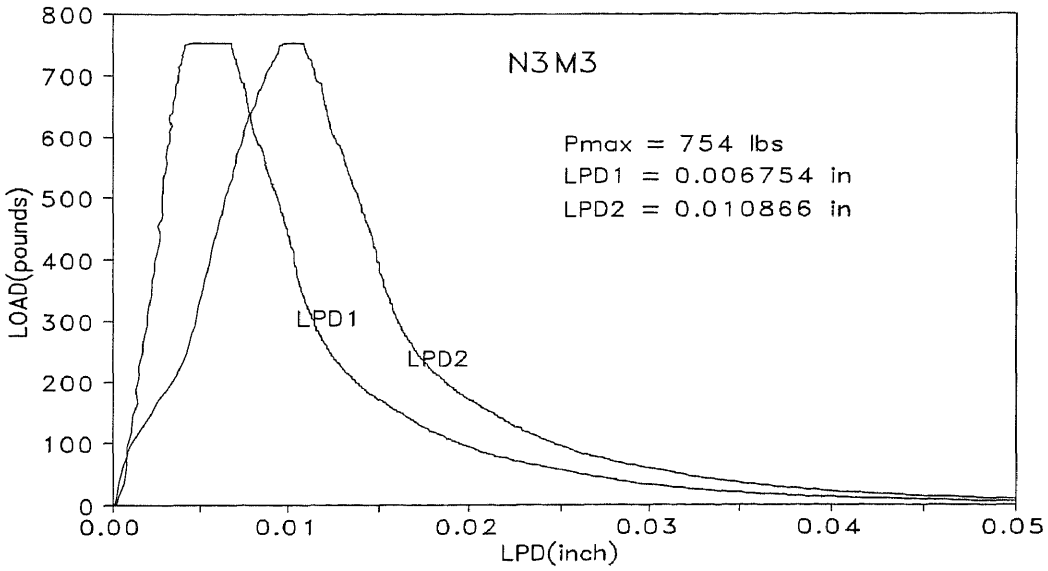

Figure A 13b Load-deflection relationship (N3M3)

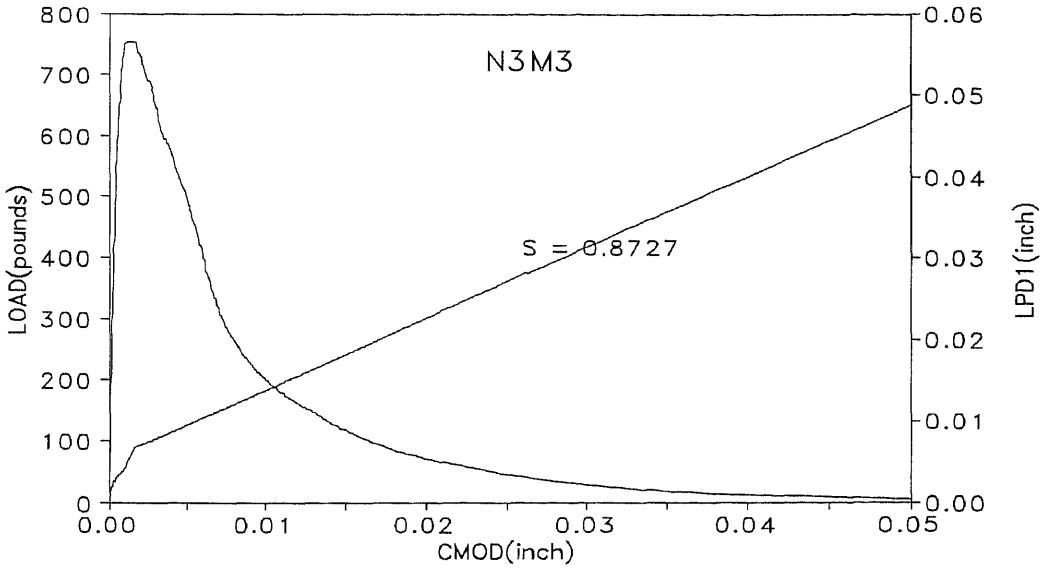

Figure A 13c Load-*CMOD*-deflection (LVDT1) relationship (N3M3)

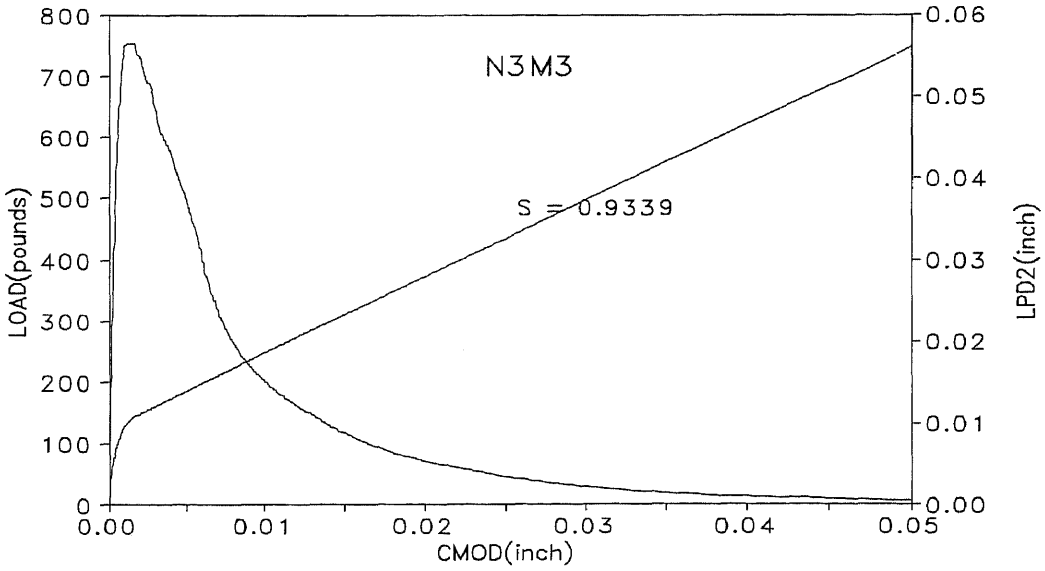

Figure A 13d Load-*CMOD*-deflection (LVDT2) relationship (N3M3)

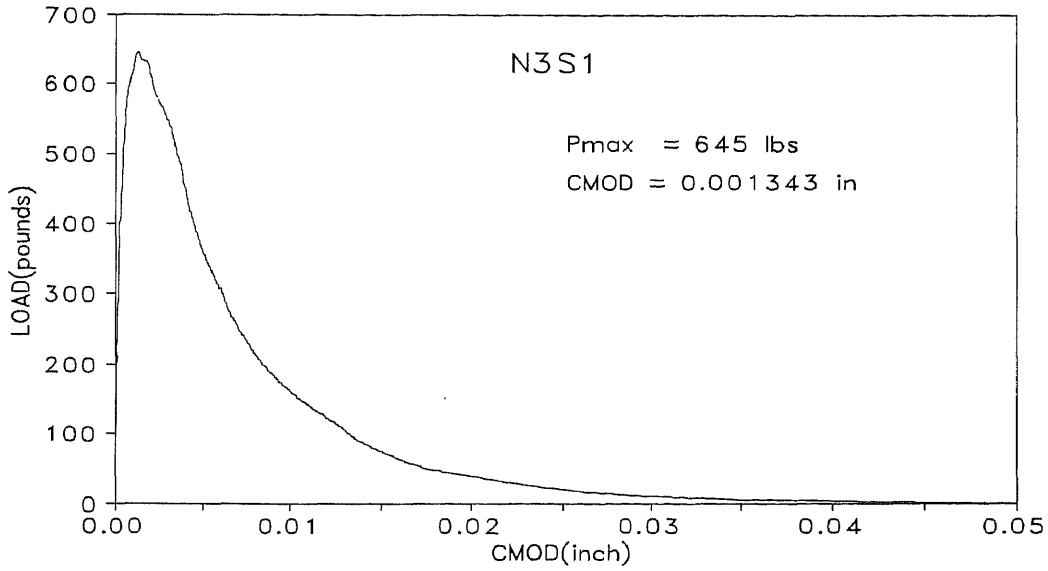

Figure A 14a Load-*CMOD* relationship (N3S1)

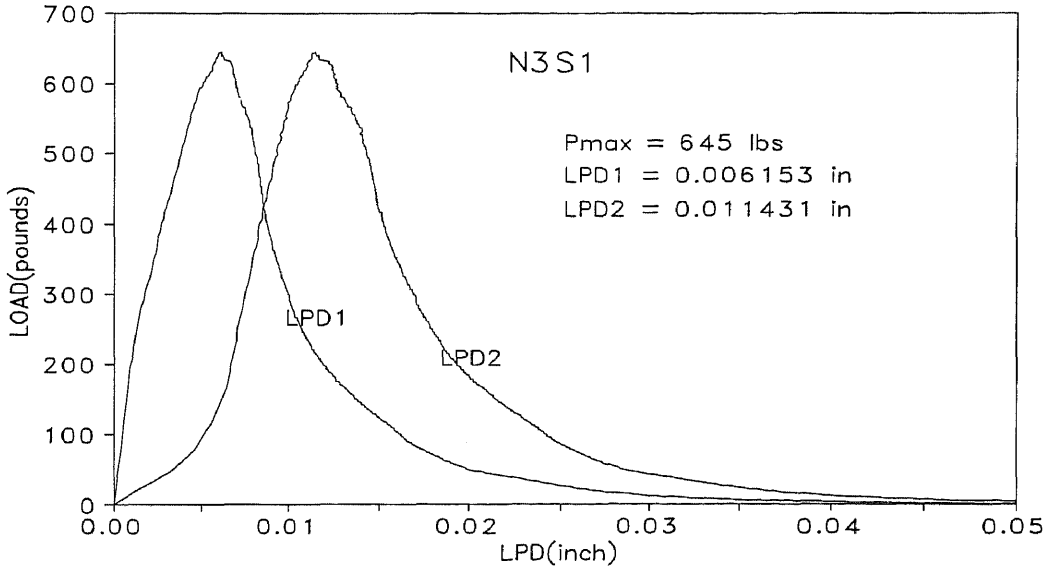

Figure A 14b Load-deflection relationship (N3S1)

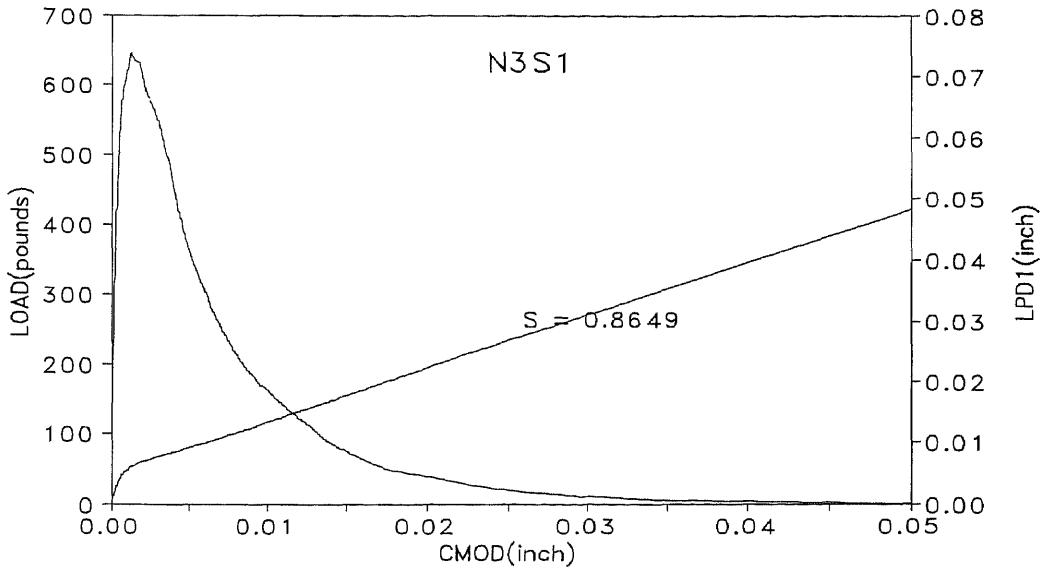

Figure A 14c Load-*CMOD*-deflection (LVDT1) relationship (N3S1)

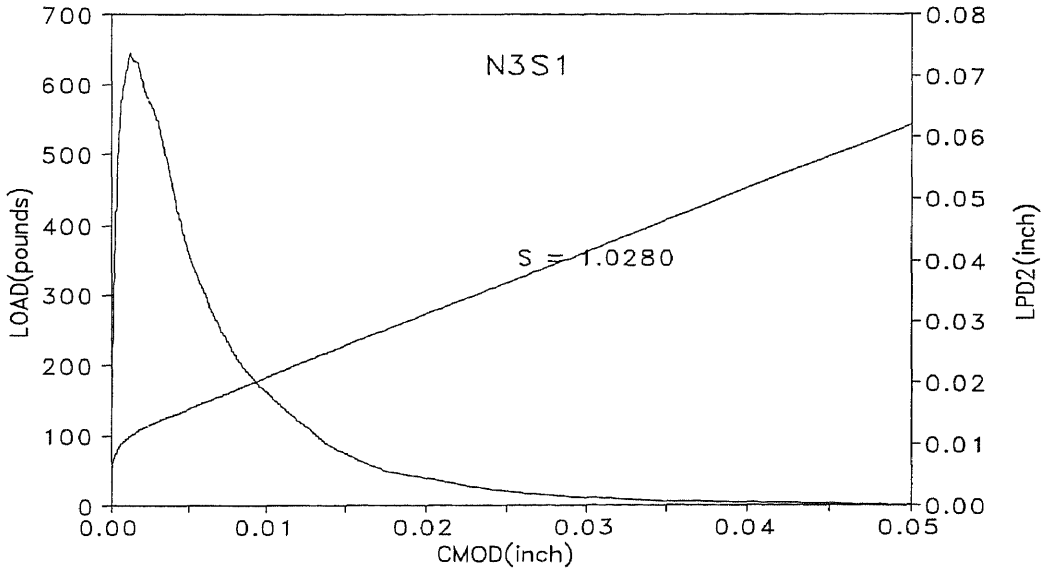

Figure A 14d Load-*CMOD*-deflection (LVDT2) relationship (N3S1)

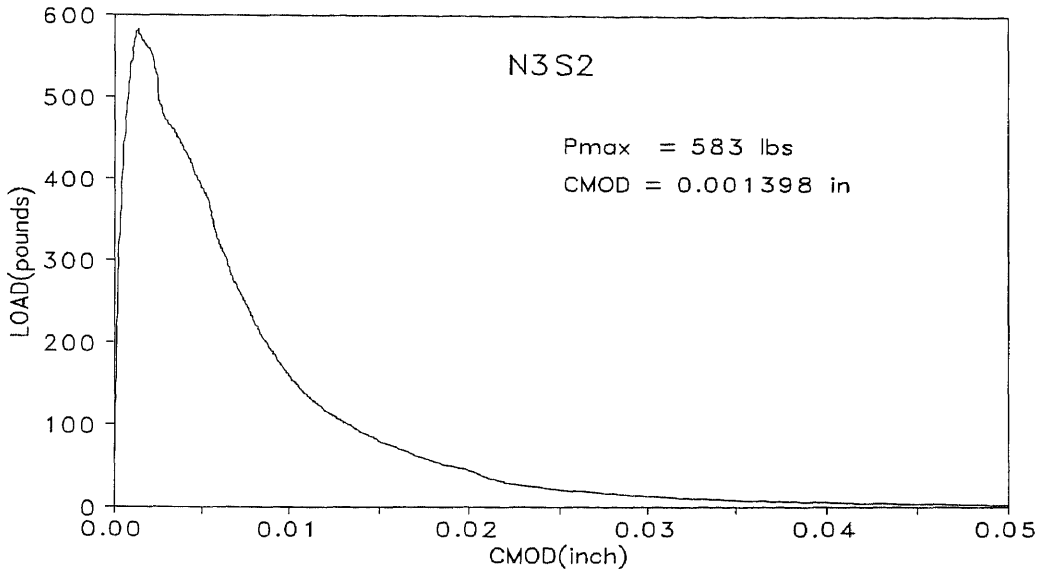

Figure A 15a Load-*CMOD* relationship (N3S2)

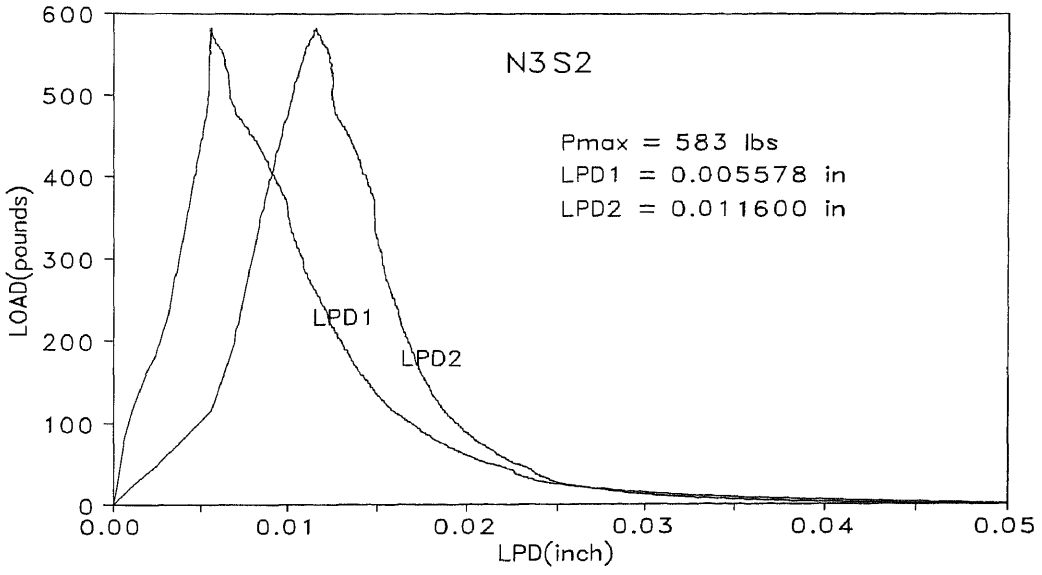

Figure A 15b Load-deflection relationship (N3S2)

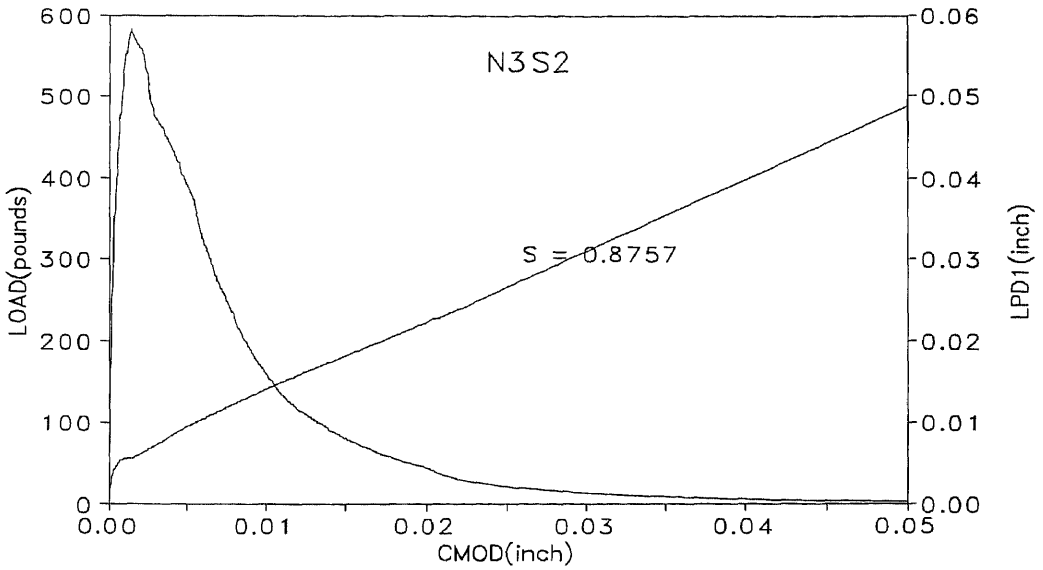

Figure A 15c Load-*CMOD*-deflection (LVDT1) relationship (N3S2)

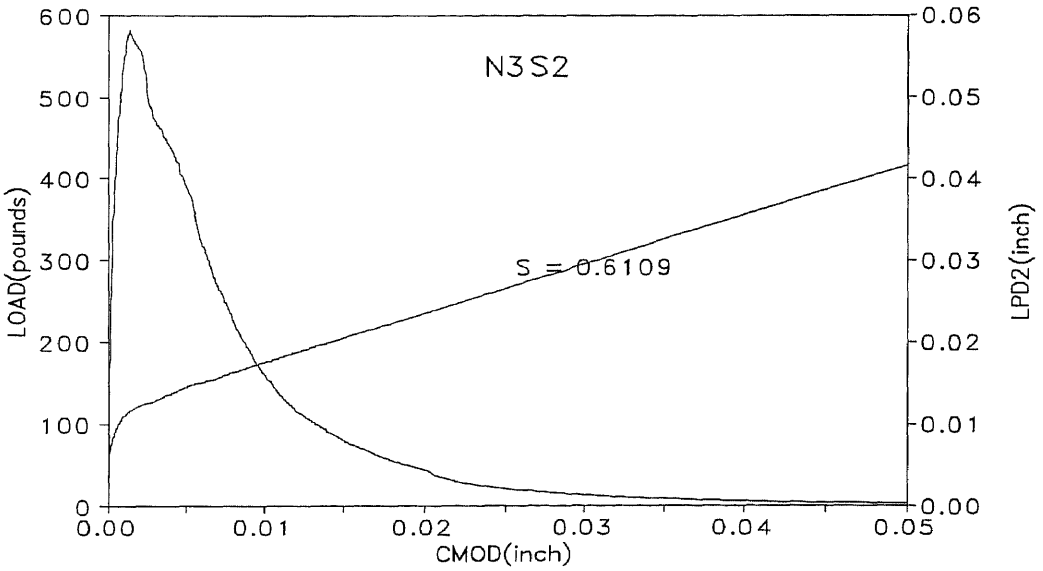

Figure A 15d Load-*CMOD*-deflection (LVDT2) relationship (N3S2)

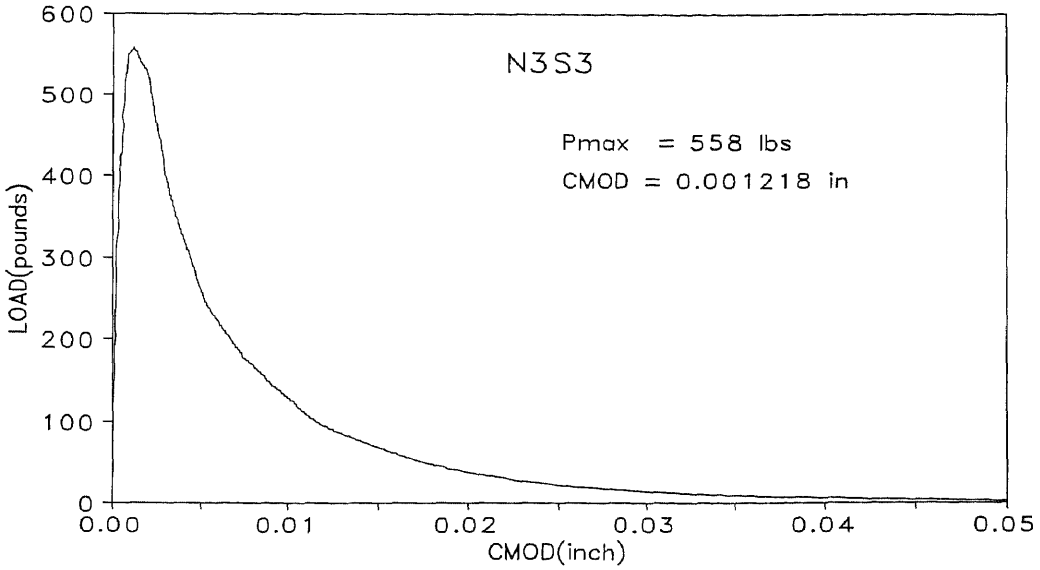

Figure A 16a Load-*CMOD* relationship (N3S3)

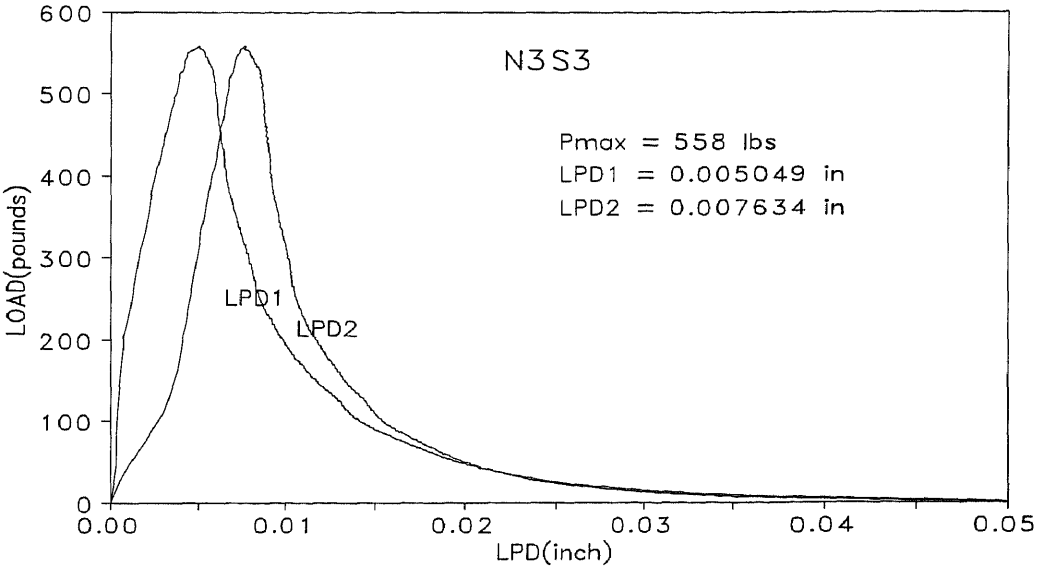

Figure A 16b Load-deflection relationship (N3S3)

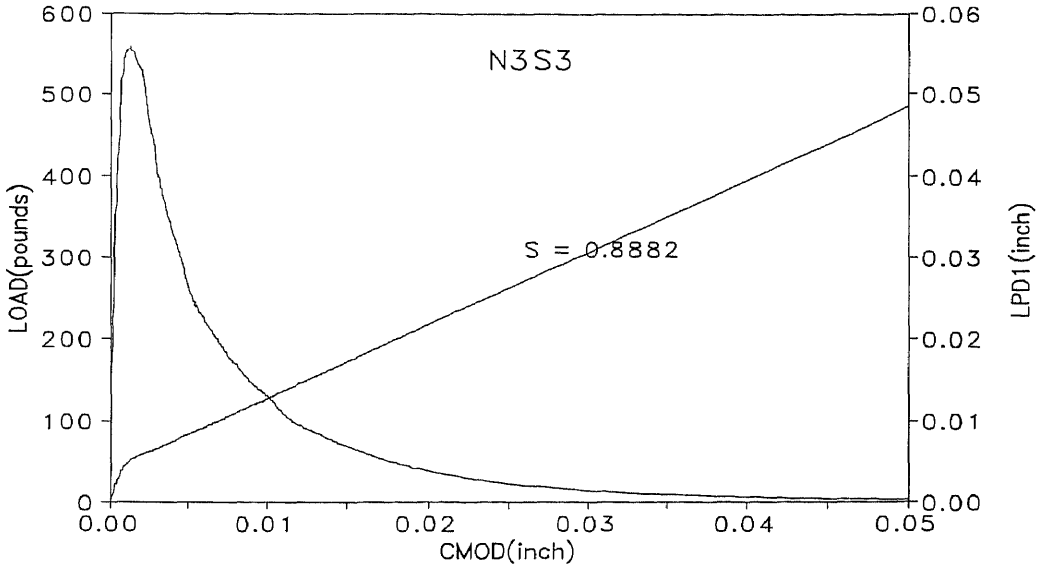

Figure A 16c Load-*CMOD*-deflection (LVDT1) relationship (N3S3)

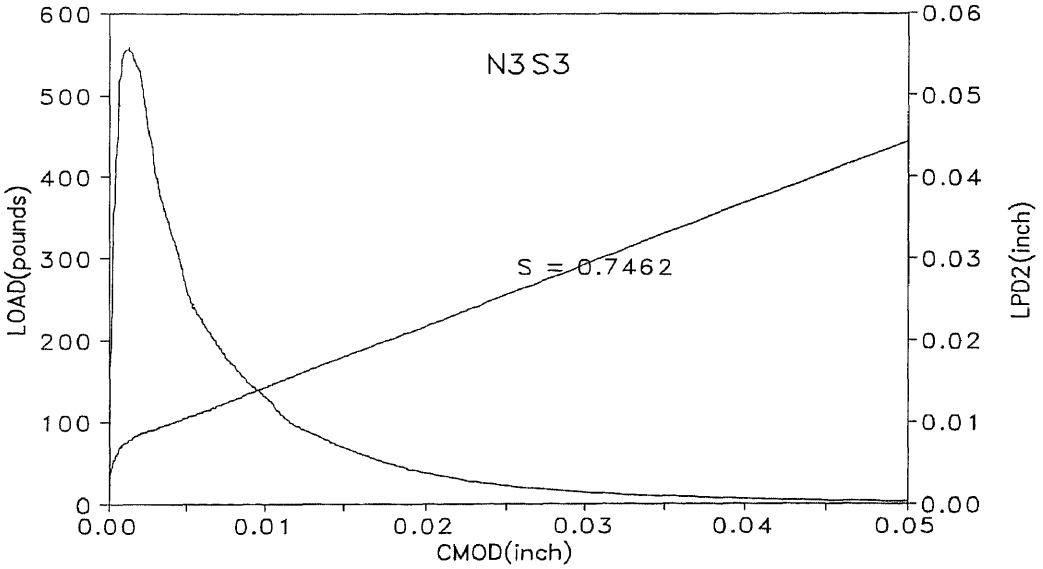

Figure A 16d Load-*CMOD*-deflection (LVDT2) relationship (N3S3)

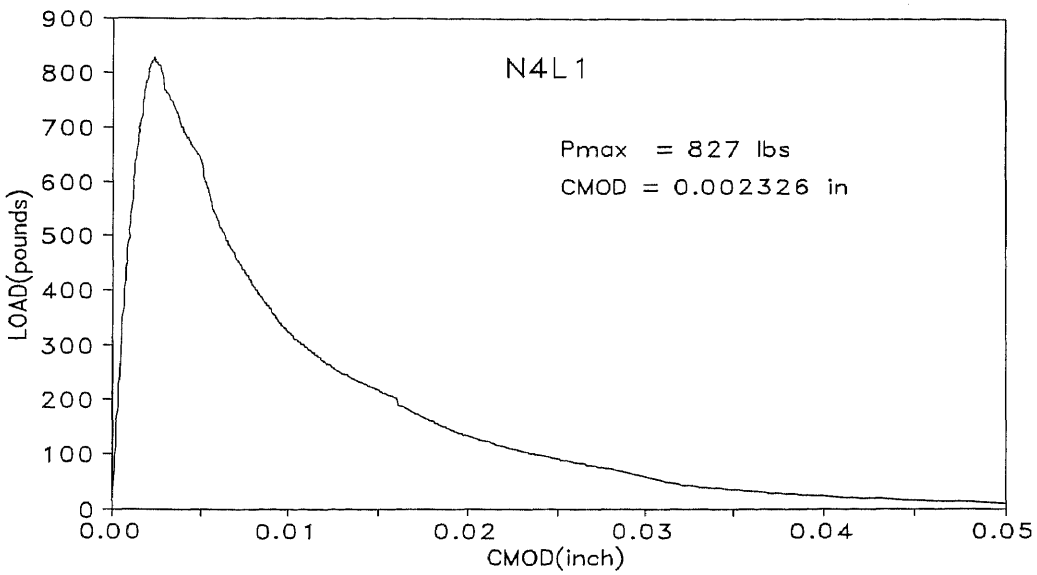

Figure A 17a Load-*CMOD* relationship (N4L1)

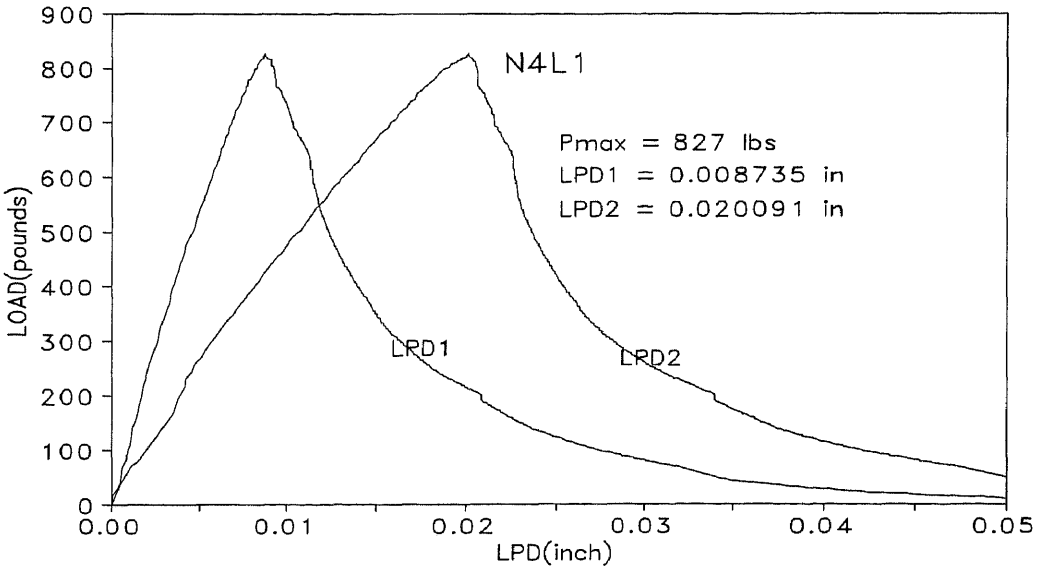

Figure A 17b Load-deflection relationship (N4L1)

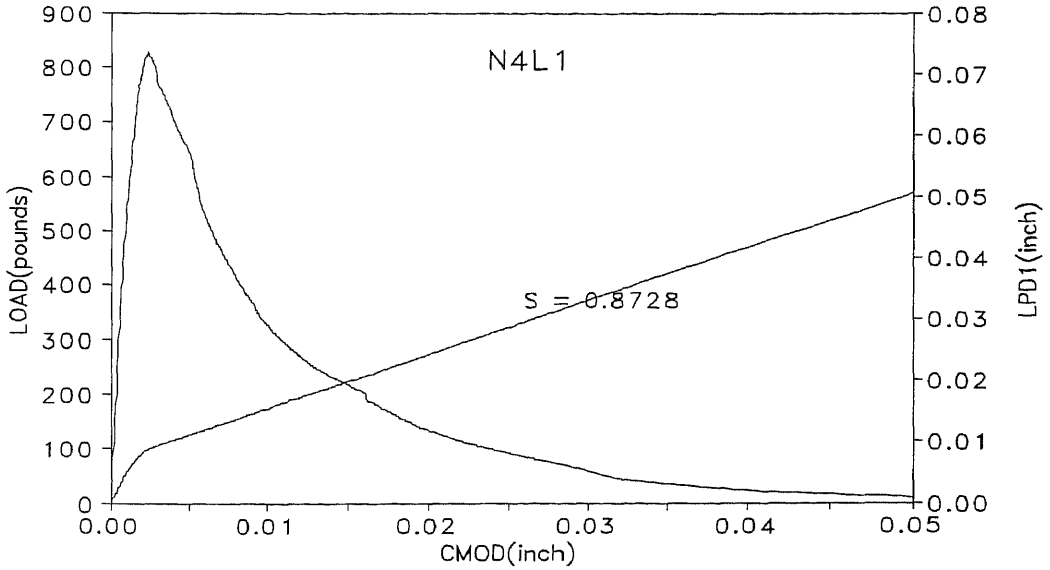

Figure A 17c Load-*CMOD*-deflection (LVDT1) relationship (N4L1)

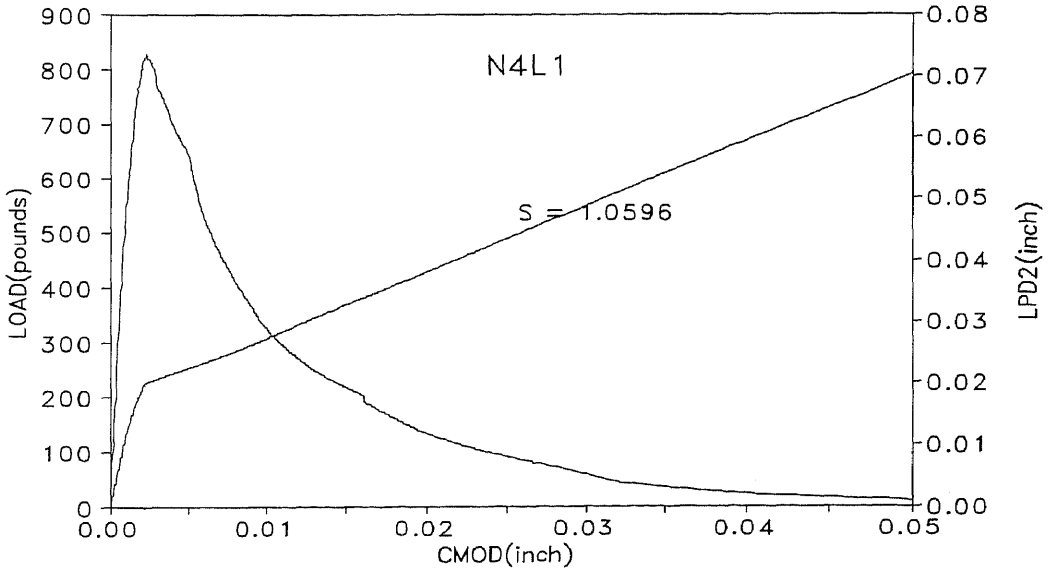

Figure A 17d Load-*CMOD*-deflection (LVDT2) relationship (N4L1)

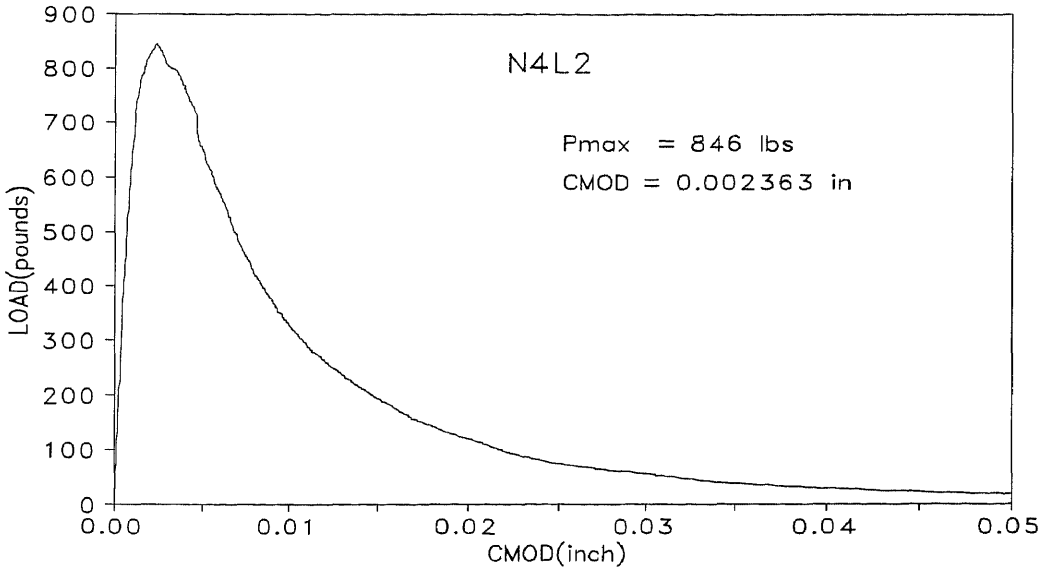

Figure A 18a Load-*CMOD* relationship (N4L2)

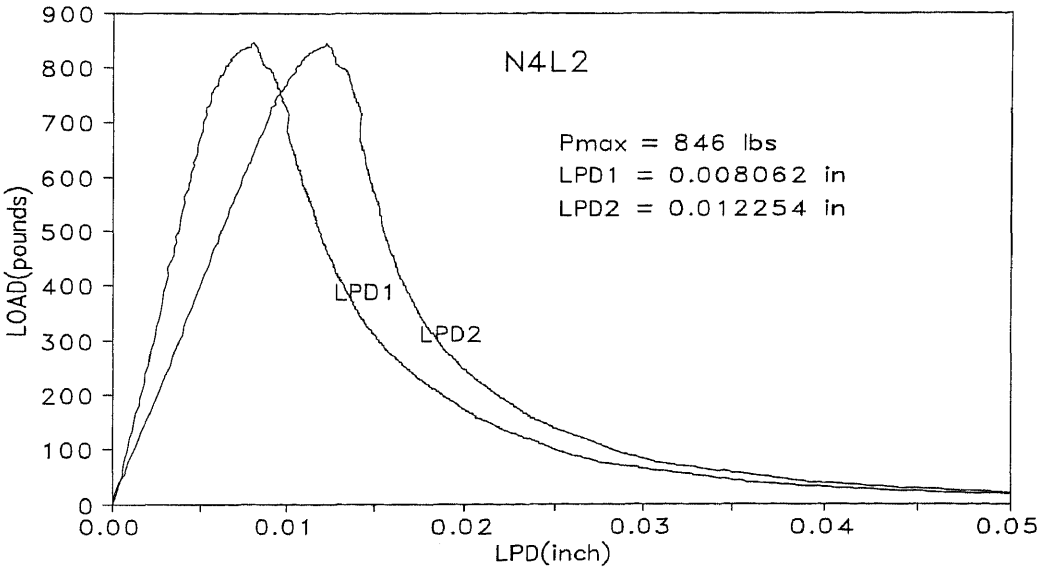

Figure A 18b Load-deflection relationship (N4L2)

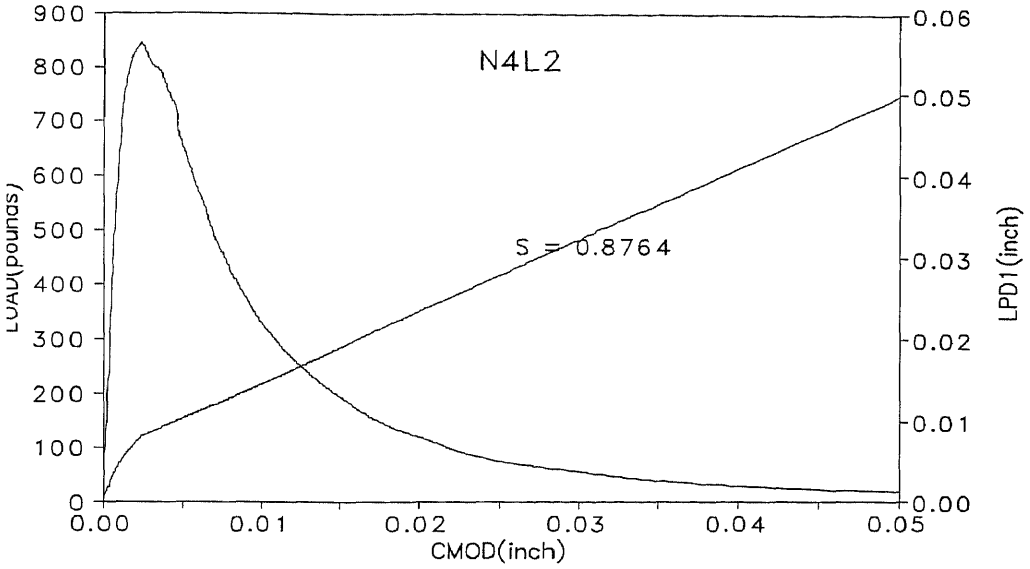

Figure A 18c Load-*CMOD*-deflection (LVDT1) relationship (N4L2)

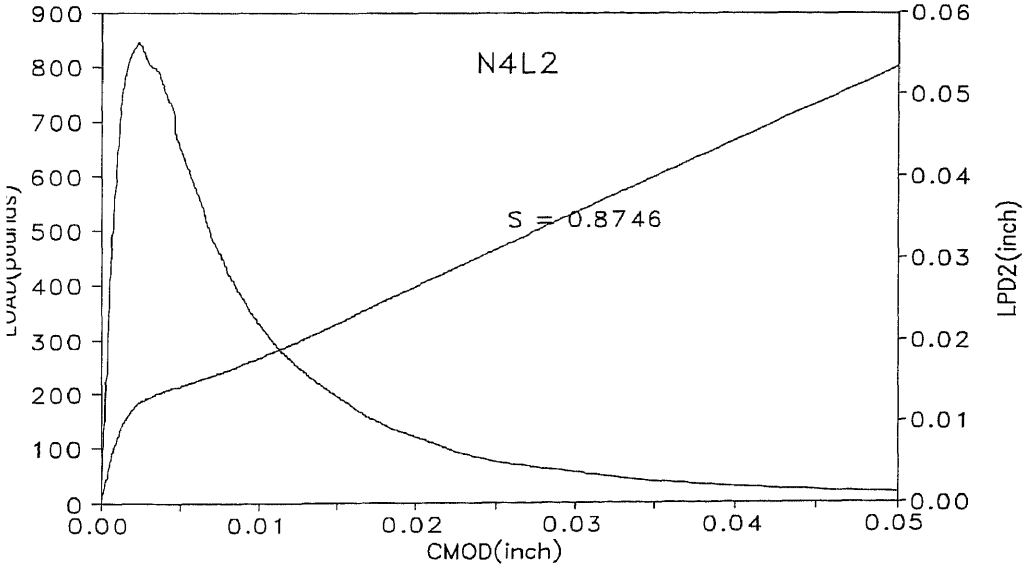

Figure A 18d Load-*CMOD*-deflection (LVDT2) relationship (N4L2)

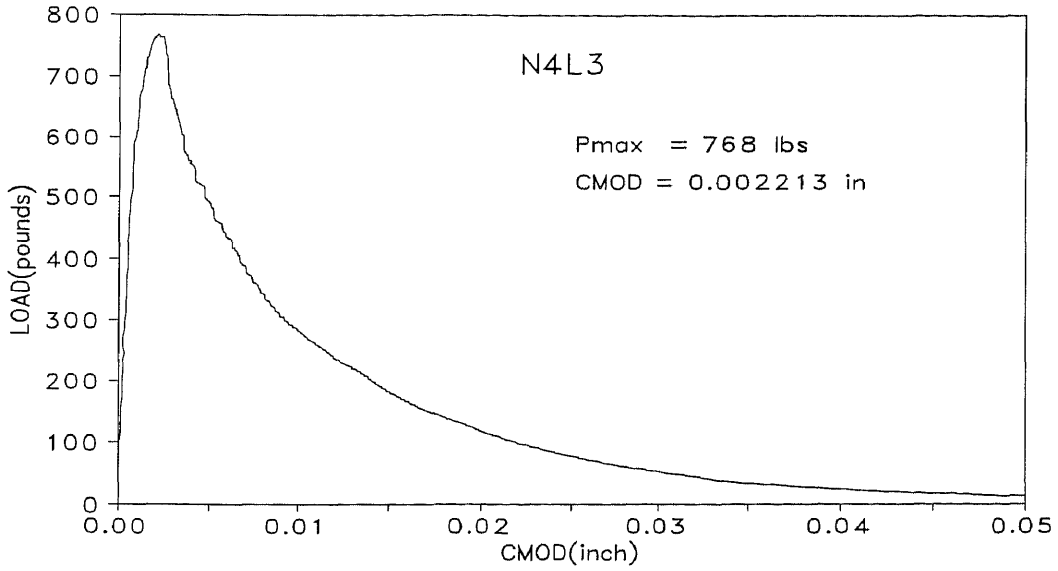

Figure A 19a Load-*CMOD* relationship (N4L3)

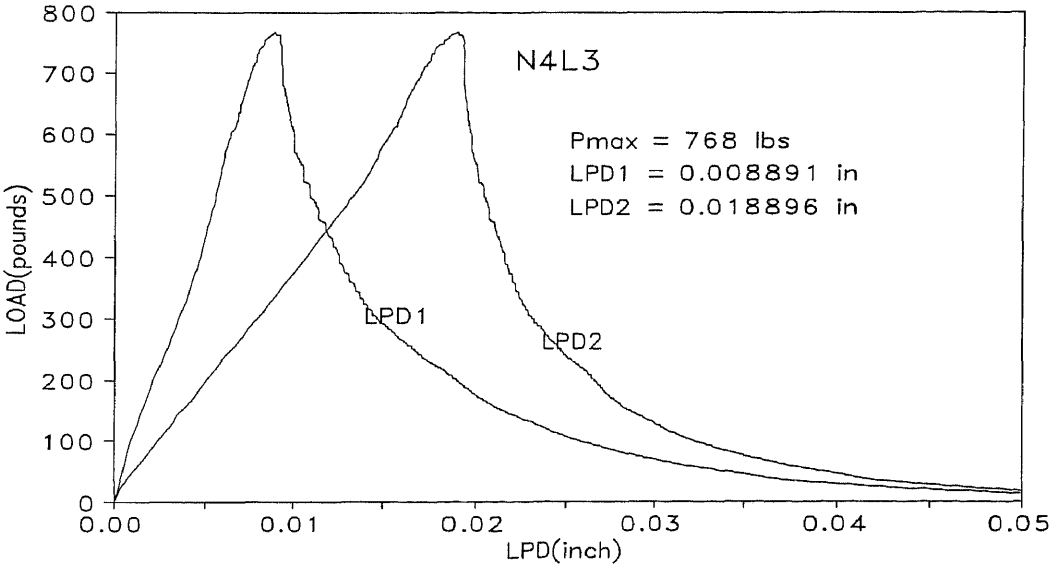

Figure A 19b Load-deflection relationship (N4L3)

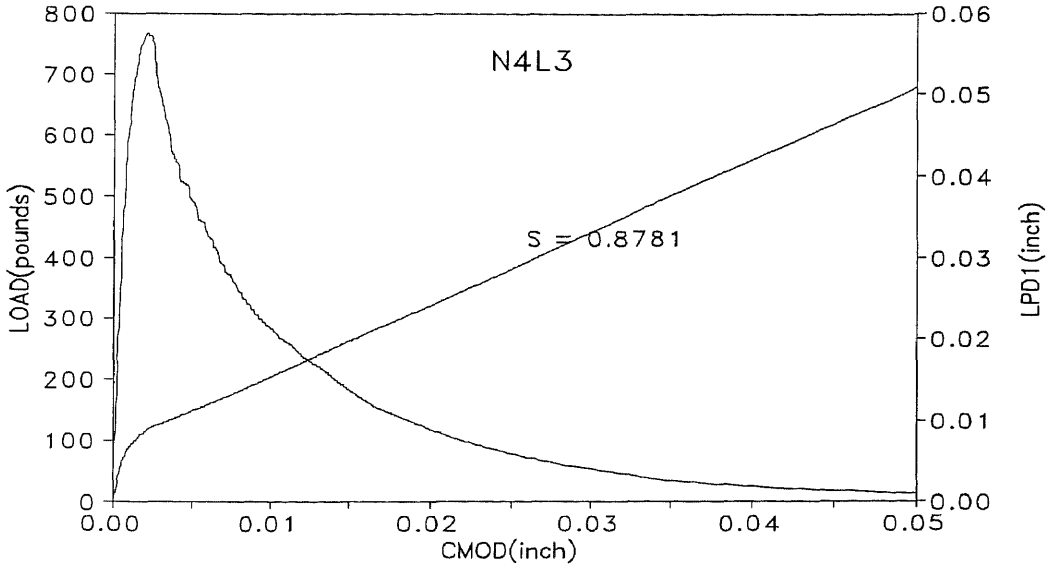

Figure A 19c Load-*CMOD*-deflection (LVDT1) relationship (N4L3)

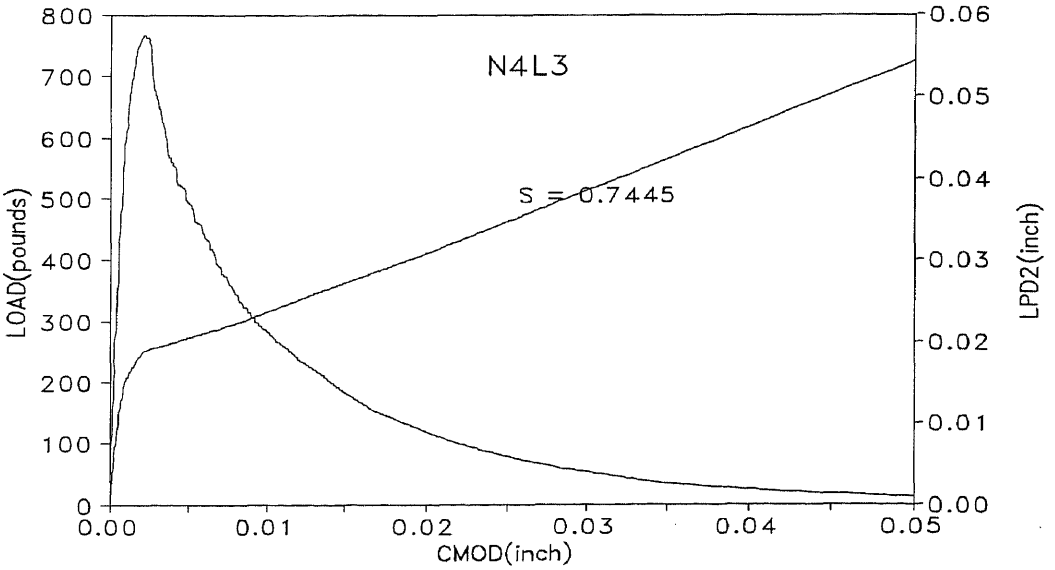

Figure A 19d Load-*CMOD*-deflection (LVDT2) relationship (N4L3)

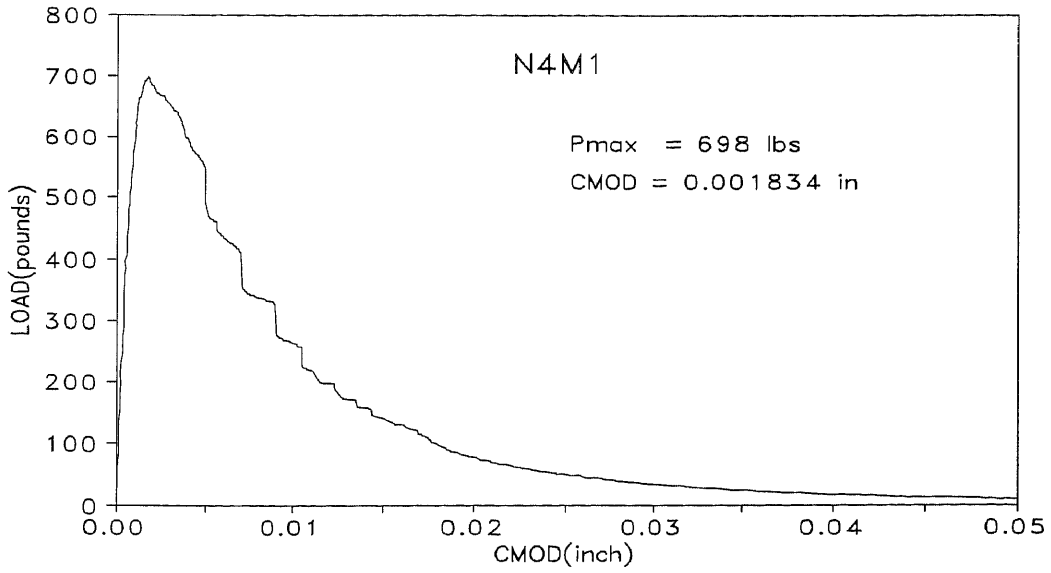

Figure A 20a Load-*CMOD* relationship (N4M1)

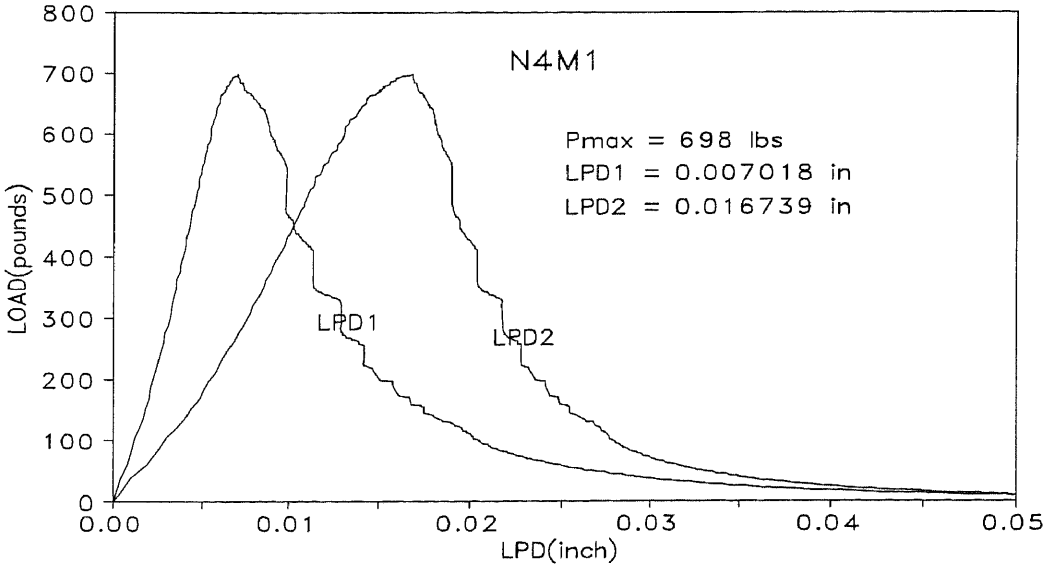

Figure A 20b Load-deflection relationship (N4M1)

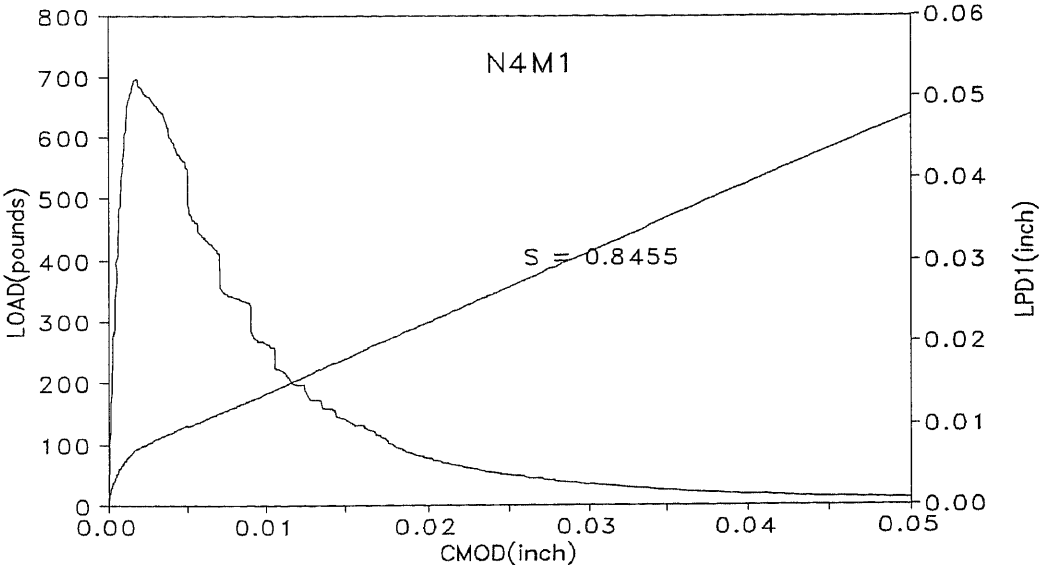

Figure A 20c Load-*CMOD*-deflection (LVDT1) relationship (N4M1)

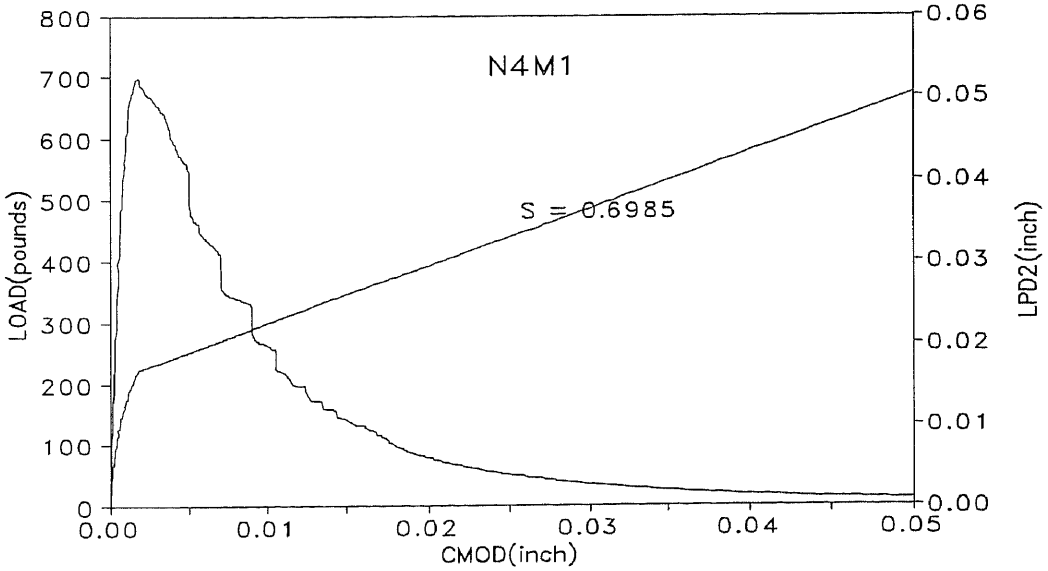

Figure A 20d Load-*CMOD*-deflection (LVDT2) relationship (N4M1)

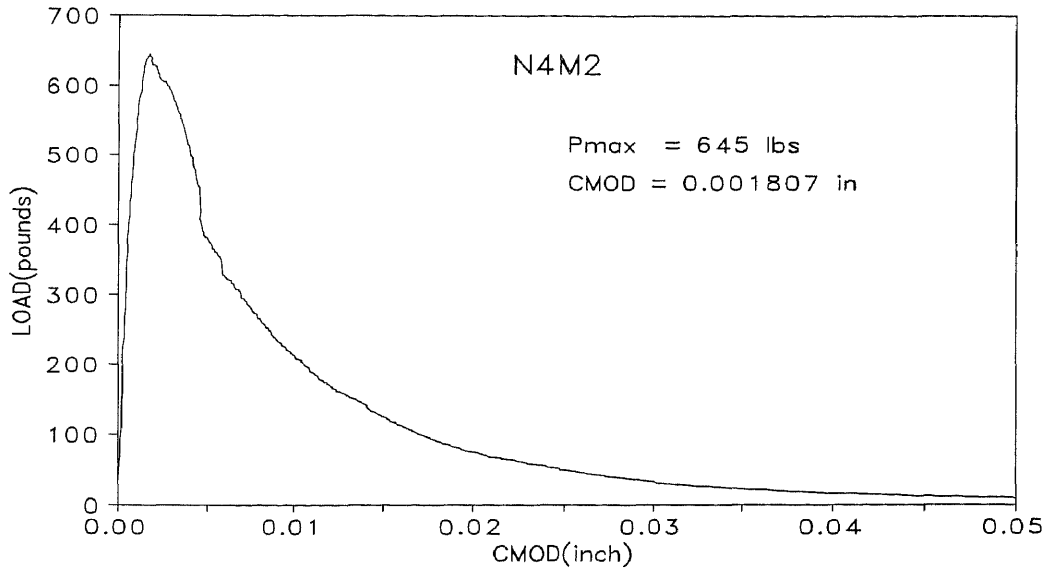

Figure A 21a Load-*CMOD* relationship (N4M2)

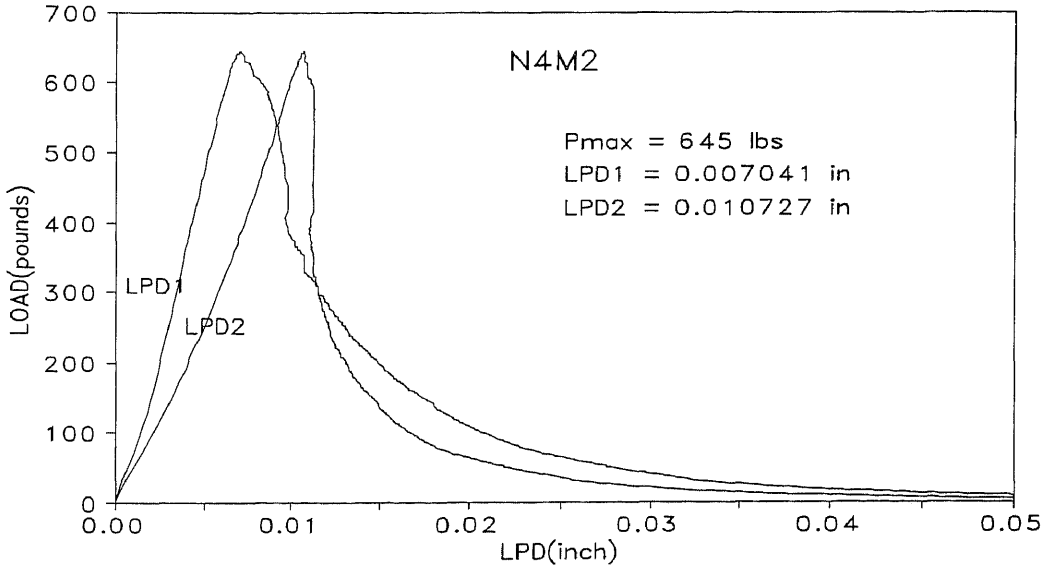

Figure A 21b Load-deflection relationship (N4M2)

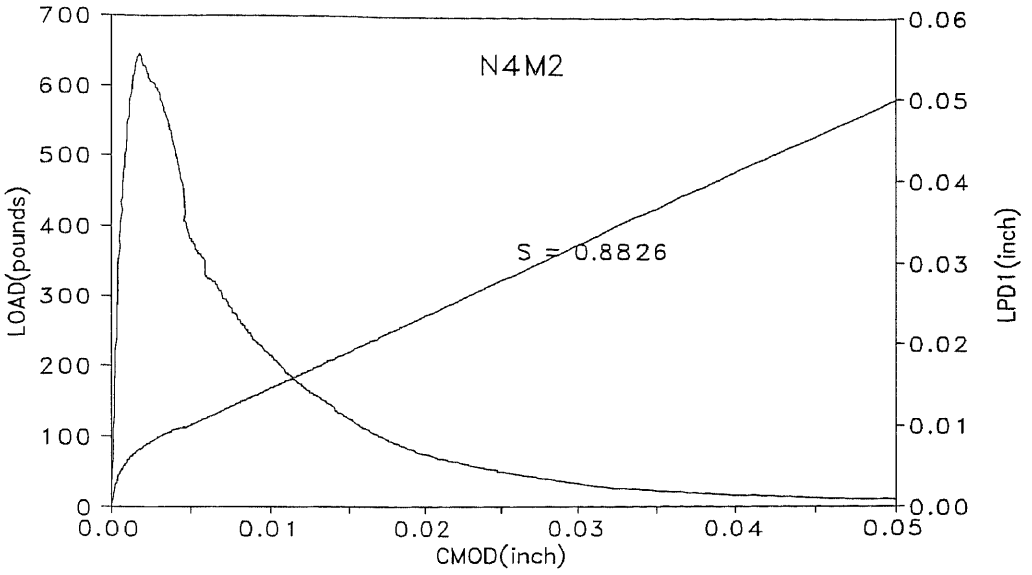

Figure A 21c Load-*CMOD*-deflection (LVDT1) relationship (N4M2)

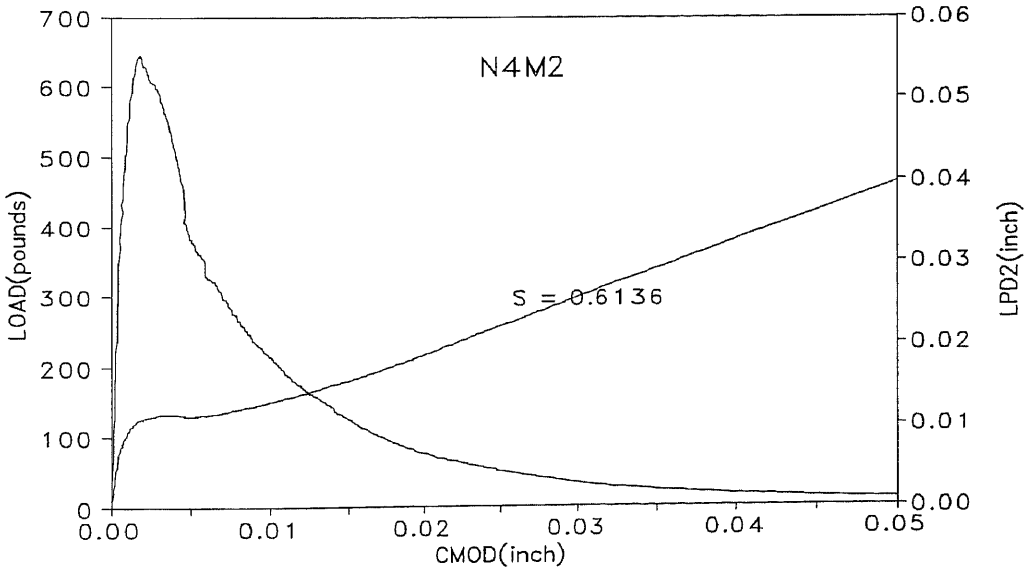

Figure A 21d Load-*CMOD*-deflection (LVDT2) relationship (N4M2)

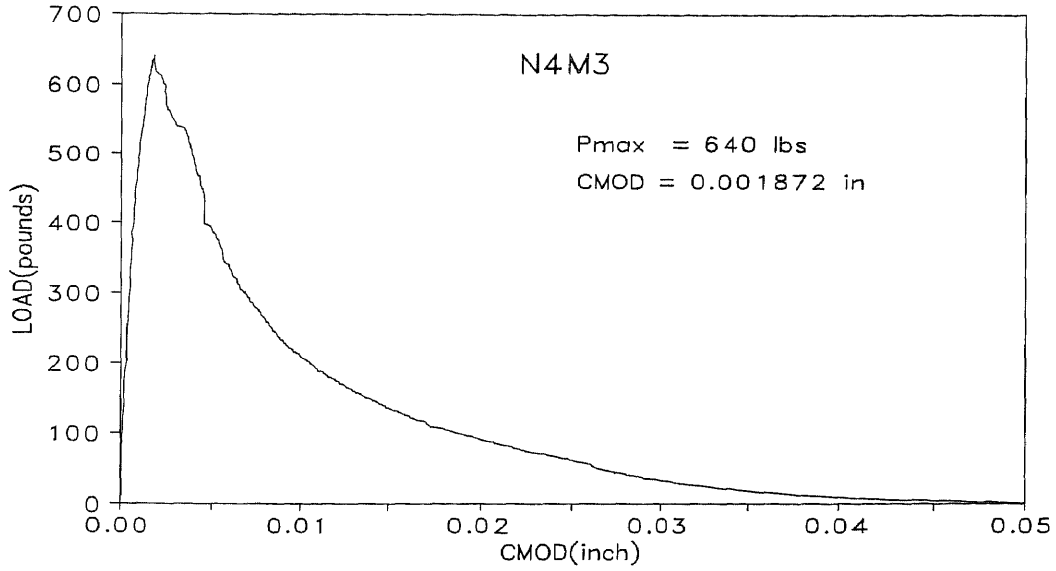

Figure A 22a Load-*CMOD* relationship (N4M3)

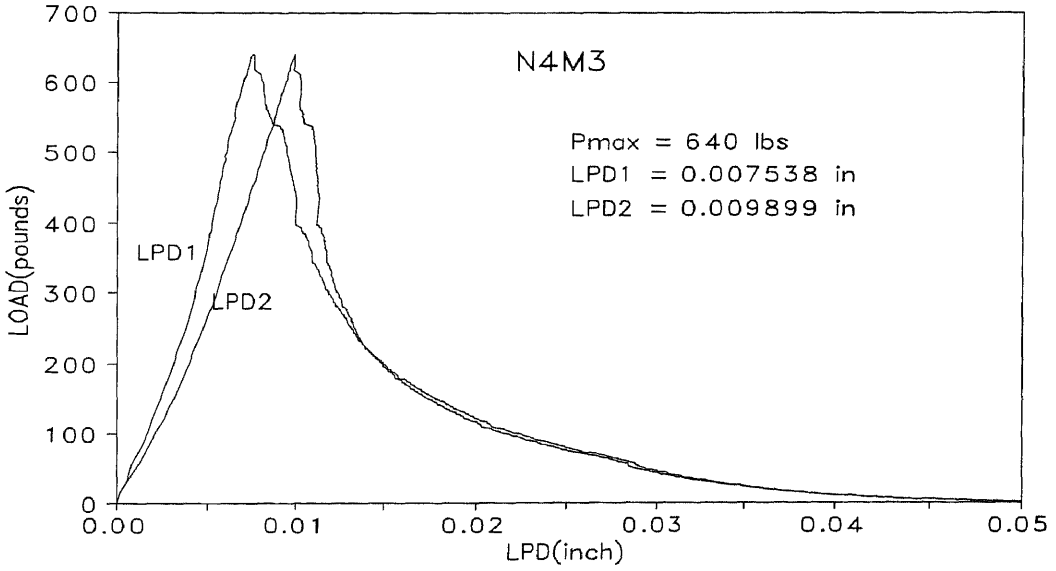

Figure A 22b Load-deflection relationship (N4M3)

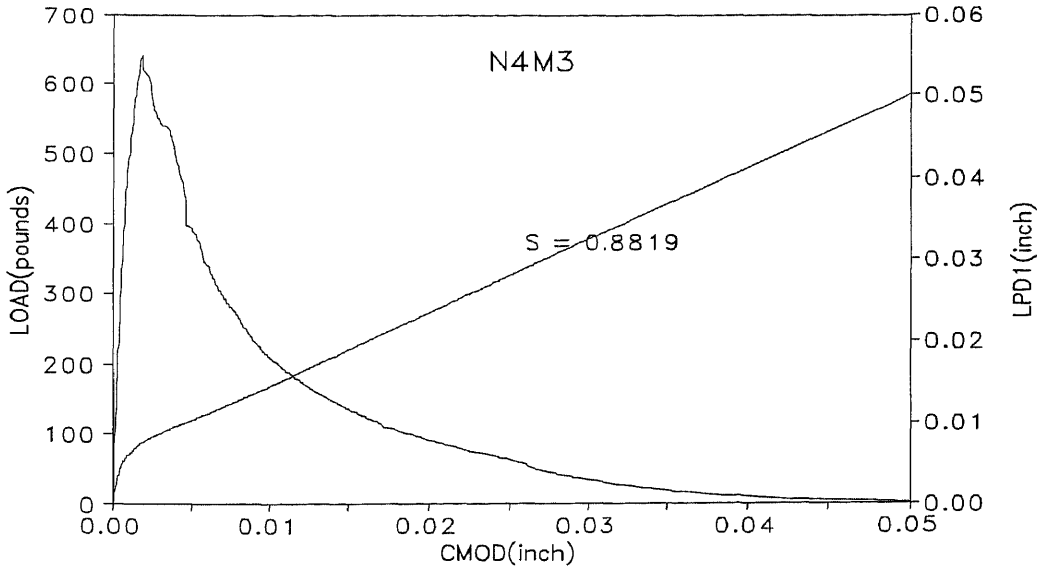

Figure A 22c Load-*CMOD*-deflection (LVDT1) relationship (N4M3)

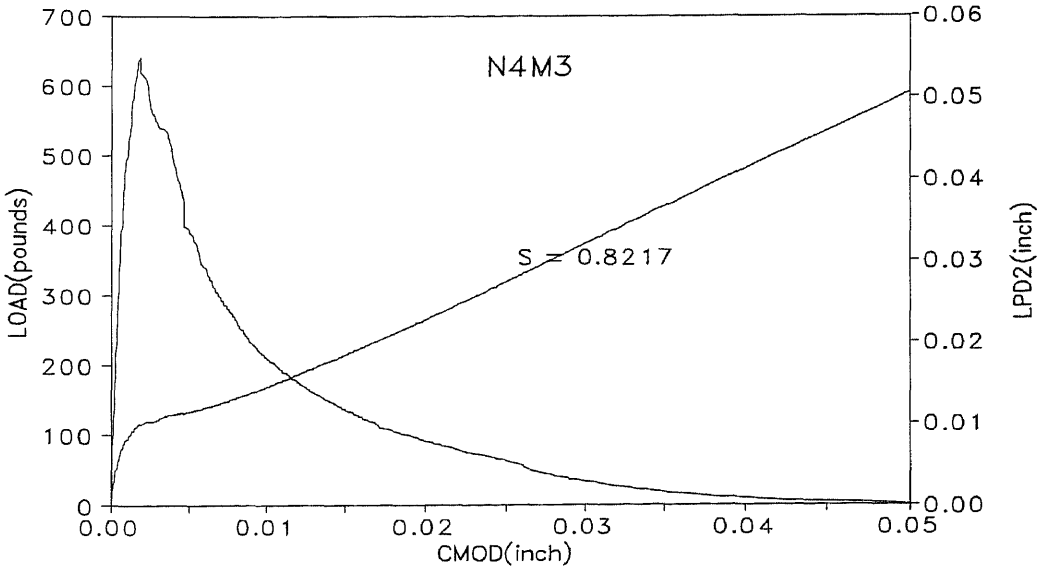

Figure A 22d Load-*CMOD*-deflection (LVDT2) relationship (N4M3)

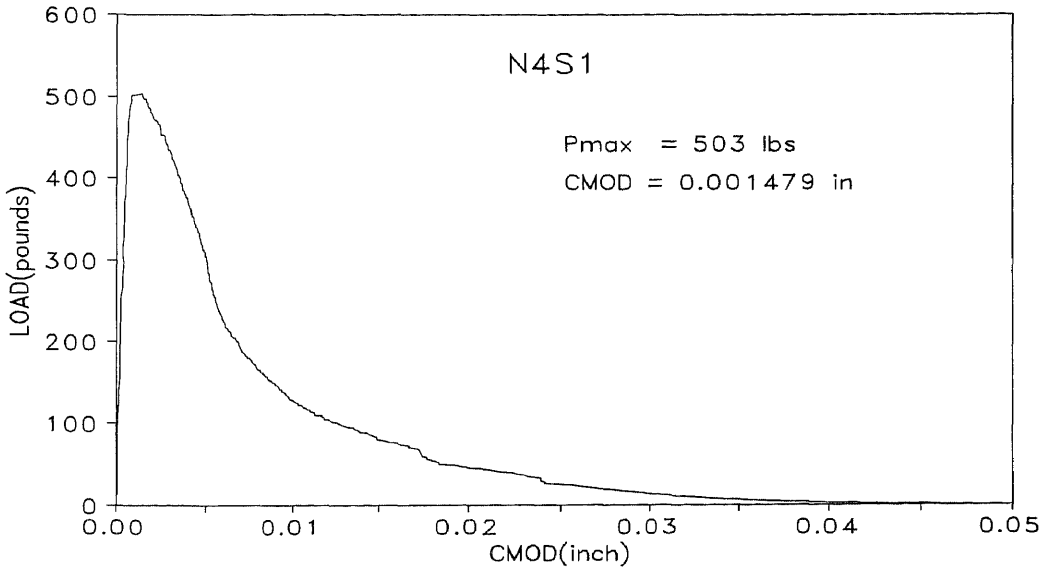

Figure A 23a Load-*CMOD* relationship (N4S1)

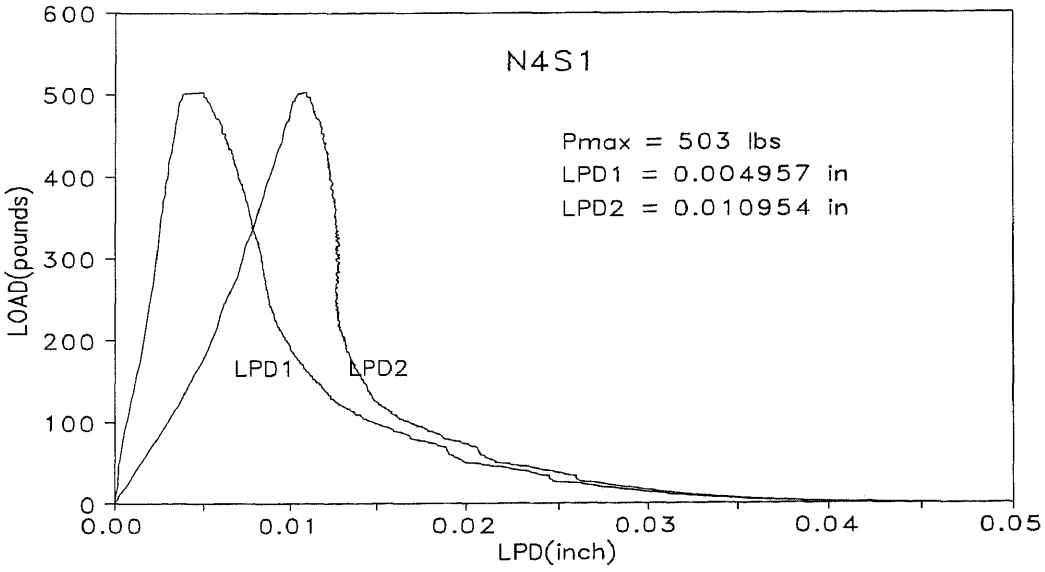

Figure A 23b Load-deflection relationship (N4S1)

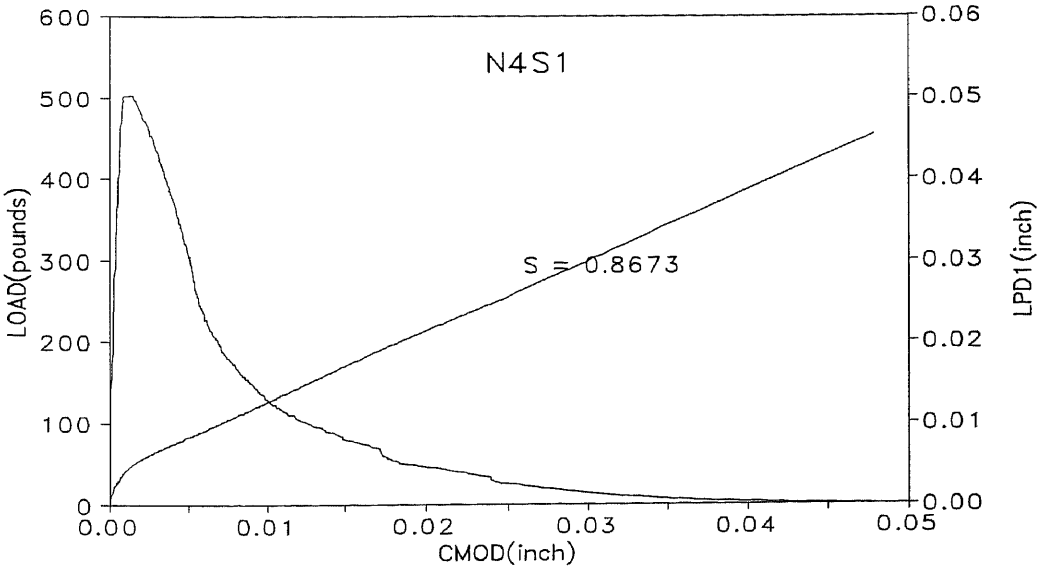

Figure A 23c Load-*CMOD*-deflection (LVDT1) relationship (N4S1)

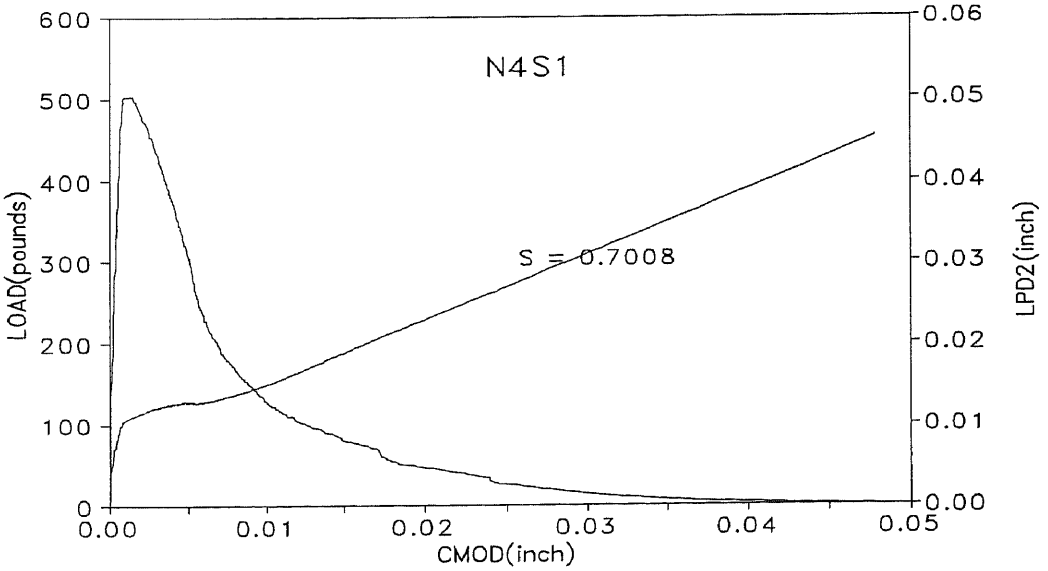

Figure A 23d Load-*CMOD*-deflection (LVDT2) relationship (N4S1)

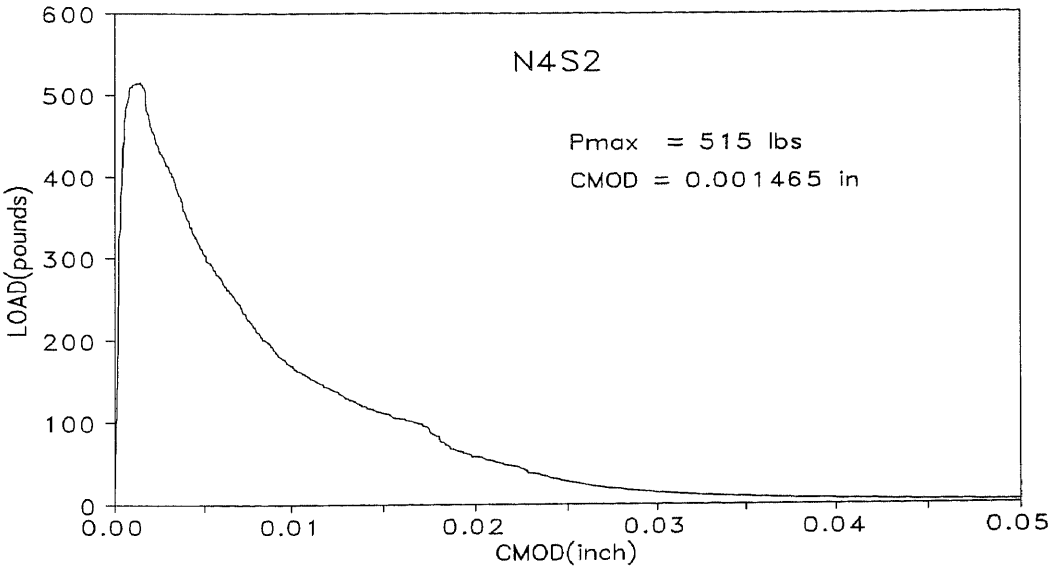

Figure A 24a Load-*CMOD* relationship (N4S2)

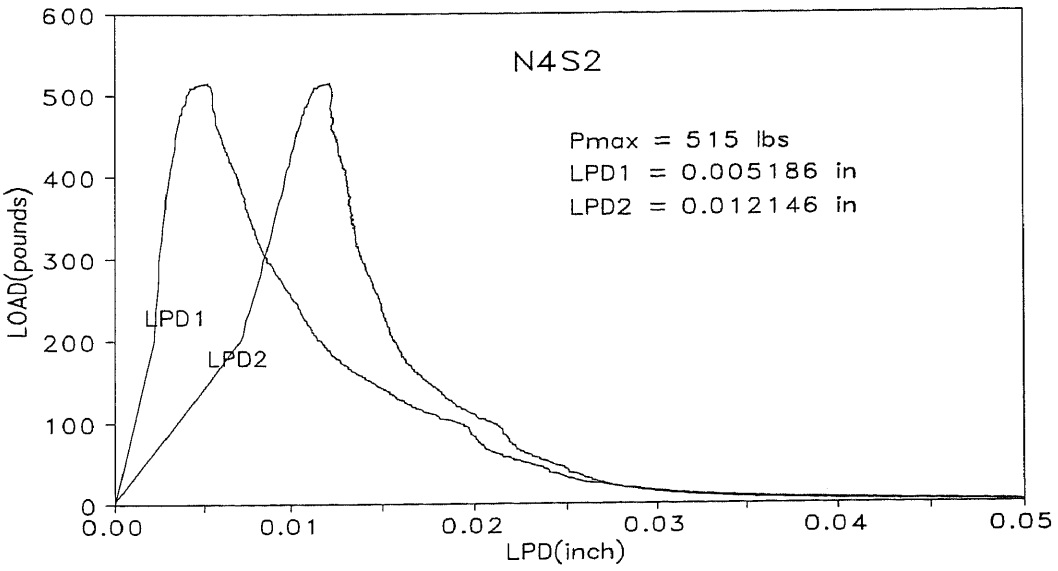

Figure A 24b Load-deflection relationship (N4S2)

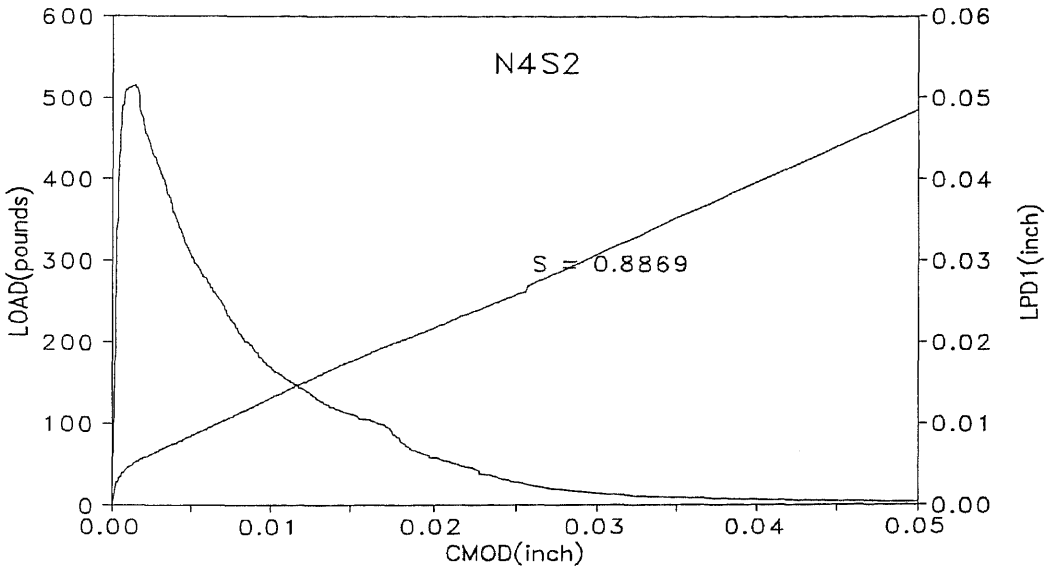

Figure A 24c Load-*CMOD*-deflection (LVDT1) relationship (N4S2)

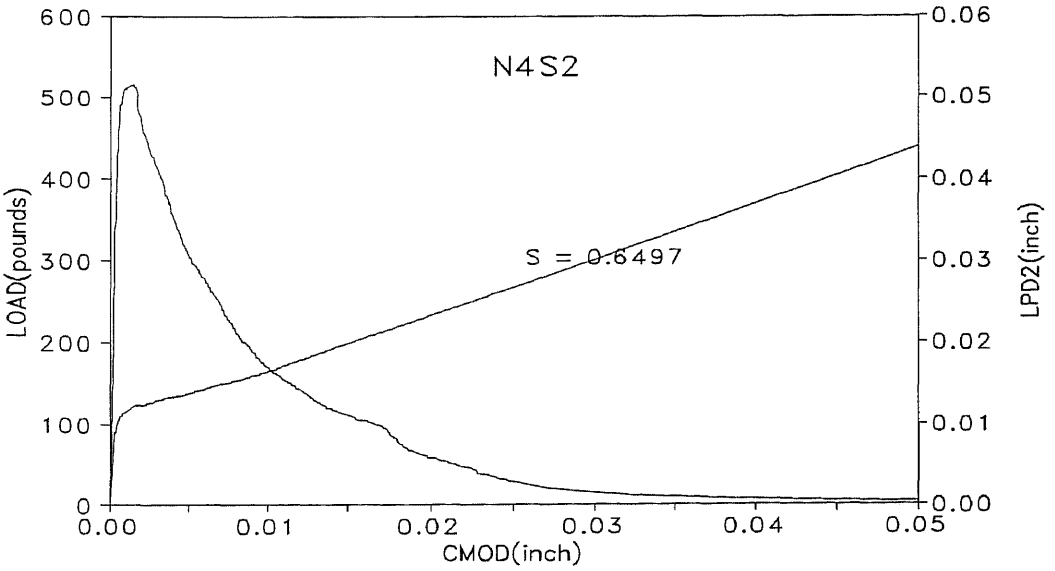

Figure A 24d Load-*CMOD*-deflection (LVDT2) relationship (N4S2)

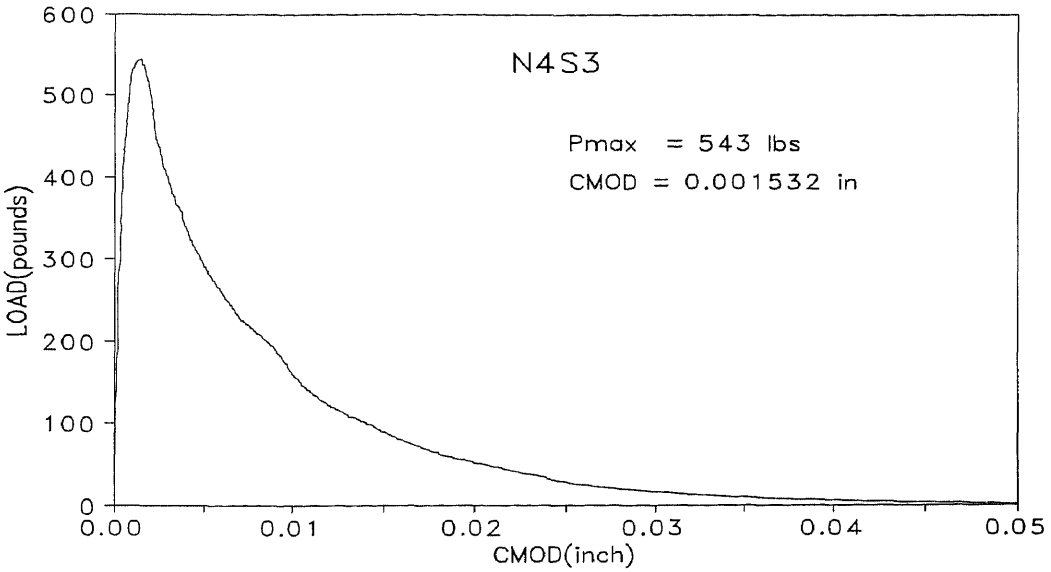

Figure A 25a Load-*CMOD* relationship (N4S3)

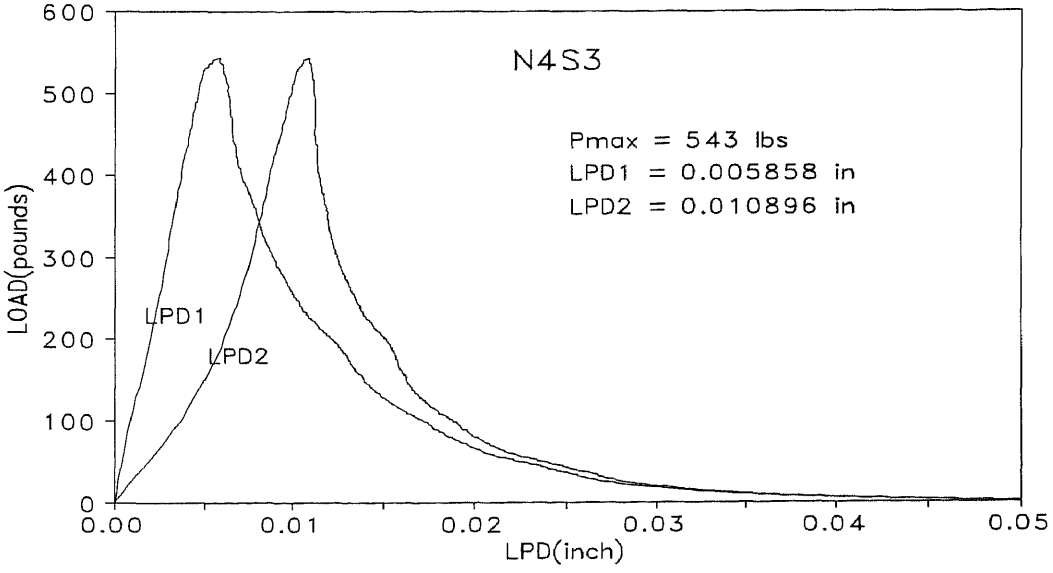

Figure A 25b Load-deflection relationship (N4S3)

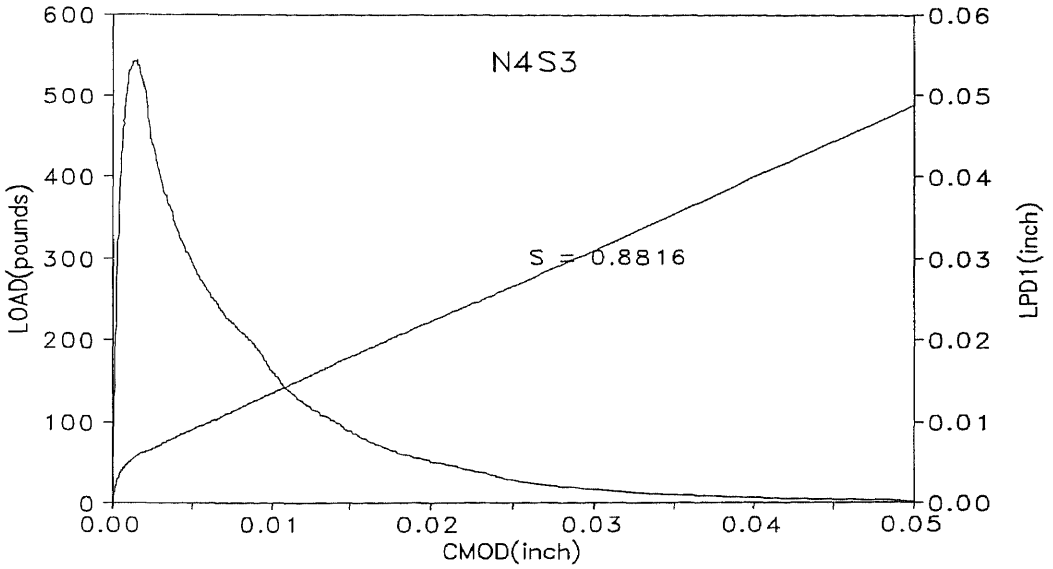

Figure A 25c Load-*CMOD*-deflection (LVDT1) relationship (N4S3)

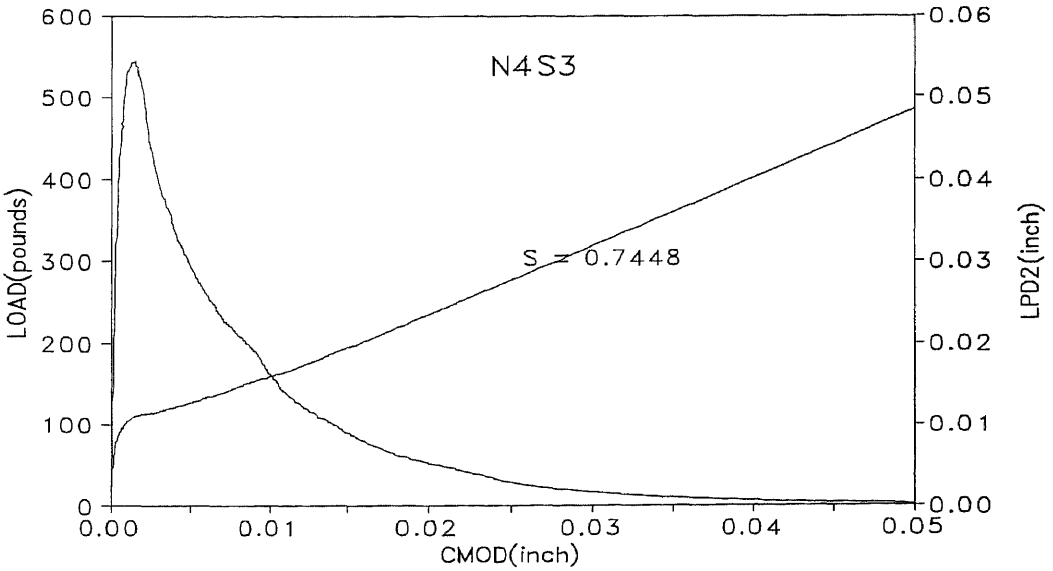

Figure A 25d Load-*CMOD*-deflection (LVDT2) relationship (N4S3)

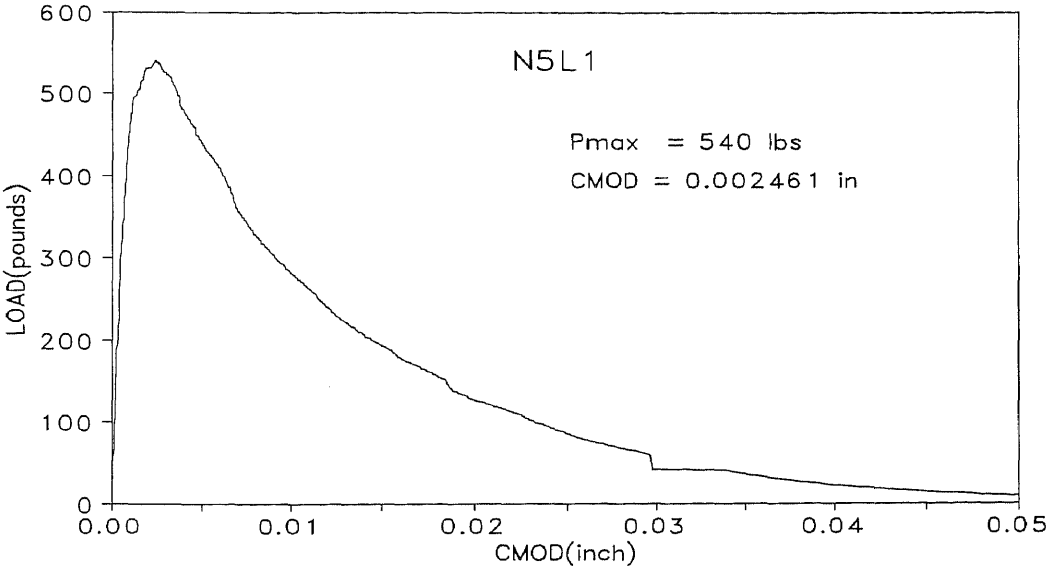

Figure A 26a Load-*CMOD* relationship (N5L1)

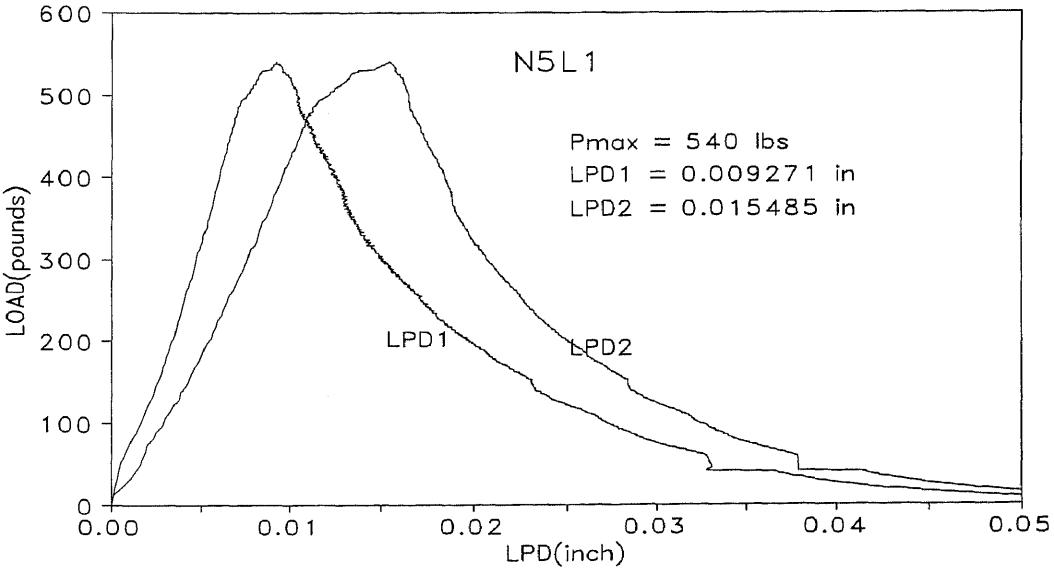

Figure A 26b Load-deflection relationship (N5L1)

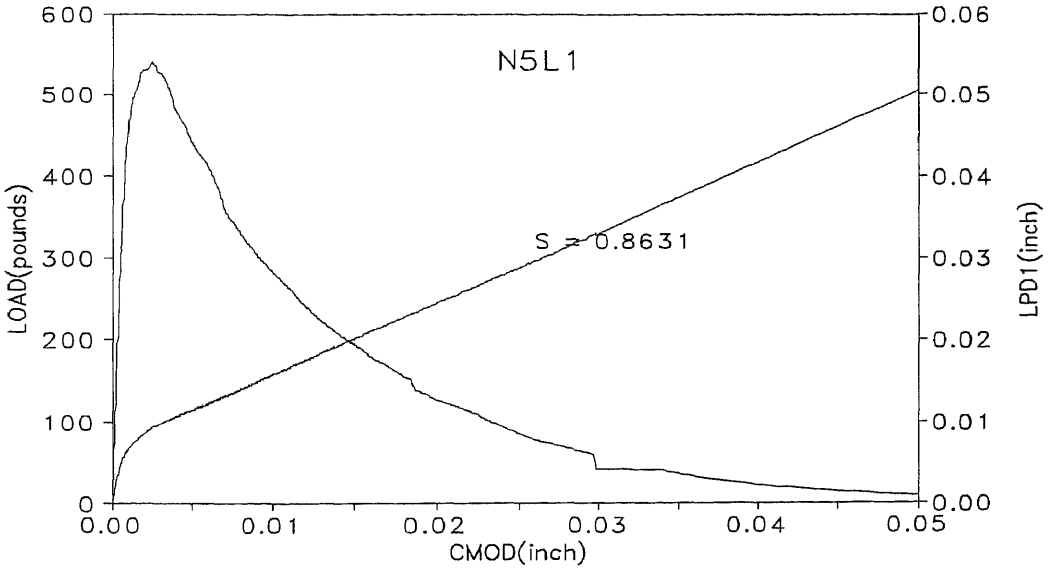

Figure A 26c Load-*CMOD*-deflection (LVDT1) relationship (N5L1)

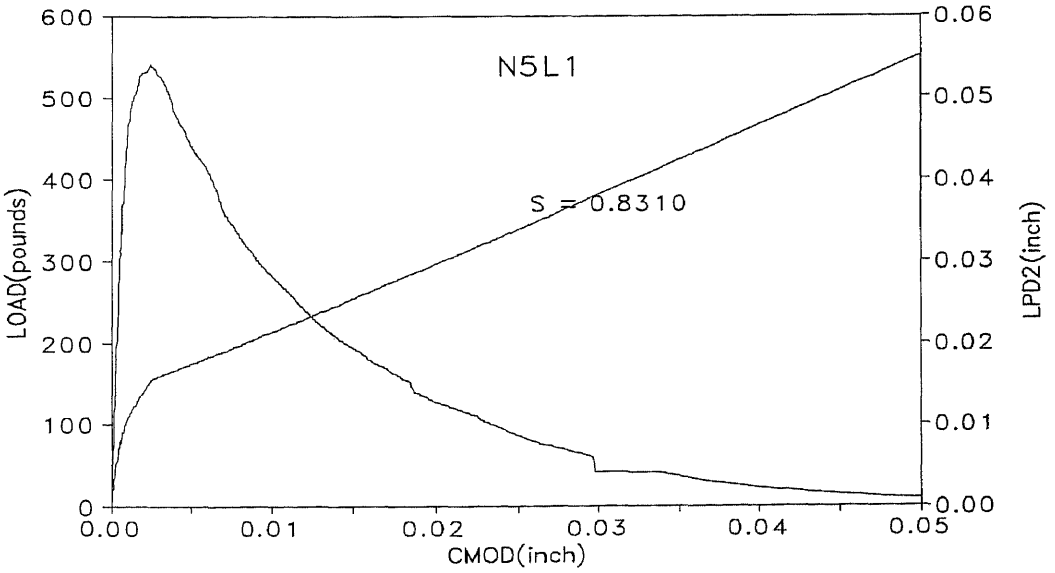

Figure A 26d Load-*CMOD*-deflection (LVDT2) relationship (N5L1)

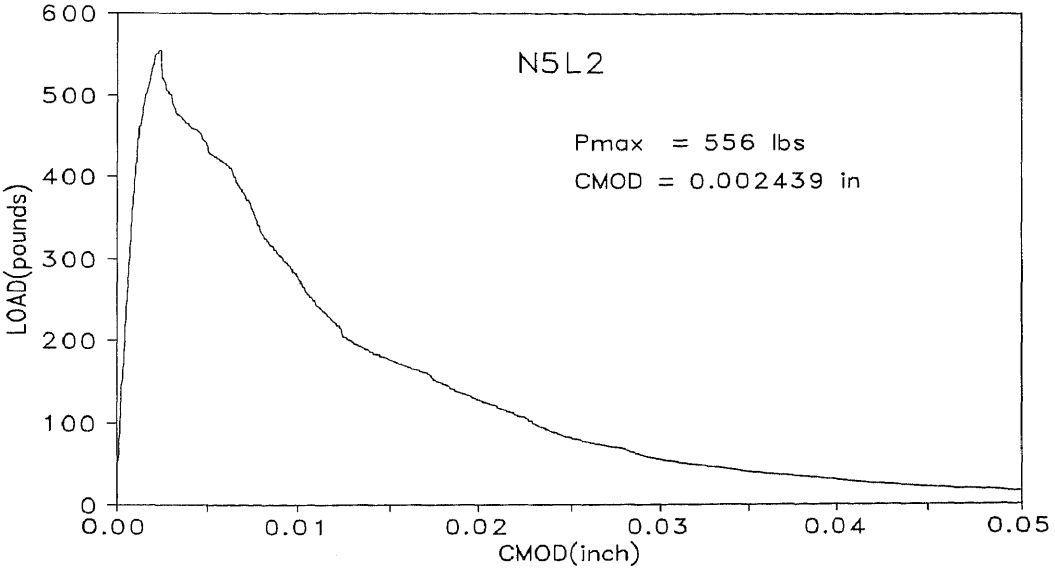

Figure A 27a Load-*CMOD* relationship (N5L2)

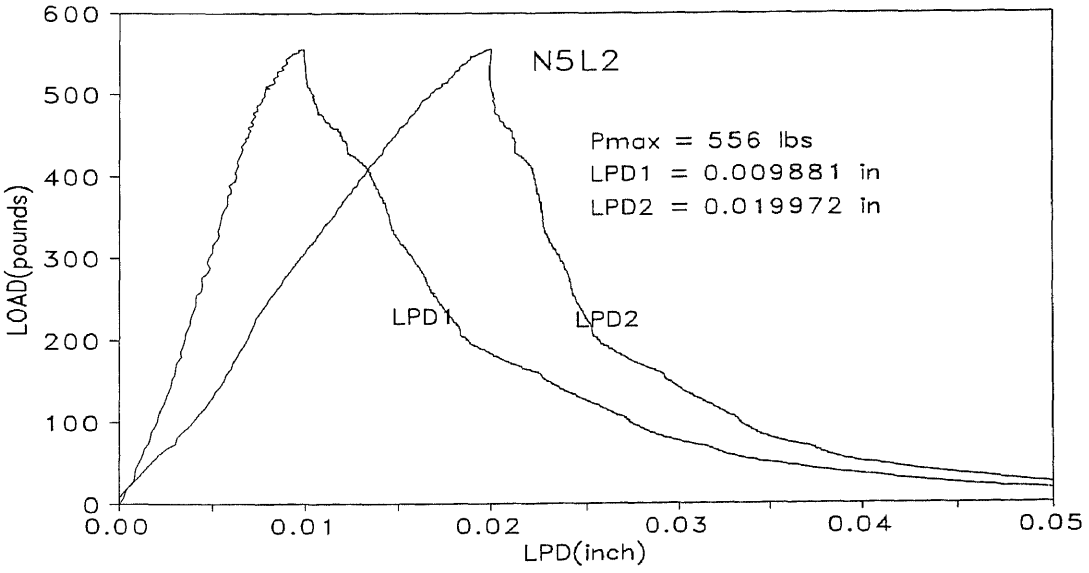

Figure A 27b Load-deflection relationship (N5L2)

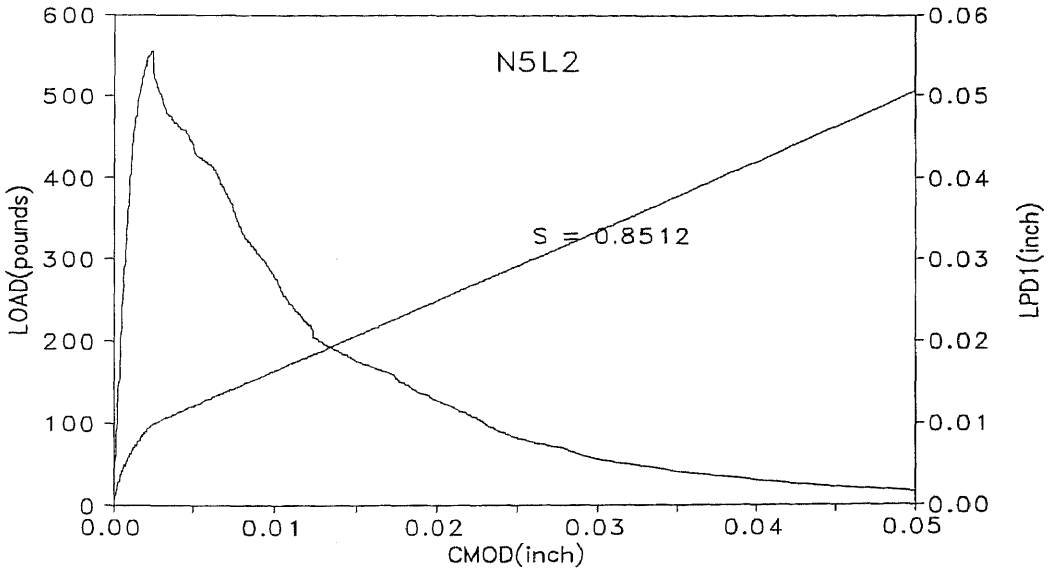

Figure A 27c Load-*CMOD*-deflection (LVDT1) relationship (N5L2)

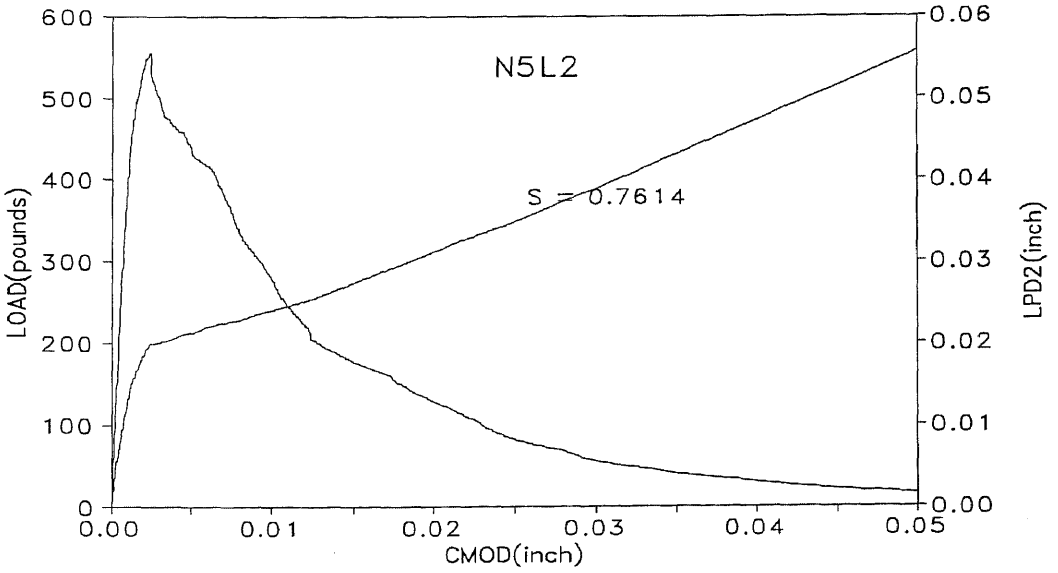

Figure A 27d Load-*CMOD*-deflection (LVDT2) relationship (N5L2)

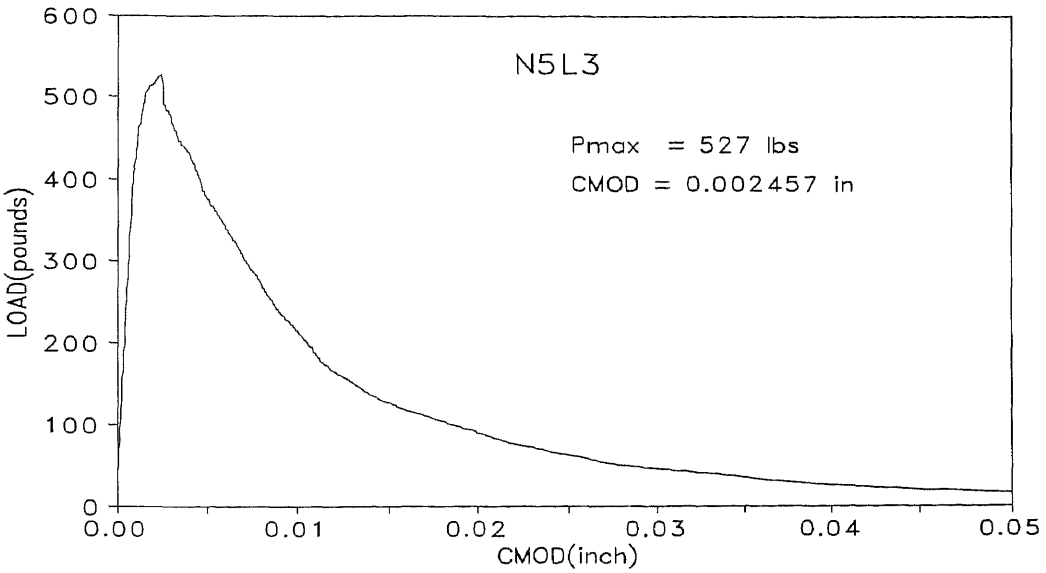

Figure A 28a Load-*CMOD* relationship (N5L3)

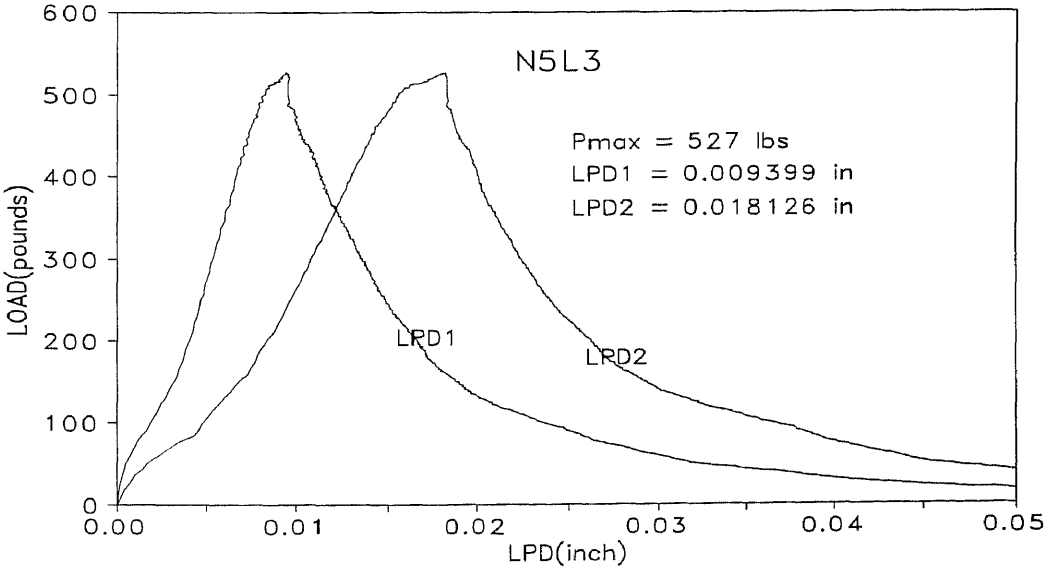

Figure A 28b Load-deflection relationship (N5L3)

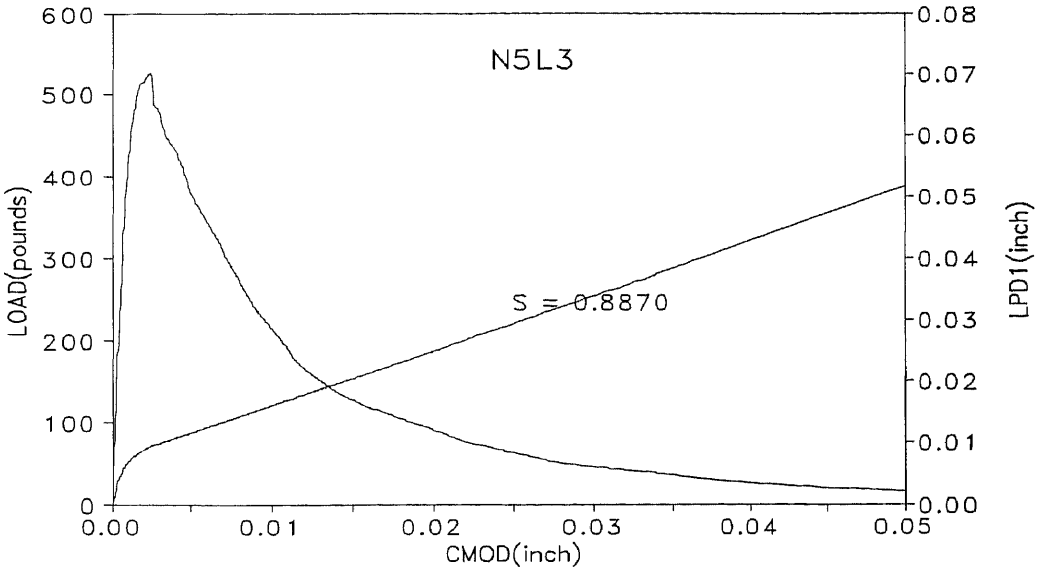

Figure A 28c Load-*CMOD*-deflection (LVDT1) relationship (N5L3)

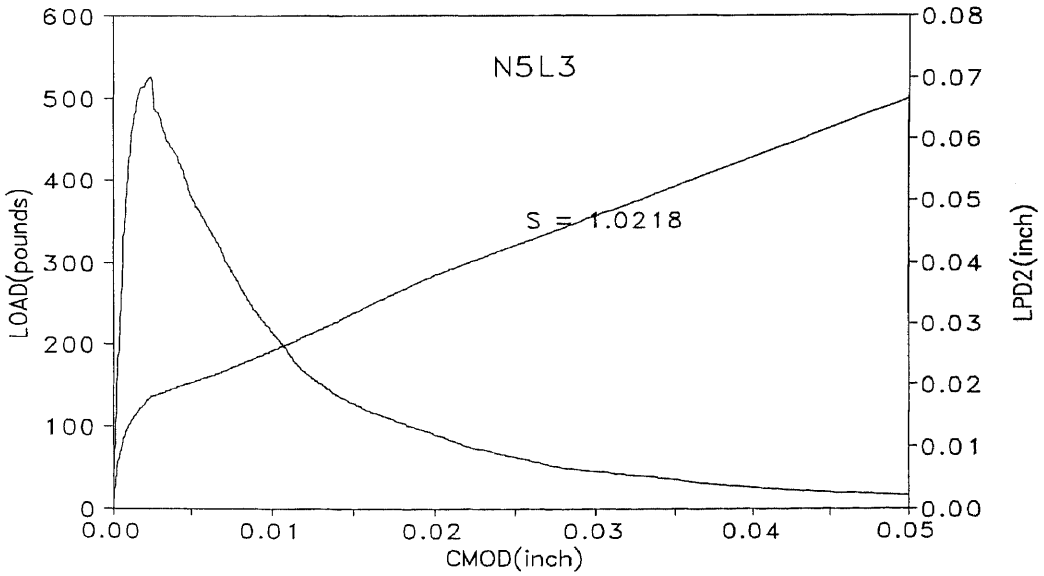

Figure A 28d Load-*CMOD*-deflection (LVDT2) relationship (N5L3)

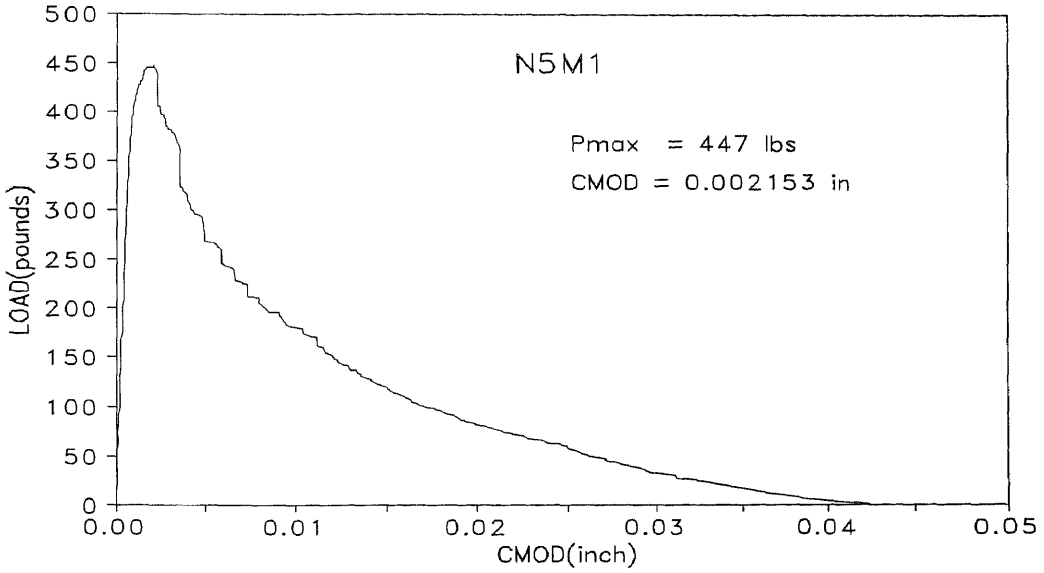

Figure A 29a Load-*CMOD* relationship (N5M1)

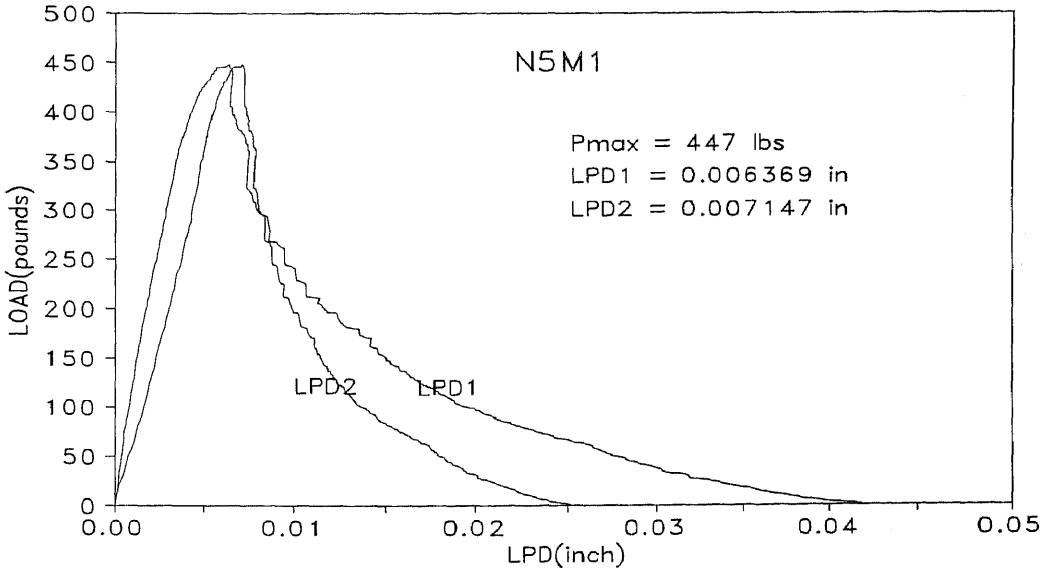

Figure A 29b Load-deflection relationship (N5M1)

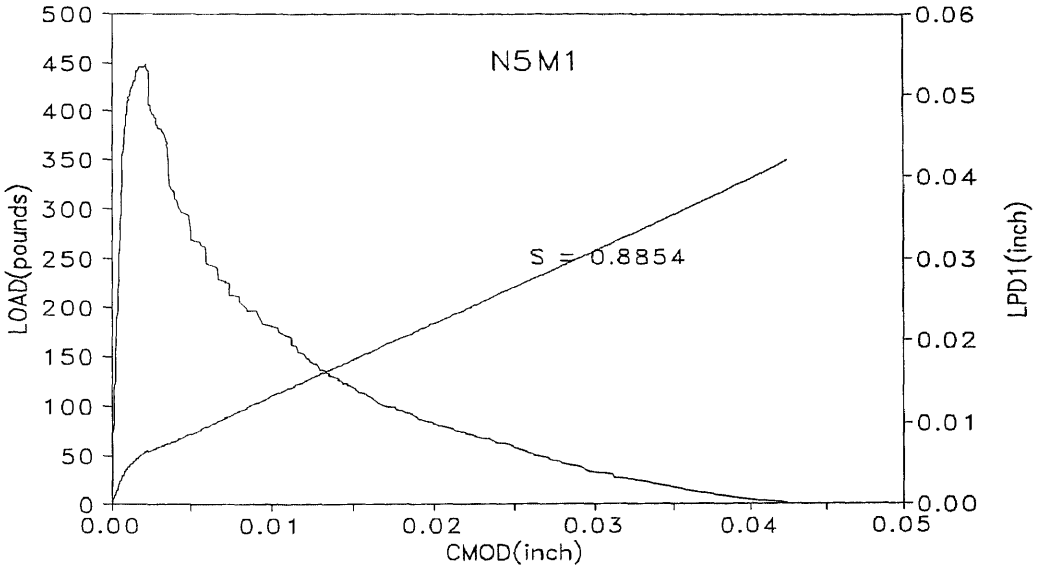

Figure A 29c Load-*CMOD*-deflection (LVDT1) relationship (N5M1)

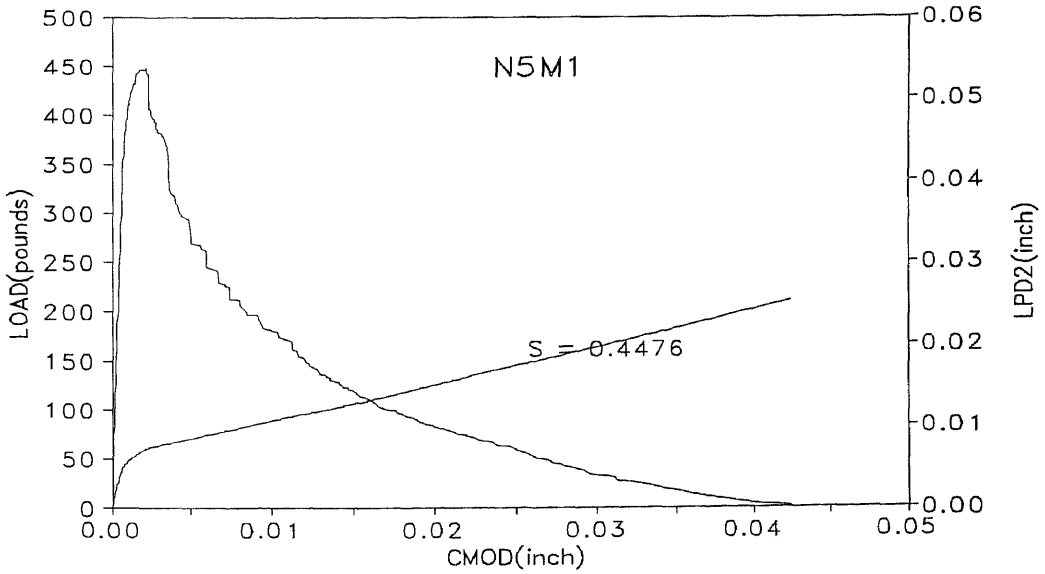

Figure A 29d Load-*CMOD*-deflection (LVDT2) relationship (N5M1)

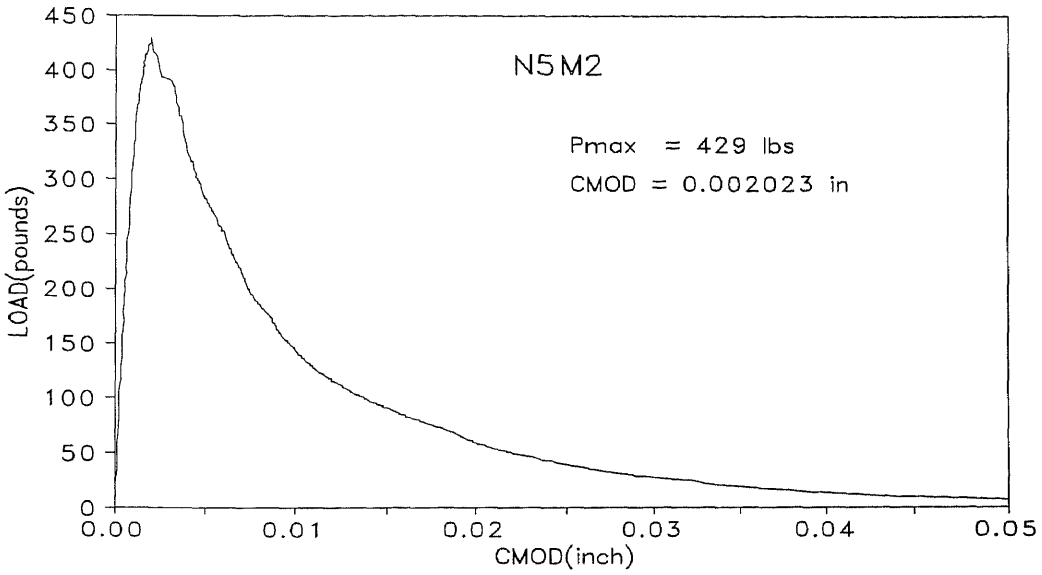

Figure A 30a Load-*CMOD* relationship (N5M2)

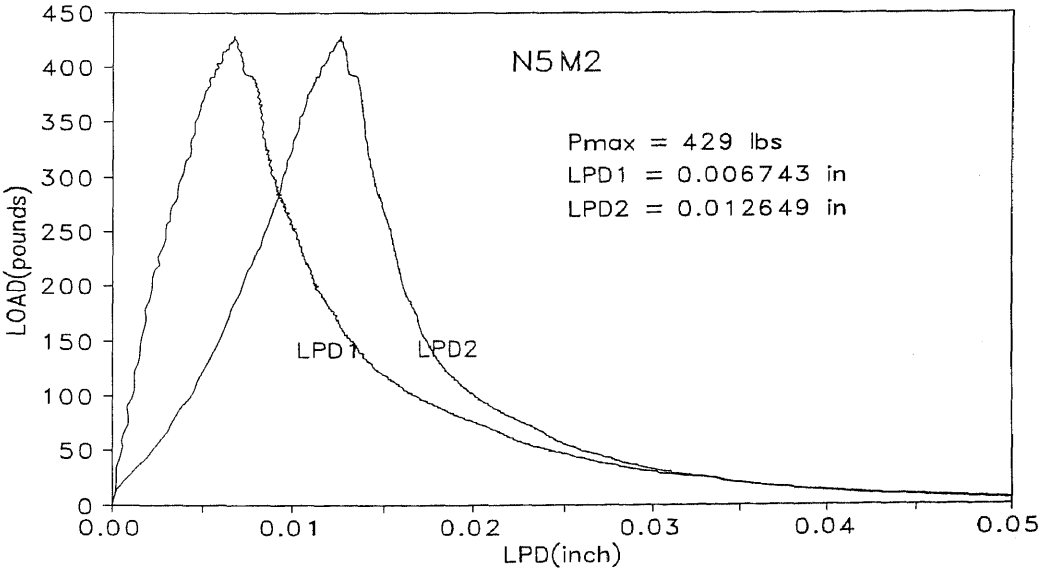

Figure A 30b Load-deflection relationship (N5M2)

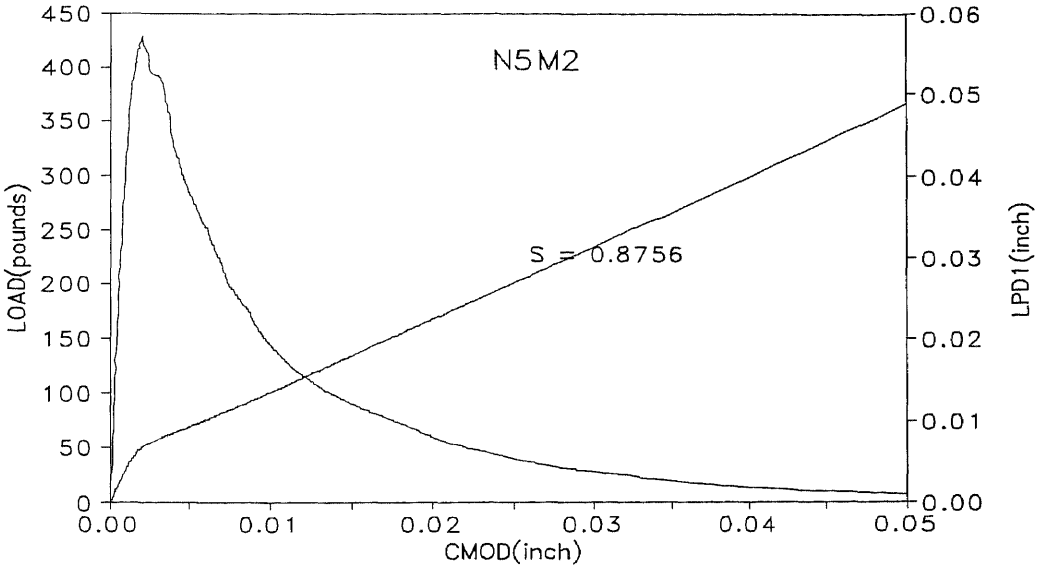

Figure A 30c Load-*CMOD*-deflection (LVDT1) relationship (N5M2)

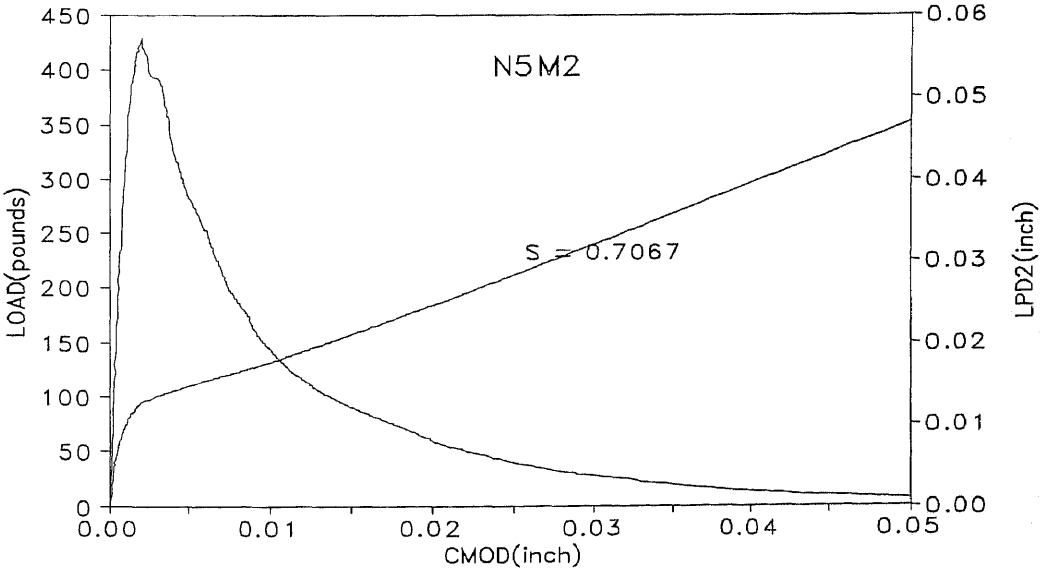

Figure A 30d Load-*CMOD*-deflection (LVDT2) relationship (N5M2)

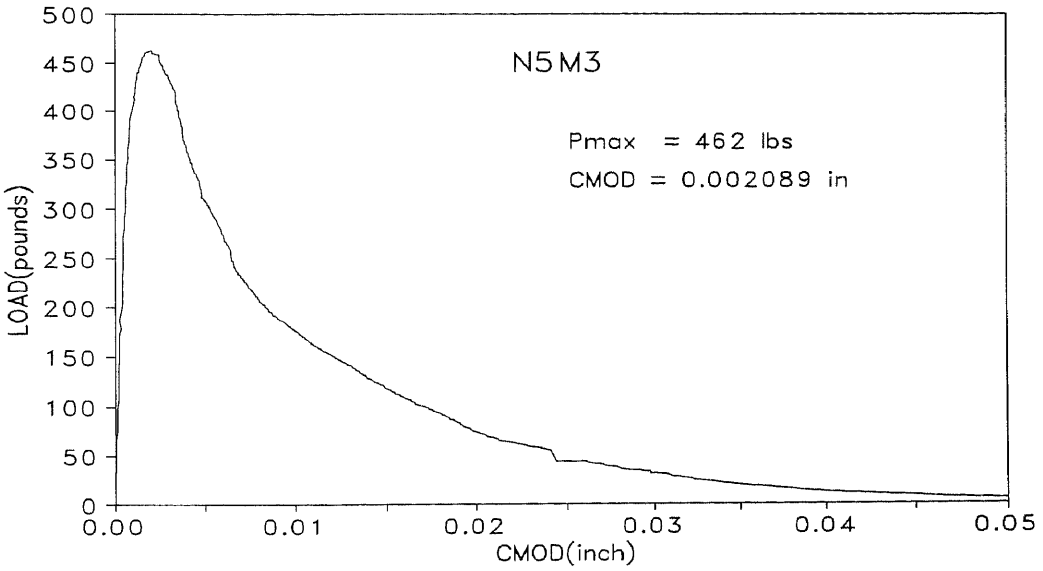

Figure A 31a Load-*CMOD* relationship (N5M3)

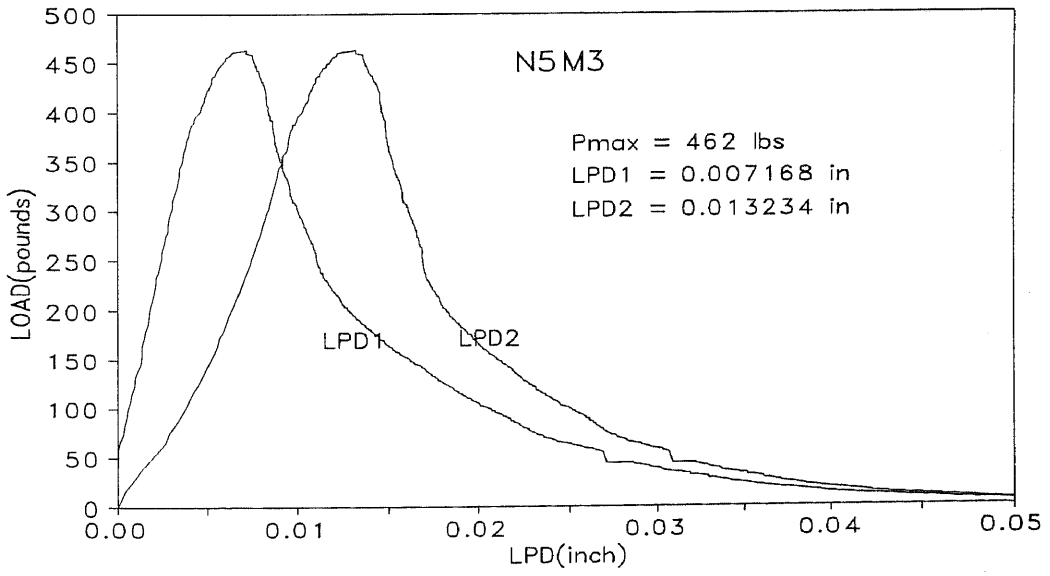

Figure A 31b Load-deflection relationship (N5M3)

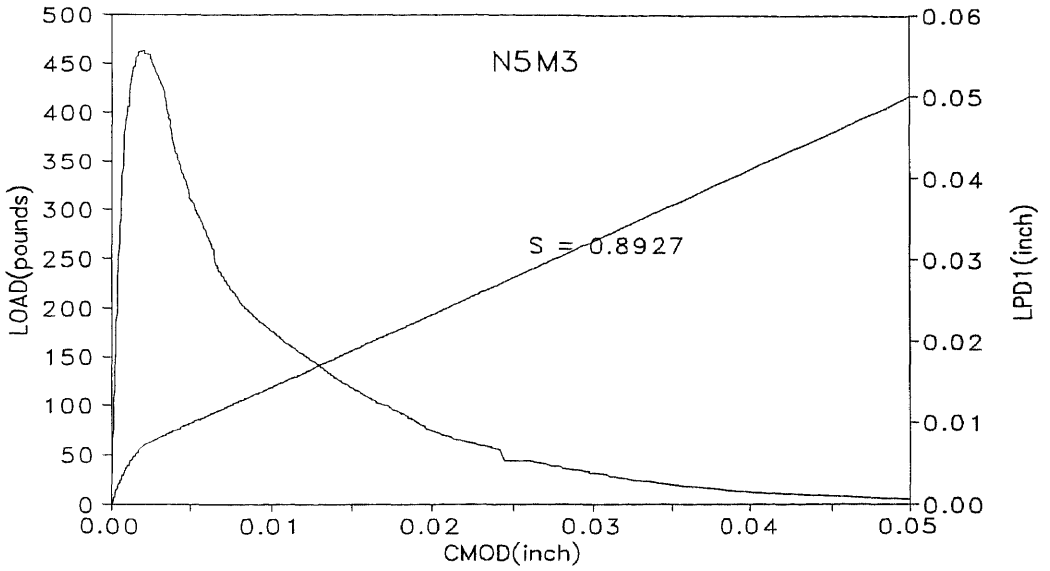

Figure A 31c Load-*CMOD*-deflection (LVDT1) relationship (N5M3)

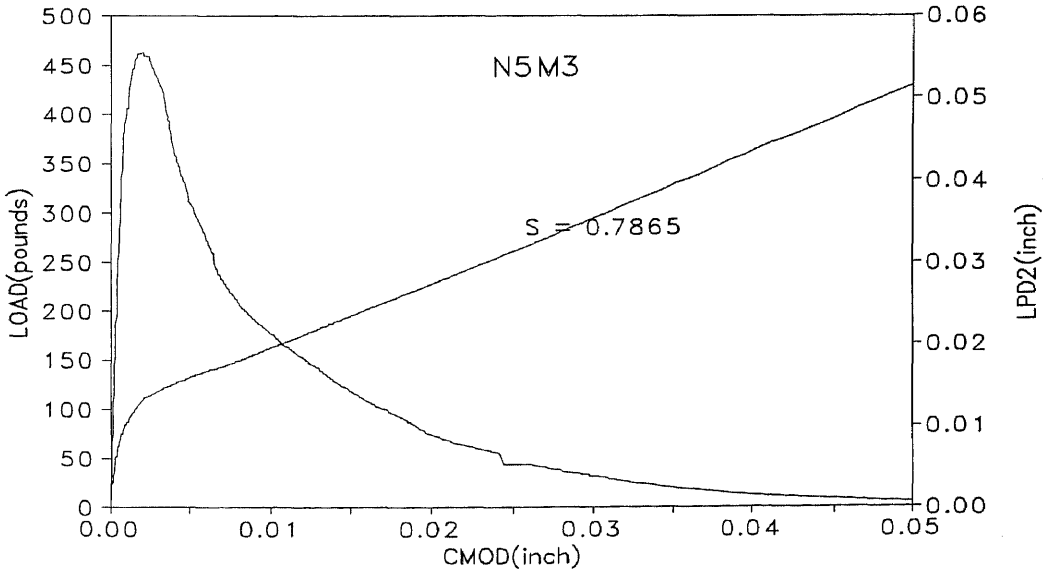

Figure A 31d Load-*CMOD*-deflection (LVDT2) relationship (N5M3)

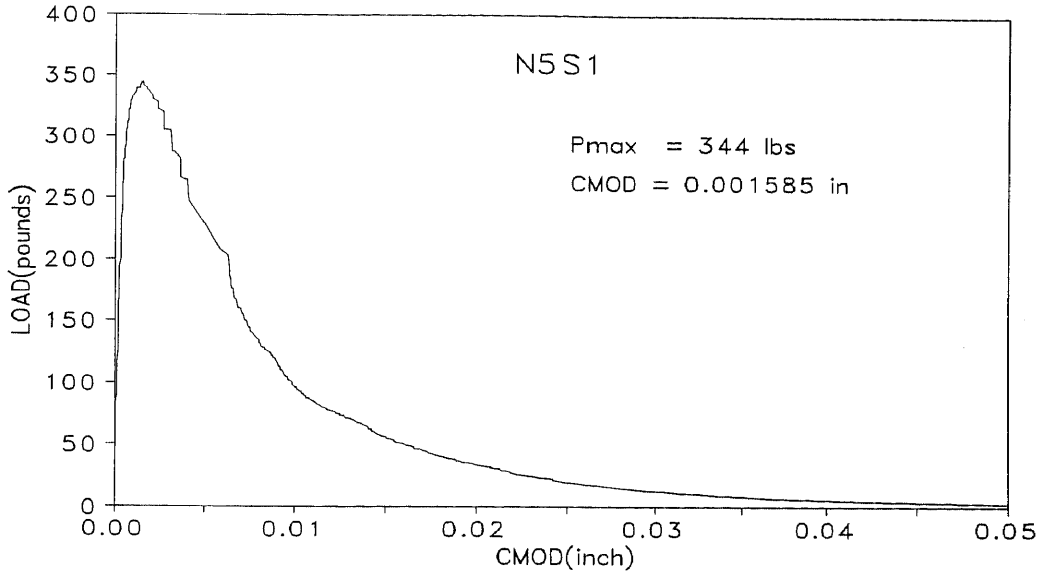

Figure A 32a Load-*CMOD* relationship (N5S1)

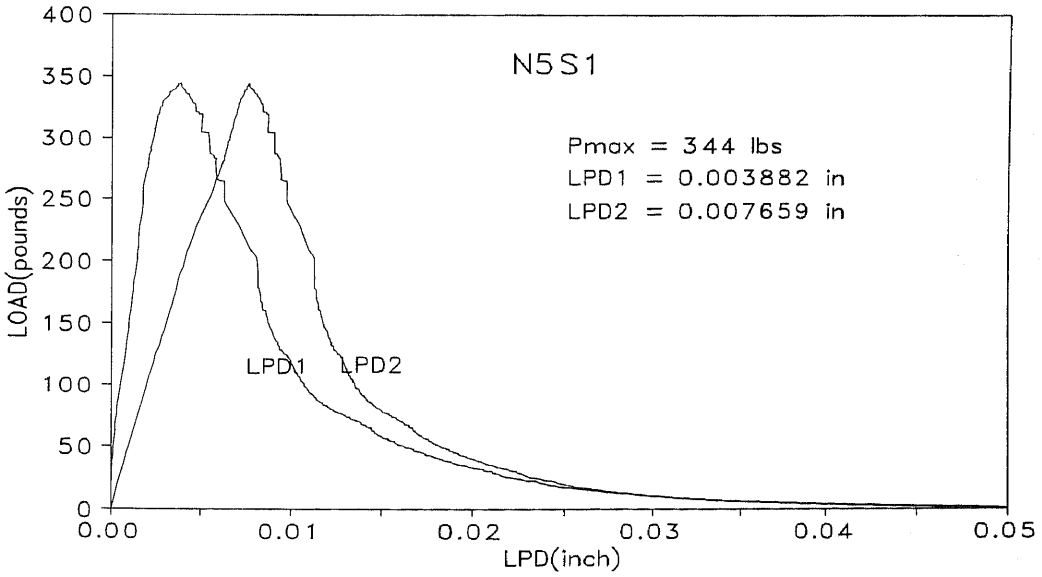

Figure A 32b Load-deflection relationship (N5S1)

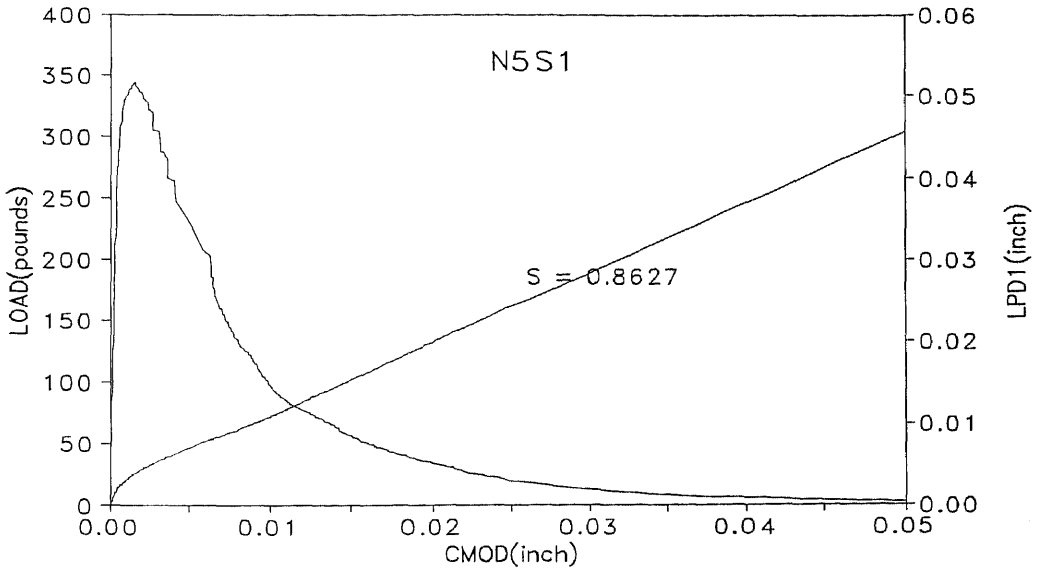

Figure A 32c Load-*CMOD*-deflection (LVDT1) relationship (N5S1)

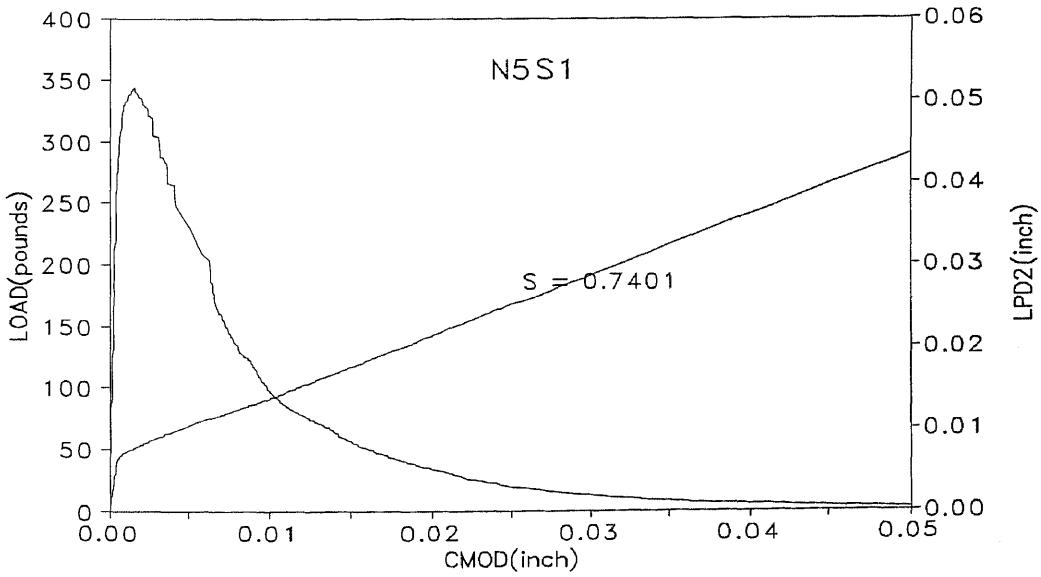

Figure A 32d Load-*CMOD*-deflection (LVDT2) relationship (N5S1)

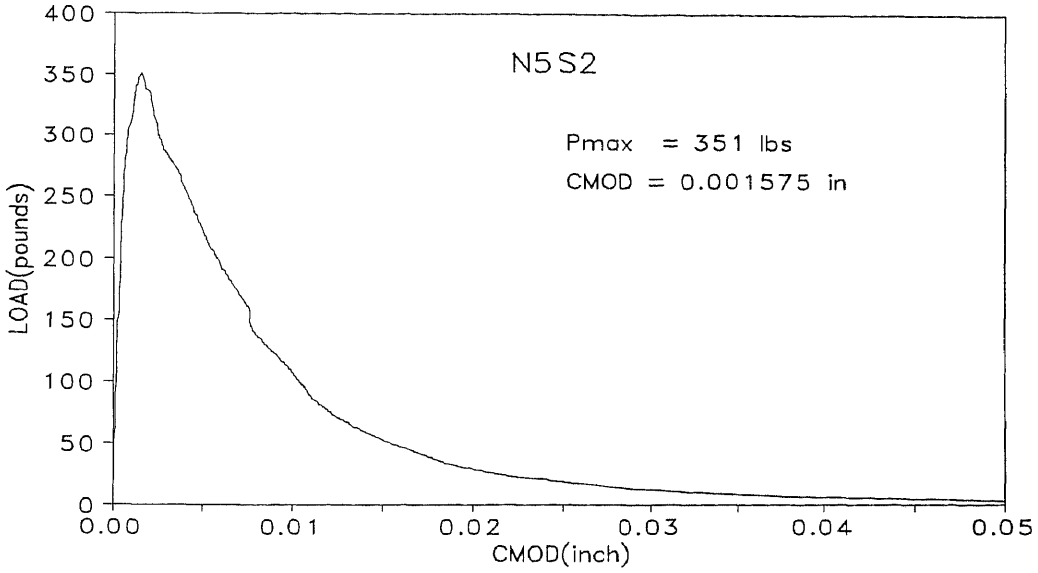

Figure A 33a Load-*CMOD* relationship (N5S2)

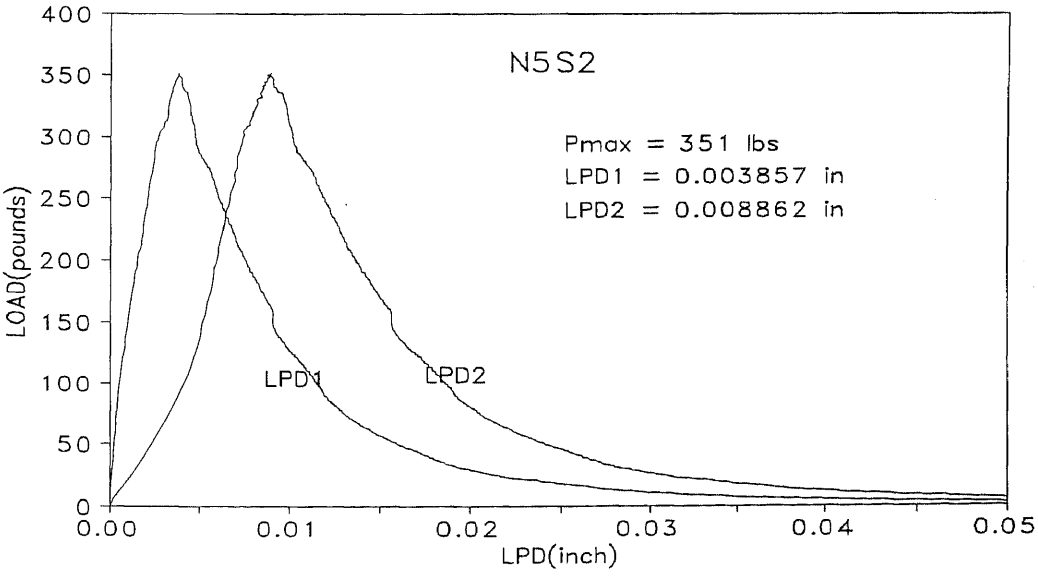

Figure A 33b Load-deflection relationship (N5S2)

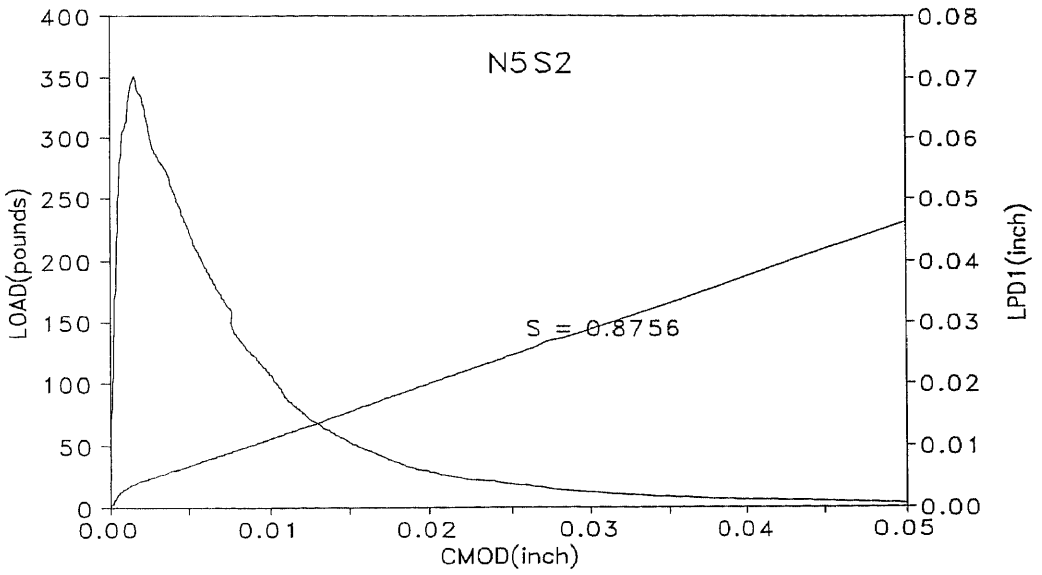

Figure A 33c Load-*CMOD*-deflection (LVDT1) relationship (N5S2)

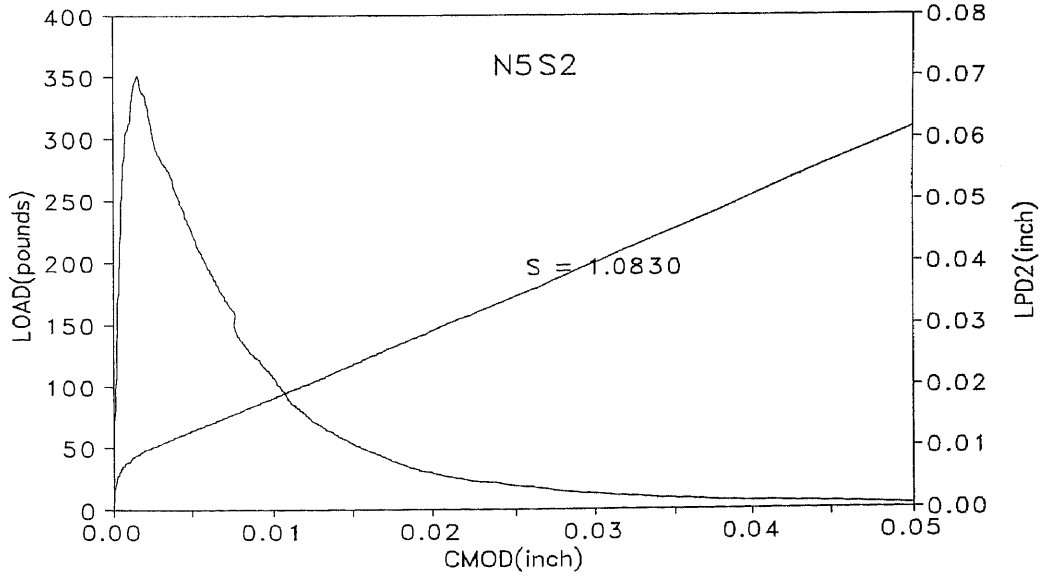

Figure A 33d Load-*CMOD*-deflection (LVDT2) relationship (N5S2)

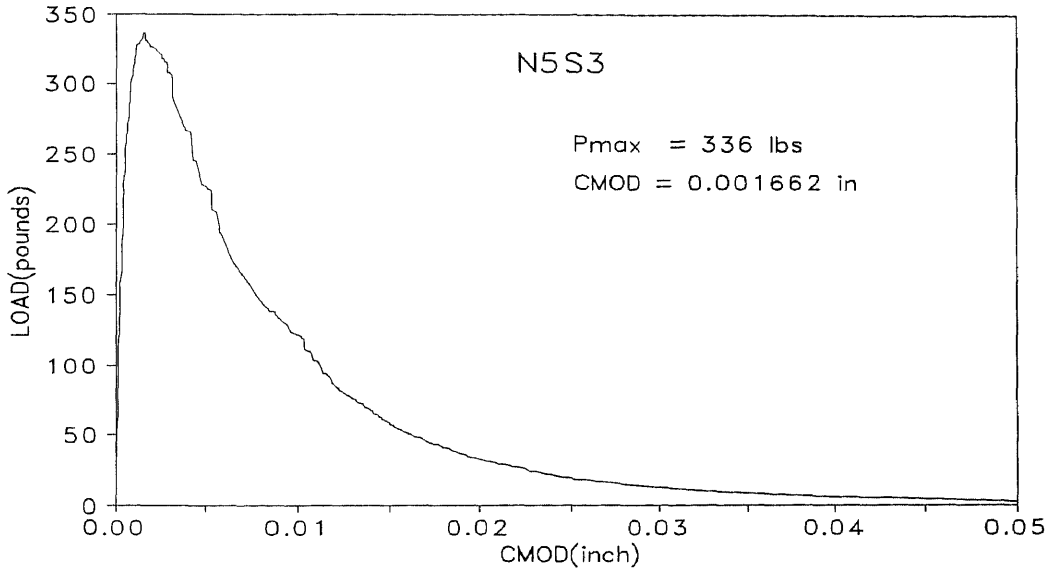

Figure A 34a Load-*CMOD* relationship (N5S3)

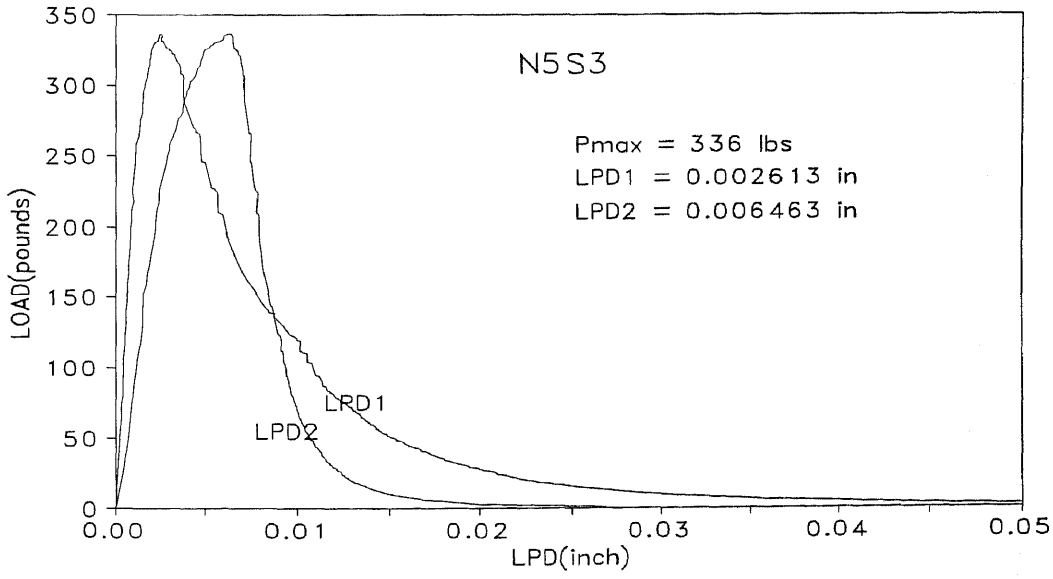

Figure A 34b Load-deflection relationship (N5S3)

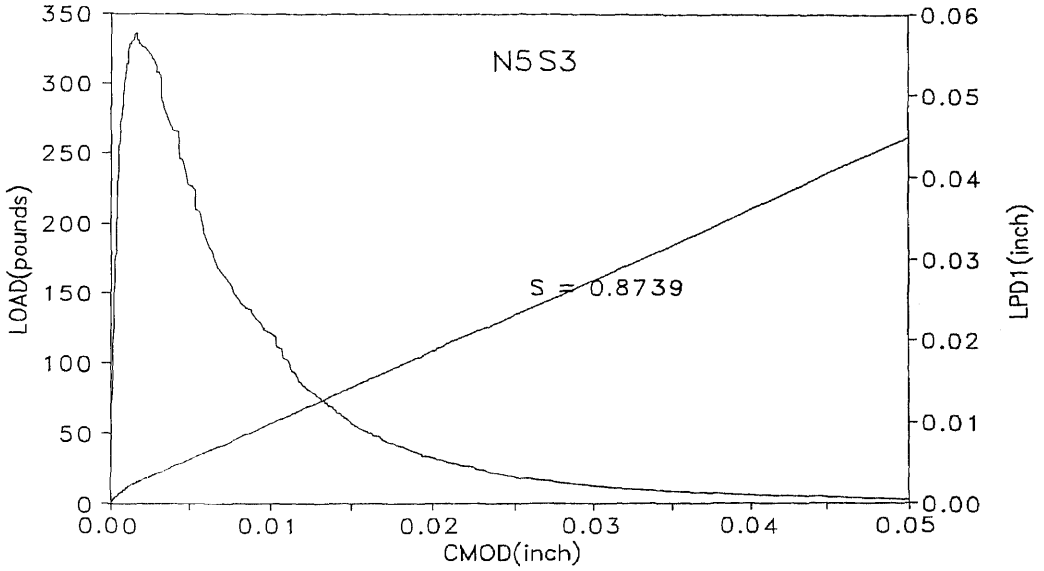

Figure A 34c Load-*CMOD*-deflection (LVDT1) relationship (N5S3)

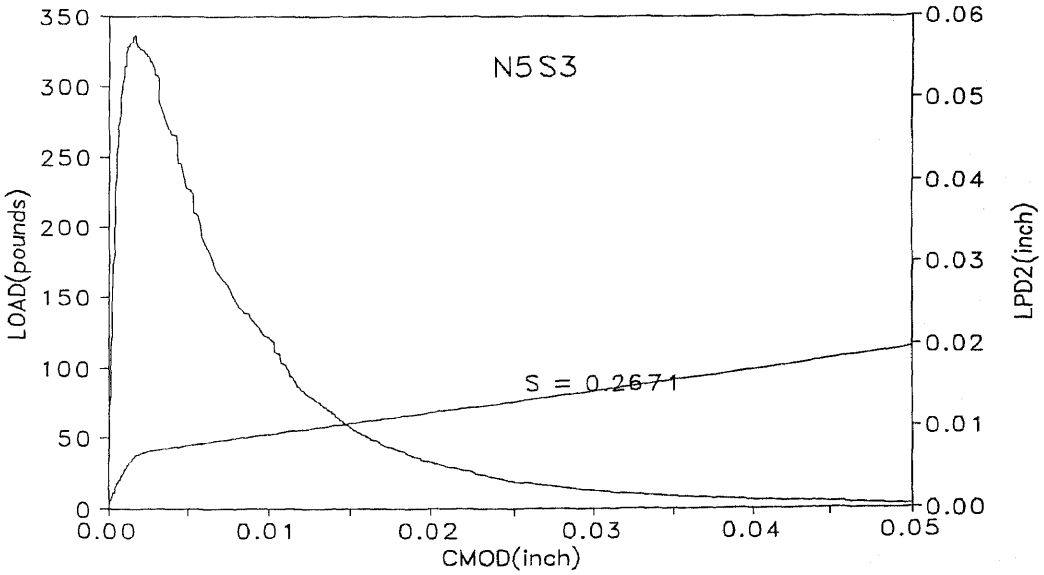

Figure A 34d Load-*CMOD*-deflection (LVDT2) relationship (N5S3)

REFERENCES

ASTM E399-83. 1983. "Standard Method of Test for Plane-Strain Fracture Toughness of Metallic Materials." *American Society for Testing and Materials*, N.Y, N.Y.

ASTM E616-82. 1982. "Standard Terminology Relating to Fracture Testing." *American Society for Testing and Materials*, N.Y, N.Y.

Bazent, Zdenek P. and Luigi Cedolin 1979. "Blunt Crack Band Propagation in Finite Element Analysis." *Journal of Engineering Mechanics Division, ASCE*, Vol. 105, NO. EM2: 297-315.

Bazent Zdenek P. and B. H. Oh 1983 "Crack Band Theory for Fracture of Concrete." *Materials and Structures*, Vol. 16, No. 93: 155-177.

Brown, J. H. 1983 "Measureing the Fracture Toughness of Cement Paste and Mortar." *Magzine of Concrete Research*, Vol.24, No.93: 185-196.

Darwin, D., S. L. McCabe, C. J. Brown and C. Schumm 1994. "Fracture Analysis of Steel-Concrete Bond." *Proceedings of the US-Europe Workshop on Fracture and Damage in Quasibrittle Structures*, Prague, Czech Republic: 549-556.

Elfgren, L. 1988. "Application of Fracture Mechanics to Concrete Structures." *Proceedings of International Workshop on the Fracture Toughness and Fracture Energy*, Sendai, Japan: 575-590.

Francois, D. 1984. "Fracture and Damage Mechanics of Concrete." *Proceedings of the NATO Advanced Research Workshop on Application of Fracture Mechanics to Cementitious Materials*, Northwestern University, Evanston, Illinois, USA: 141-156.

Griffith, A. A. 1920. "The Phenomena of Rupture and Flow in Solids." *Philosophical Transaction, Royal Society of London*, A 221: 163-198.

Griffith, A. A. 1924. "The Theory of Rupture." *Proceedings of 1st International Congress for Appl. Mech.*: 55-63.

Gopalaratnam, V. S., S. P. Shah, G. B. Batson, M. E. Criswell, V. Ramakrishnan, and M. Wecharatana 1991. "Fracture Toughness of Fiber Reinforced Concrete." *ACI Materials Journal*, Vol. 88, No. 4: 339-353.

REFERENCES
(Continued)

Hawkins, N. M. 1984. "The Role for Fracture Mechanics in Conventional Reinforced Concrete Design." *Proceedings of the NATO Advanced Research Workshop on Application of Fracture Mechanics to Cementitious Materials*, Northwestern University, Evanston, Illinois, USA: 639-666.

Hillerborg, A., M. Modeer, and P-E Petersson 1976. "Analysis of Crack Formation and Crack Growth in Concrete by means of Fracture Mechanics and Finite Elements." *Cement and Concrete Research*, Vol. 6: 773-782.

Hillerborg, A. 1985. "Results of Three Comparative Test Series for Determining the Fracture Energy G_F of Concrete." *Materials and Structures*, Vol. 18, No. 107: 407-413.

Inglis,. C. E. 1913. "Stress in a Plate due to the Presence of Crack and Sharp Corners." *Trans. Inst. Naval Architects*, 55, 219-241.

Jenq, Y. and S. P. Shah 1985. "Two Parameter Fracture Model for Concrete." *Journal of Engineering Mechanics, ASCE*, Vol. 111, No. 10: 1227-1241.

Jenq, Y. S. and S. P. Shah 1985. "A Fracture Toughness Criterion for Concrete." *Engineering Fracture Mechanics*, Vol. 21, No. 5: 1055-1069.

Irwin, G. R. 1957. "Analysis of Stresses and Strains Near the End of a Crack Transversing a Plate." *ASME Journal of Applied Mechanics*, Vol. 24: 361-364.

Kaplan, M. F. 1961. "Crack Propagation and the Fracture of Concrete." *ACI Journal*, Vol.58: 591-610.

Naus, D. J. and Lott, J. L. 1969. "Fracture Toughness of Portland Cement Concretes." *ACI Journal*, Vol. 66: 481-489.

Petersson, P. E. 1980. "Fracture Energy of Concrete: Method of Determination." *Cement and Concrete Research*, Vol. 10: 78-89.

Petersson, P. E. 1980. "Fracture Energy of Concrete: Practical Performance and Experimental Results." *Cement and Concrete Research*, Vol. 10: 91-101.

Petersson, P. E. 1981. "Crack Growth and Development of Fracture Zones in Plain Concrete and Similar Materials," Report TVBM-1008, Division of Building Materials, Lund Instiyute of Technology, Lunt, Sweden.

REFERENCES
(Continued)

RILEM Draft Recommendation 1985. "Determination of the Fracture Energy of Mortar and Concrete by means of Three-Point Bend Tests on Notched Beams." *Materials and Structures*, Vol.18, No 106: 285-296.

Tada, H., P. C. Paris and G. R. Irwin 1976. *The Stress Analysis of Cracks Handbook.* Del Research Corporation, Hellertown, Pennsylvania

Tassios, T. P. 1984. "Design Code and Fracture Mechanics." *Proceedings of the NATO Advanced Research Workshop on Application of Fracture Mechanics to Cementitious Materials*, Northwestern University, Evanston, Illinois, USA: 681-693.

Tindukasiri, S. 1993. *Fracture of Cementitious Composites.* Thesis for the Degree of Master of Science in Civil Engineering, New Jersey Institute of Technology.

Westergaard, H. M. 1939. "Bearing Pressures and Cracks." *ASME Journal of Applied Mechanics*, Vol. 61: A49-A53.